Title
Investigation of Coupled Processes in Argillite Rock: FY18 Progress

Author
Rutqvist, Jonny

Publication Date
2018-06-22

Peer reviewed

Investigation of Coupled Processes in Argillite Rock: FY18 Progress

Spent Fuel and Waste Disposition

Prepared for
U.S. Department of Energy
Spent Fuel and Waste Science and Technology

Jonny Rutqvist, Kunwhi Kim, Hao Xu, Yves Guglielmi, Jens Birkholzer
Lawrence Berkeley National Laboratory

June 22, 2018

LBNL-2001168

SFWD Working Document: External Release

Revision 5
01/15/2018

APPENDIX E

NTRD DOCUMENT COVER SHEET [1]

Name/Title of Deliverable/Milestone/Revision No.	Investigation of Coupled Processes in Argillite Rock: FY18 Progress M3SF-18LB010301031
Work Package Title and Number	Argillite Disposal R&D – LBNL/Argillite International Collaboration – LBNL
Work Package WBS Number	SF-18LB01030103 /SF-18LB01030107
Responsible Work Package Manager	Jonny Rutqvist (signature on file) (Name/Signature)

Date Submitted **6/22/2018**

Quality Rigor Level for Deliverable/Milestone[2]	☐ QRL-1 Nuclear Data	☐ QRL-2	☐ QRL-3	☒ QRL 4 Lab-specific [3]

This deliverable was prepared in accordance with Lawrence Berkeley National Laboratory (LBNL)
(Participant/National Laboratory Name)

QA program which meets the requirements of
☒ DOE Order 414.1 ☐ NQA-1 ☐ Other

This Deliverable was subjected to:

☐ Technical Review

Technical Review (TR)

Review Documentation Provided

☐ Signed TR Report or,
☐ Signed TR Concurrence Sheet or,
☒ Signature of TR Reviewer(s) below

Name and Signature of Reviewers

Mengsu Hu (signature on file)

☐ Peer Review

Peer Review (PR)

Review Documentation Provided

☐ Signed PR Report or,
☐ Signed PR Concurrence Sheet or,
☐ Signature of PR Reviewer(s) below

Name and Signature of Reviewers

NOTE 1: *Appendix E should be filled out and submitted with each deliverable. Or, if the PICS:NE system permits, completely enter all applicable information in the PICS:NE Deliverable Form. The requirement is to ensure that all applicable information is entered either in the PICS:NE system or by using the FCT Document Cover Sheet.*

- *In some cases there may be a milestone where an item is being fabricated, maintenance is being performed on a facility, or a document is being issued through a formal document control process where it specifically calls out a formal review of the document. In these cases, documentation (e.g., inspection report, maintenance request, work planning package documentation or the documented review of the issued document through the document control process) of the completion of the activity, along with the Document Cover Sheet, is sufficient to demonstrate achieving the milestone.*

NOTE 2: *If QRL 1, 2, or 3 is not assigned, then the QRL 4 box must be checked, and the work is understood to be performed using laboratory specific QA requirements. This includes any deliverable developed in conformance with the respective National Laboratory / Participant, DOE or NNSA-approved QA Program*

NOTE 3: *If the lab has an NQA-1 program and the work to be conducted requires an NQA-1 program, then the QRL-1 box must be checked in the work Package and on the Appendix E cover sheet and the work must be performed in accordance with the Lab's NQA-1 program. The QRL-4 box should not be checked*

This page intentionally left blank.

CONTENTS

This page is intentionally left blank.

LIST OF FIGURES

LIST OF TABLES

ACRONYMS

ALC	
ANDRA	French National Radioactive Waste Management Agency
BBM	Barcelona Basic Model
BExM	Barcelona Expansive Clay Model
BGR	Bundesanstalt für Geowissenschaften und Rohstoffe
BGS	British Geological Survey
CIEMAT	Centro De Investigaciones Energéticas, Medio Ambientales Y Tecnológicas
COx	callovo-oxfordian claystone
DECOVALEX	DEvelopment of COupled Models and their VAlidation against EXperiments
DFN	discrete fracture network
DOE	Department of Energy
DRZ	disturbed rock zone
EBS	engineered barrier system
EDZ	excavation damaged zone
FBG	fiber Bragg gratings
FE	full-scale emplacement
FEPs	Features, Events, and Processes
FLAC	Fast Lagrangian analysis of continua
FY	fiscal year
GDSA	Generic Disposal Systems Analysis
H2	Heater #2
HM	hydro-mechanical
IRSN	Institut de Radioprotection et de Sûreté Nucléaire
KAERI	Korea Atomic Energy Research Institute
KBS	Kärnbränslesäkerhet/Nuclear Fuel Safety
LBNL	Lawrence Berkeley National Laboratory
MHM	Meuse/Haute-Marne
NAGRA	National Cooperative for the Disposal of Radioactive Waste, Switzerland
PA	performance assessment
R&D	Research & Development
RBSN	Rigid-Body-Spring Network

REV	Representative Elementary Volume
SFWST	Spent Fuel and Waste Science and Technology
SIMFIP	Step-Rate Injection Method for Fracture In-situ Properties
STP	standard temperature and pressure
SURF	Sanford Underground Research Facility
TH	thermal-hydrological
THC	thermo-hydro-chemical
THM	thermo-hydro-mechanical
THMC	thermal-hydrological-mechanical-chemical
TOUGH	Transport of Unsaturated Groundwater and Heat
TPHM	two-part Hooke's model
TSX	Tunnel Sealing Experiment
UFD	Used Fuel Disposition
UFDC	Used Fuel Disposition Campaign
UFZ	Helmholtz-Centre for Environmental Research
UPC	Universitat Politècnica de Catalunya
URLs	Underground Research Laboratory

1. INTRODUCTION

Shale and argillite geological formations have been considered as potential host rock for geological disposal of high-level radioactive waste (HLW) throughout the world because of their low permeability, low diffusion coefficient, high retention capacity for radionuclides, and capability to self-seal fractures. The low permeability of clay and shale rock are well-known in the hydrogeology community where these rock types represent aquitards that severely limit groundwater movement, and in petroleum industry, where they act as caprocks limiting the rise of buoyant petroleum fluids. While fractures can occur in such formations, argillite and shale often demonstrate the tendency to self-seal fractures, which reduces the effects of fractures on bulk permeability. Other favorable characteristics of argillite/shale are the strong sorptive behavior for many radionuclides, reducing conditions because of the lack of oxygen transport from the surface, and chemical buffering the effects of materials introduced through repository construction, operation, and emplaced materials.

The focus of research within the Spent Fuel and Waste Science and Technology (SFWST), formerly called Used Fuel Disposal (UFD), Campaign is on repository-induced interactions that may affect the key safety characteristics of engineered barrier system (EBS) bentonite and host rock. These include thermal-hydrological-mechanical-chemical (THMC) processes that occur because of repository construction and waste emplacement. Some of the key questions addressed in this report include the formation of an excavation damaged zone (EDZ) near tunnels and the evolution of near field coupled thermo-hydro-mechanical (THM) processes after waste emplacement. In particular, this report describes our efforts to model these processes with confidence.

Within the SFWST program, LBNL's work on argillite disposal research & development (R&D) started in 2010 by leveraging on previous experience on coupled THM processes modeling within domestic and international nuclear waste programs (Rutqvist et al., 2001; 2002; 2011). Much of this work has been dedicated to develop and validate coupled THM simulators for the modeling of near-field coupled processes. Such near-field coupled processes are relatively short-lived from a safety assessment perspective, but could give rise to permanent changes, such as the formation of a thermally altered or damaged zone around excavations that could provide a path for transport of radionuclides if released from a waste package (Figure 1-1). For a repository hosted in clay-rock, the mechanical evolution and swelling of the protective buffer surrounding the waste package (often bentonite) are imperative to its functions, such as to provide long-term mechanical support to seal the EDZ. At the same time, the mechanical evolution of the buffer is governed by complex coupled interactions with temperature and hydraulics, between micro and macro clay structures, as well as with the host rock. Currently, more advanced constitutive mechanical models are being applied, but those require a large number of input parameters for describing processes at the different structural levels. It is therefore important to test and validate these models at a relevant field scale, in addition to verification and validation against independent analytical and numerical solutions and well-controlled laboratory experiments.

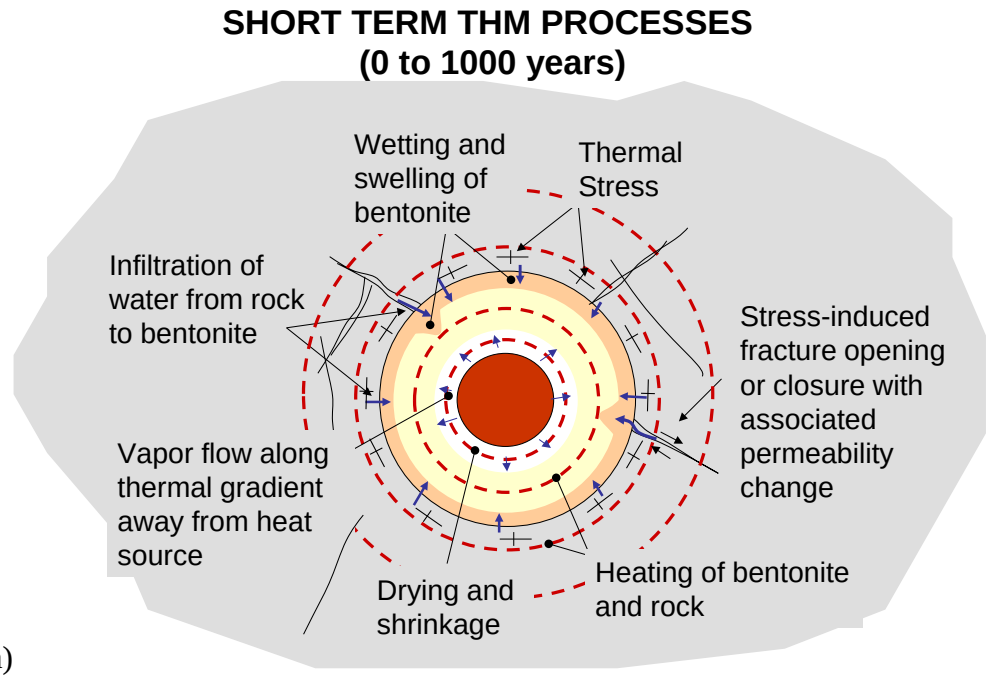

(a)

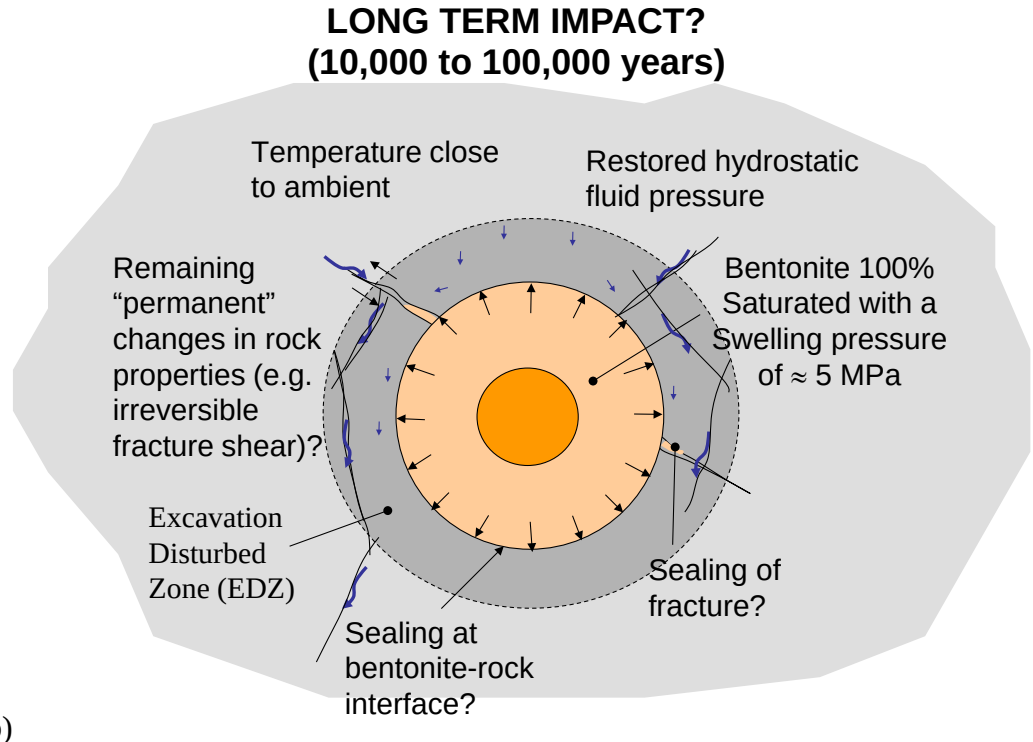

(b)

Figure 1-1. Schematic illustration of coupled THM processes driven by heat released from the waste package: (a) short-term THM processes, and (b) long-term impact of early time coupled THM processes.

LBNL is developing two complementary coupled simulation approaches to model THM processes (Figure 1-2). TOUGH-FLAC, based on linking LBNL's TOUGH2 multiphase fluid flow simulator with the FLAC3D geomechanics code, provides an efficient continuum modeling approach with state-of-the-art constitutive models for bentonite and host rock (Rutqvist et al., 2002; Rutqvist 2011; 2017). The complementary TOUGH-RBSN simulator, based on linking the TOUGH2 simulator with the Rigid-Body-Spring Network (RBSN) model, enables explicit modeling of discrete fractures and fracturing (Asahina et al. 2014; Kim et al., 2017). The TOUGH-RBSN is most suitable for detailed analysis of fracturing in laboratory samples as well as within the EDZ, whereas TOUGH-FLAC enables modeling of the evolution of the EBS, EDZ and surround host rock at a larger scale (Figure 1-2). TOUGH-FLAC with appropriated constitutive models is also used to calculate the evolution of the permeability and transport properties in the EDZ that can then be provided as input to future safety assessment models and Generic Disposal Systems Analysis (GDSA).

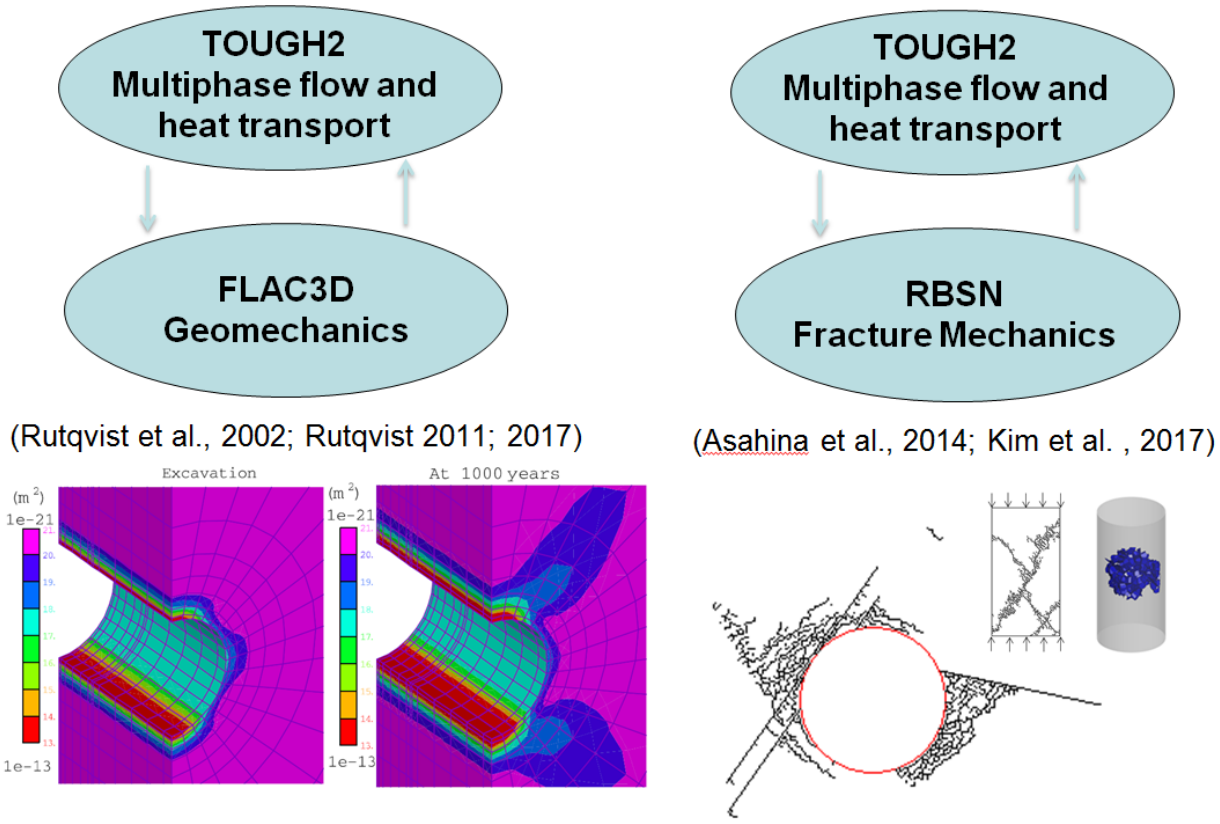

Figure 1-2. TOUGH-FLAC (left) and TOUGH-RBSN (right) models developed for coupled THM process analysis.

In this report, we present our FY2018 progress on these activities. The document delivers milestone M3SF-18LB010301031 "Investigation of Coupled Processes in Argillite Rock" in the LBNL Argillite R&D Work Package (SF-18LB01030103) with input from Activity SF-18LB010301071 "LBNL FY18 Argillite International Collaboration" in the LBNL Argillite International Collaboration Work Package (SF-18LB01030107). These activities address key Features, Events, and Processes (FEPs), which have been ranked in importance from medium to high, as listed in Table 7 of the Used Fuel Disposition

Campaign Disposal Research and Development Roadmap (FCR&D-USED-2011-000065 REV 1) (Nutt, 2012). Specifically, they address FEP 2.2.01, Excavation Disturbed Zone, for clay/shale, by investigating how coupled processes affect EDZ evolution; FEP 2.2.05, Flow and Transport Pathways; and FEP 2.2.08, Hydrologic Processes, and FEP 2.2.07, Mechanical Processes, as well as FEP 2.2.12, Gas Sources and Effects.

The activities documented in this report also address a number of research topics identified in Research & Development (R&D) Plan for Used Fuel Disposition Campaign (UFDC) Natural System Evaluation and Tool Development (Wang 2011), including Topics S3, Disposal System Modeling – Natural System; P1, Development of Discrete Fracture Network (DFN) Model; P14, Technical Basis for Thermal Loading Limits; and P15, Modeling of Disturbed Rock Zone (DRZ) Evolution (Clay Repository).

In the following Sections 2 and 3 we present the current status of the TOUGH-FLAC and TOUGH-RBSN simulators for modeling coupled THM processes in argillite, including fracturing. This is followed in Sections 4 and 5 by validation of the TOUGH-FLAC model against major *in situ* heater experiments at the Mont Terri Underground Research Laboratory (URL) in Switzerland and at the URL in Bure, France. The heater experiments modeled are the Mont Terri FE (Full-scale Emplacement) Experiment, conducted as part of the Mont Terri Project, and the TED and ALC experiments conducted in Callovo-Oxfordian claystone (COx) at the Meuse/Haute-Marne (MHM) URL in Bure, France. The modeling of the TED and ALC heater experiments is part of a modeling task (Task E) of the international DECOVALEX-2019 project. DECOVALEX, which stands for DEvelopment of COupled Models and their VALidation against EXperiments, is an international collaborative activity, in which DOE and LBNL gain access to unique laboratory and field data defined as modeling test cases. DECOVALEX tasks are studied collectively among several international groups to better understand the processes and to improve numerical models that could eventually be applied in the performance assessment for nuclear waste disposal in clay host rocks and bentonite backfill. Section 6 presents LBNL's activities for modeling gas migration in bentonite related to another task (Task A) of the international DECOVALEX project. In Section 7, we present new FY2018 work related to monitoring and characterization of faults using a unique borehole tool. Finally, in Section 8, we conclude with a summary of achievements in FY2018, planned work for the rest of FY2018, and proposed work for FY2019.

2. STATUS OF TOUGH-FLAC SIMULATOR

The TOUGH-FLAC simulator (Rutqvist et al., 2002; Rutqvist, 2011), used within the SFWST Argillite R&D work package, has been adapted for modeling coupled THM processes associated with bentonite backfilled repositories in argillite host rocks. For rigorous modeling of the THM behavior of bentonite-based (swelling) buffer and back-fill materials, the BBM (Barcelona Basic Model) and BExM (Barcelona Expansive Model) have been implemented into TOUGH-FLAC (Rutqvist et al., 2011; 2014b; Vilarrasa et al., 2016). Constitutive models to describe anisotropic THM behavior of shale rocks have also been adapted. This model development has been accompanied by extensive testing, verification and validation, including participation within international collaborative projects such as DECOVALEX. In the following subsections we present more details on the status of the TOUGH-FLAC, including the status of the numerical framework for coupled THM modeling and geomechanical constitutive models, followed by a list of completed verification and validation examples, as well as new verifications against analytical solutions.

2.1 TOUGH-FLAC Framework

As mentioned in the introduction, the TOUGH-FLAC simulator (Rutqvist 2011; 2017), is based on linking the TOUGH2 multiphase flow and heat transport simulator (Pruess et al., 2012) with the FLAC3D geomechanical simulator (Itasca 2011). In this approach, TOUGH2 (Pruess et al., 2012) is used for solving multiphase flow and heat transport equations, whereas FLAC3D (Itasca, 2011) is used for solving geomechanical stress-strain equations.

For analysis of coupled THM problems, TOUGH2 and FLAC3D are executed on compatible numerical grids and linked through a coupled THM model (Figure 2-1) with coupling functions to pass relevant information between the field equations, which are solved in the respective codes. In the coupling scheme between TOUGH2 and FLAC3D, the TOUGH2 multiphase pressures, saturation, and temperature are provided to update temperature, and pore pressure to FLAC3D (Figure 2-1). After data transfer, FLAC3D internally calculates thermal expansion, swelling, and effective stress. Conversely, element stress or deformation from FLAC3D is supplied to TOUGH2 to correct element porosity, permeability, and capillary pressure for the fluid-flow simulation in TOUGH2. The corrections of hydraulic properties are based on material-specific functions.

In a TOUGH-FLAC simulation, the calculation is stepped forward in time with the transient multiphase fluid flow analysis in TOUGH2, and at each time step or at the TOUGH2 Newton iteration level, a quasi-static mechanical analysis is conducted with FLAC3D to calculate stress-induced changes in porosity and intrinsic permeability (Figure 2-2). In this scheme, the fluid-flow sequence is solved first under fixed stress with a porosity correction $\Delta\Phi_c$ derived from the constitutive equations of solid:

$$\mathrm{d}\Phi = \left(\frac{b^2}{K} + \frac{b-\phi}{K_s}\right)\mathrm{d}p + \phi\alpha_s \mathrm{d}T - \Delta\Phi_c \tag{2.1}$$

$$\Delta\Phi_c = -\frac{b}{K}\mathrm{d}\sigma_v = -\frac{b}{K}(K\mathrm{d}\epsilon_v - b\mathrm{d}p - K\alpha\mathrm{d}T) \tag{2.2}$$

where K is the bulk modulus of porous medium, K_s is the bulk modulus of solid skeleton, b is the Biot's coefficient, p is the pore pressure, ϕ is the porosity, α_s is the volumetric thermal expansion coefficient of solid grains, T is the absolute temperature, σ_v is the mean stress, and ϵ_v is the volumetric strain. The resulting pressure and temperature are prescribed in the mechanical sequence. This corresponds to so-called stress-fixed iterations in the sequential scheme, in which the solution becomes unconditionally stable. The resulting THM analysis may be explicit sequential, meaning that the porosity and permeability is evaluated only at the beginning of each time step, or the analysis may be implicit sequential, with

permeability and porosity updated on the Newton iteration level toward the end of the time step using an iterative process.

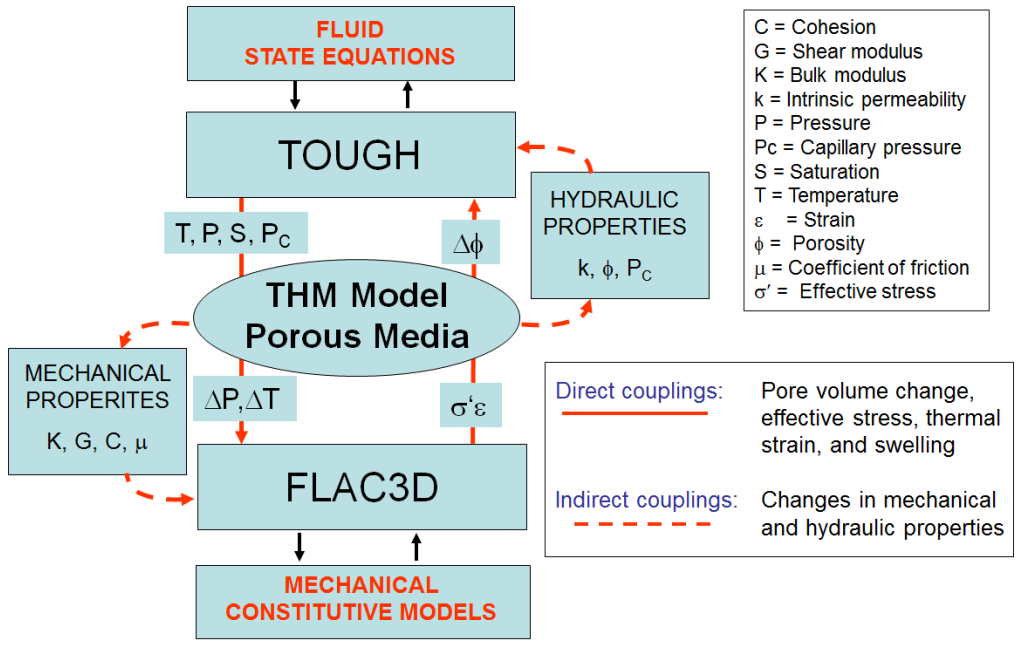

Figure 2-1. Schematic of linking of TOUGH2 and FLAC3D in a coupled TOUGH-FLAC simulation.

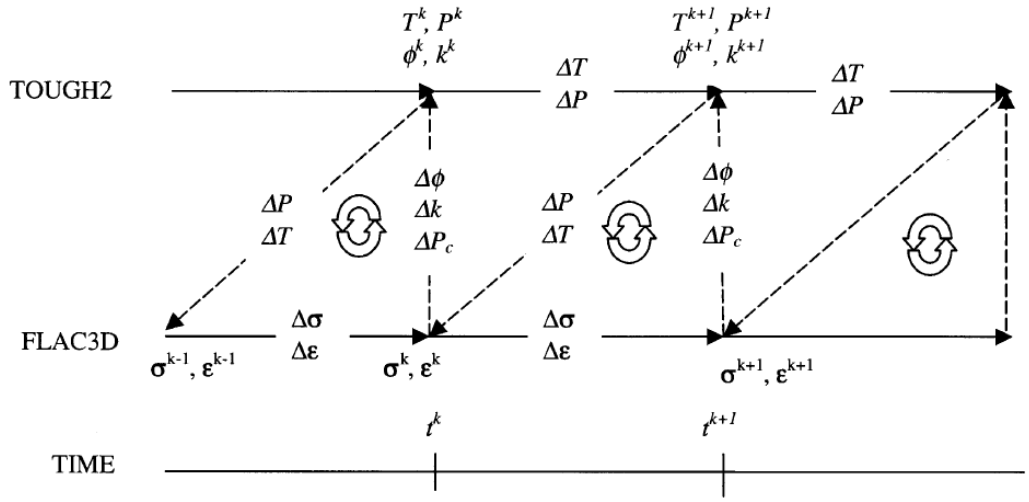

Figure 2-2. Numerical procedure of a linked TOUGH2 and FLAC3D simulation with subscript k signifying time step.

2.2 Bentonite Constitutive THM Models in TOUGH-FLAC

Since 2010, the TOUGH-FLAC simulator has been adapted and applied to issues related to nuclear waste disposal with bentonite backfilled tunnels (Rutqvist et al., 2011; 2014b). This includes implementation of the BBM (Alonso et al., 1990) for the mechanical behavior of unsaturated soils, which has been applied for modeling of bentonite backfill behavior (Rutqvist et al., 2011). The model can describe many typical features of unsaturated soil mechanical behavior, including wetting-induced swelling or collapse strains, depending on the magnitude of applied stress, as well as the increase in shear strength and apparent preconsolidation stress with suction (Gens et al., 2006). Figure 2-3 presents the yield surface of the BBM model in *q-p-s* space. The shaded surface corresponds to the elastic region at fully water-saturated conditions. The figure also shows how the yield surface expands at unsaturated and dryer conditions when suction increases. There is an increase in both the apparent pre-consolidation pressure along the load collapse (LC) yield surface and by the increasing tensile strength, which in turn leads to an increased cohesion and shear strength.

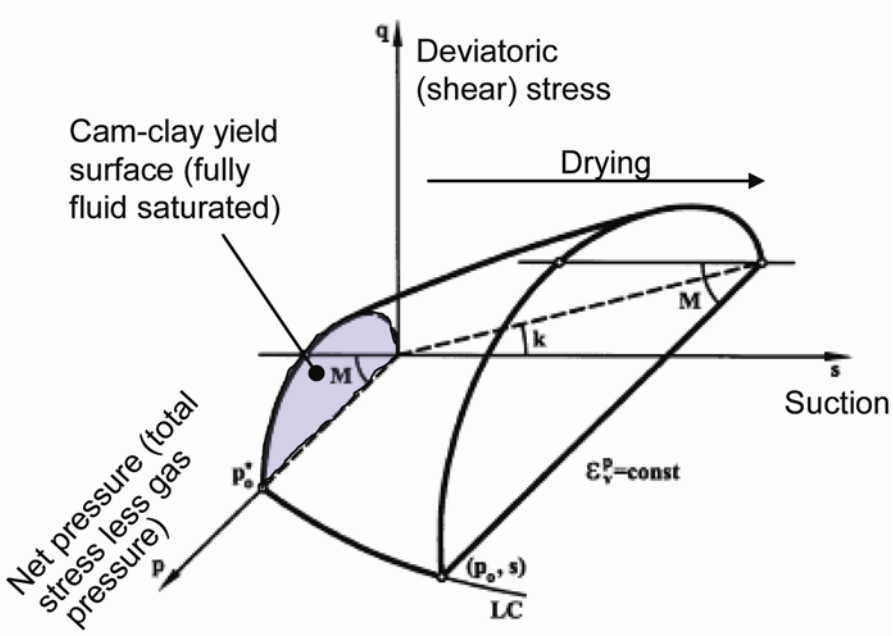

Figure 2-3. BBM constitutive model showing the yield surface in q-p-s space.

The BBM has been used for modeling bentonite-buffer behavior in various national nuclear waste programs in Europe and Japan. For example, the BBM was successfully applied to model the coupled THM behavior of unsaturated bentonite clay associated with the full-scale engineered barrier experiment (FEBEX) *in situ* heater test at the Grimsel Test Site, Switzerland (Gens et al., 2009). The BBM has also been applied to other types of bentonite-sand mixtures based on MX-80, considered as an option for an isolating buffer in the Swedish KBS-3 repository concept (Kristensson and Åkesson 2008). As part of the Used Fuel Disposition (UFD) program, the BBM was also used by Rutqvist et al. (2014b) for modeling of coupled THM processes around a generic repository in a clay host formation. In the last few years, as part of the UFD and current SFWST program, the BBM has been extended to a dual-structure model, corresponding to the Barcelona Expansive Model (BExM). In a dual-structure model, the material consists of two structural levels: a microstructure in which the interactions occur at the particle level, and

a macrostructure that accounts for the overall fabric arrangement of the material comprising aggregates and macropores (Figure 2-3) (Gens et al., 2006, Sánchez et al., 2005, Gens and Alonso 1992). A dual-structure model has important features for modeling the mechanical behavior of a bentonite buffer, such as irreversible strain during suction cycles. Moreover, a dual-structure model provides the necessary link between chemistry and mechanics, enabling us to develop a coupled THMC model for the analysis of long-term EBS behavior. This approach enables mechanistic modeling of processes important for long-term buffer stability, including effects of pore-water salinity on swelling (loss of swelling), conversion of smectite to nonexpansive mineral forms (loss of swelling), and swelling pressure versus exchangeable cations. Details of the development, testing and applications of the dual-structure model, were first presented in the FY2014 UFD milestone report titled "Investigation of Coupled THMC Processes and Reactive Transport: FY14 Progress" (Rutqvist et al. 2014a) and have also been published in a journal paper (Vilarrasa et al., 2016).

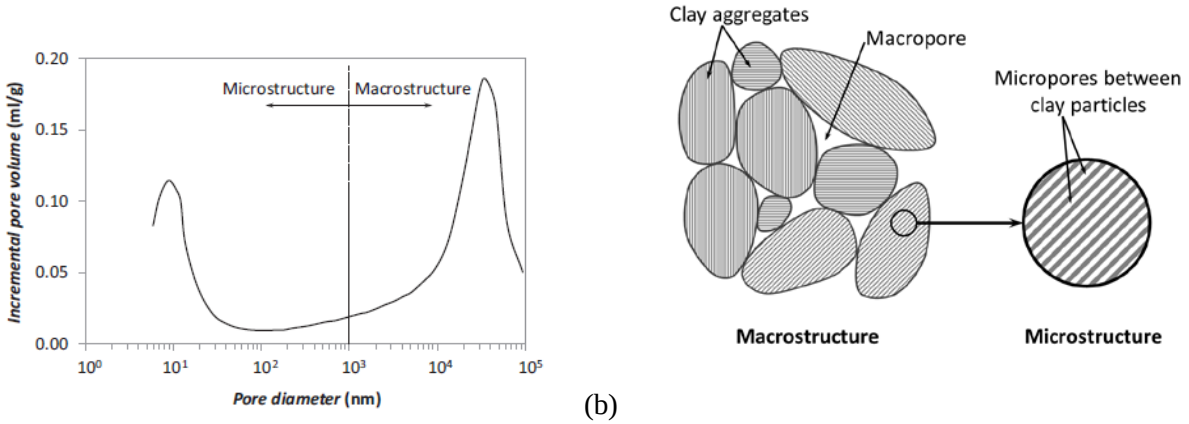

Figure 2-4. (a) Pore size distribution, and (b) schematic representation of the two structural levels considered in the dual structure model. Clay particles are represented by the gray lines (Vilarrasa et al., 2016).

The model implementation of BExM was further tested and validated as documented in the FY2016 milestone report titled "DR Argillite Disposal R&D at LBNL" (Zheng et al., 2016) by modeling (1) one swelling pressure test on Boom clay pellets, (2) two cyclic wetting-drying tests on one type of expansive clay, and (3) two tests with combination of loading paths on compacted bentonite samples. Based on the simulation results, the model is capable to reproduce the observed behavior of expansive clays during experiments associated with suction changes. The computation results we obtained with BExM agree well with the experiment data, and also follow the same tendency of results presented by BExM developers. However, considerable uncertainties still exists in the use of the BExM model, because of complexities in the underlying processes and the large number of parameters needed to define the constitutive dual-structure behavior of clays.

2.3 Shale Constitutive THM Models in TOUGH-FLAC

Through modeling of a number of *in situ* experiments at Mont Terri and Bure underground research laboratories (URL's), constitutive models for coupled THM behavior of clay stone (or shale) have been developed and adapted. Modeling of these *in situ* experiments and other field studies have shown that it is important to consider anisotropic properties of shale elasticity, strength, thermal conductivity, permeability and thermal expansion.

The FLAC3D ubiquitous joint model can handle anisotropic strength properties of shale, and this model has been commonly used for geomechanical modeling of Opalinus Clay at Mont Terri (Corcum and Martin, 2007). The theory and implementation of this model in FLAC3D is described in the FLAC3D manual (Itasca, 2011). The model accounts for the presence of an orientation of weakness (weak plane) in a Mohr-Coulomb constitutive model. The criterion for failure on the planes, of a given orientation is based on the escalation of a composite Mohr-Coulomb envelope with tension cutoff. The rock-strength input parameters includes fiction angle and tension cutoff with weaker properties for the weak (joint) planes compared to that of the intermediate intact rock. Figure 2-5 shows the results of a simulation involving a horizontal emplacement tunnel in Opalinus Clay with horizontal bedding (Rutqvist et al., 2014). On top and bottom of the emplacement tunnel we can see shear failure that occurred along bedding planes.

The results of modeling of heater experiments at Mont Terri and Bure showed the need to take into account anisotropic thermal conductivity to match temperature measurements at the experiments (Garitte et al., 2017). Anisotropic thermal conductivity is not standard in TOUGH2 and TOUGH-FLAC and was implemented into the TOUGH2 source code. Anisotropic permeability can be considered in the standard TOUGH2 code for rectilinear grid.

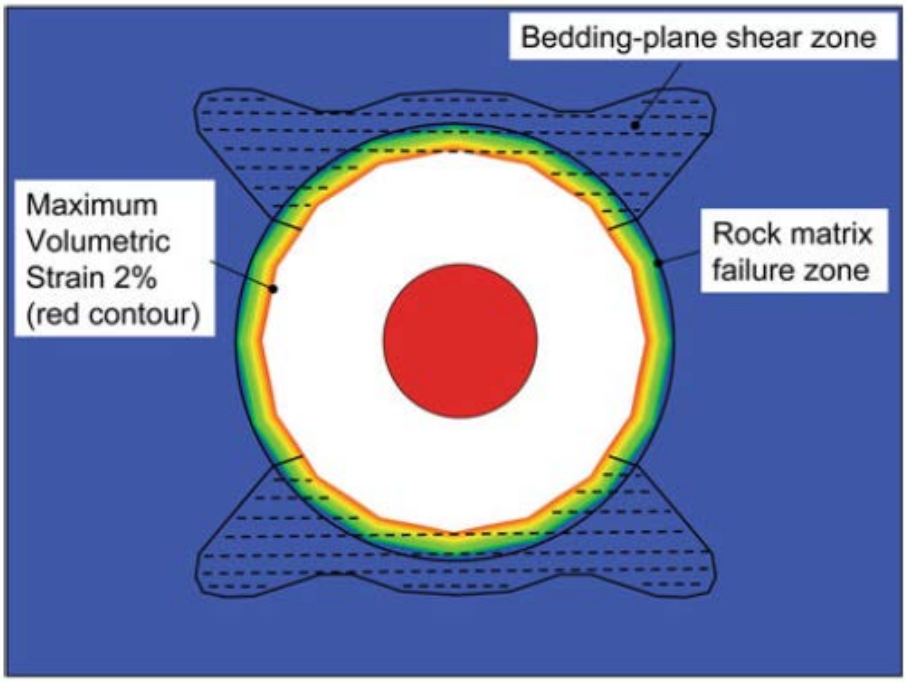

Figure 2-5. Volumetric strain contour and extent of failure zones related to horizontal bedding planes and rock matrix (Rutqvist et al., 2014).

2.4 EDZ Models in TOUGH-FLAC

The EDZ is one of the most important features taken into account in the performance assessment of repositories in argillite, and was assigned the highest research priority ranking in the 2012 UFD Road Map (Nutt, 2012). Models of different sophistications have been developed and applied to model the EDZ using TOUGH-FLAC, including

1) Empirical stress-permeability model;
2) Non-linear elastic and brittle failure model; and
3) Anisotropic continuum damage model.

The three models are summarized in the following subsections.

2.4.1 Empirical stress-permeability model

An empirical stress-permeability model calibrated against *in situ* EDZ data is described in Rutqvist (2015). The empirical EDZ model was applied in a previous phase of the DECOVALEX project related to nuclear waste disposal in crystalline rock (Rutqvist et al., 2009). The empirical EDZ model was calibrated against EDZ data from the TSX experiment conducted at the underground research laboratory in Manitoba, Canada (Martino et al., 2004).

The permeability around the tunnel was simulated using the empirical stress-permeability relationship in which permeability is a function of the effective mean stress, σ'_m, and deviatoric stress, σ_d, according to (Rutqvist et al., 2009):

$$k = [k_r + \Delta k_{\max} \exp(\beta_1 \sigma'_m)] \cdot \exp(\gamma \Delta \sigma_d) \tag{2.3}$$

where k_r is residual (or irreducible) permeability at high compressive mean stress, Δk_{max}, β_1 and γ are fitting constants, and $\Delta\sigma_d$ is the change in deviatoric stress relative to a critical deviatoric stress for onset of shear-induced permeability.

Figure 2-6 compares simulated and measured permeability changes for $\beta_1 = 4\times10^{-7}$ Pa^{-1}, $k_r = 2\times10^{-21}$ m^2, $\Delta k_{max} = 8\times10^{-17}$ m^2, $\gamma = 3\times10^{-7}$ Pa^{-1}, and with the critical deviatoric stress for onset of shear-induced permeability set to 55 MPa. The 55 MPa critical deviatoric stress roughly coincides with the extent of a cluster of microseismic events at the top of the tunnel and to about 0.3 of the instantaneous uniaxial compressive stress of small-scale core samples, which is consistent with the stress level at which crack initiation has been observed in studies of Lac du Bonnet granitic samples (Martin and Chandler, 1994).

Based on the relationship calibrated against field measurements of EDZ during excavation, a model prediction of the longer term EDZ evolution of a nuclear waste emplacement tunnel was conducted (Ngyuen et al., 2009). Figure 2-7 present the EDZ permeability distribution after excavation and at 1000 years after emplacement when the thermal-mechanical stress might be the highest. Figure 2-7 shows that there is some increase in EDZ permeability at 1000 years compared to that after excavation, though the changes are small.

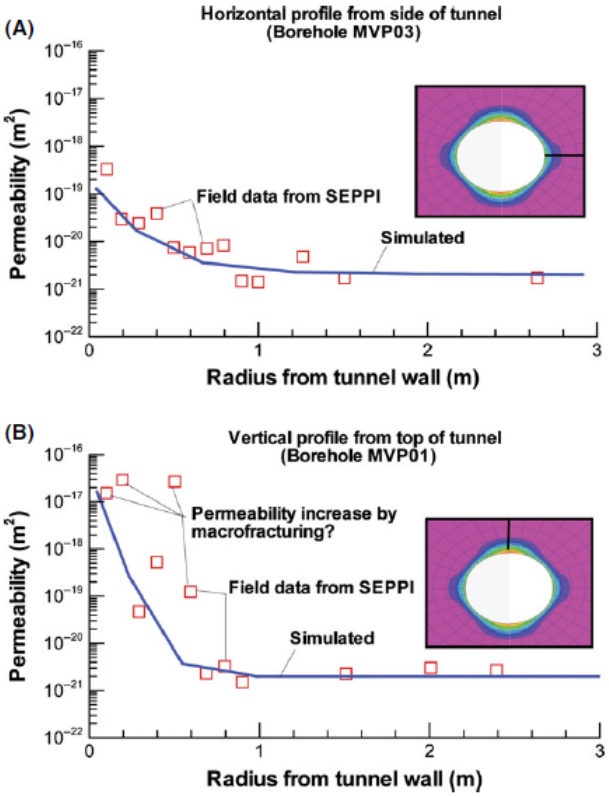

Figure 2-6. Simulated and measured permeability changes around the TSX tunnel (Rutqvist et al. 2009). Permeability versus radius along (A) a horizontal profile from the side of the tunnel, and (B) a vertical profile from the top of the tunnel.

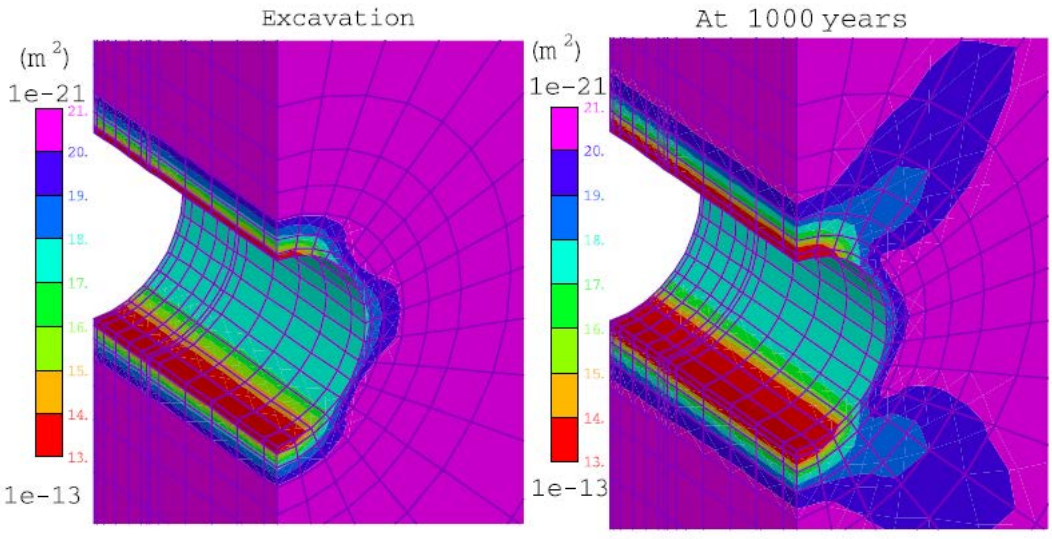

Figure 2-7. Calculated permeability distribution for generic repository emplacement tunnel in crystalline rocks using the empirical stress-permeability relation (Nguyen et al., 2009).

2.4.2 Non-linear elastic and brittle failure model

A non-linear elastic and brittle failure model was implemented in TOUGH-FLAC and demonstrated in the FY2012 Milestone Report titled "Report on Modeling Coupled Processes in the Near Field of a Clay Repository" (Liu et al., 2012). The non-linear elastic model, denoted the two-part Hooke's model (TPHM), provided a new constitutive relationship, and associated formulations regarding rock hydraulic/mechanical properties. The usefulness and validity of the TPHM were demonstrated by the consistence between simulation results and field observations at the Mont Terri URL. The brittle failure model was applied using a fine-grid numerical approach, based on the explicit incorporation of small-scale heterogeneity of mechanical properties. Using the combination of the TPHM and the fine-grid numerical approach of the results of investigations were compared with field results at Mont Terri.

Figure 2-8 shows the example of calculated brittle failure and permeability changes around a tunnel in a host rock representing Oplalinus Clay. The model simulation captured both the observed displacements and the size of the damage zone. Moreover, the fine-grid numerical approach, together with an explicit incorporation of the small-scale heterogeneity of mechanical properties, was able to capture the overall behavior of the EDZ, as demonstrated by the consistency between the simulated and the observed EDZ size, which was about 1 m on the side of the tunnel. The calculated hydraulic conductivity values are especially high in the EDZ within the tunnel sidewalls, varying between 2.39×10^{-14} m^2 and 7.45×10^{-13} m^2, is consistent with measured data at the Mont Terri Laboratory (Bossart et al., 2002; Bossart et al., 2004). Such a model validated against field data could also be used to calculate EDZ evolution over the longer term. However, while the current model addresses permeability changes induced during excavation, it does not address sealing and healing processes that might be important over the long term.

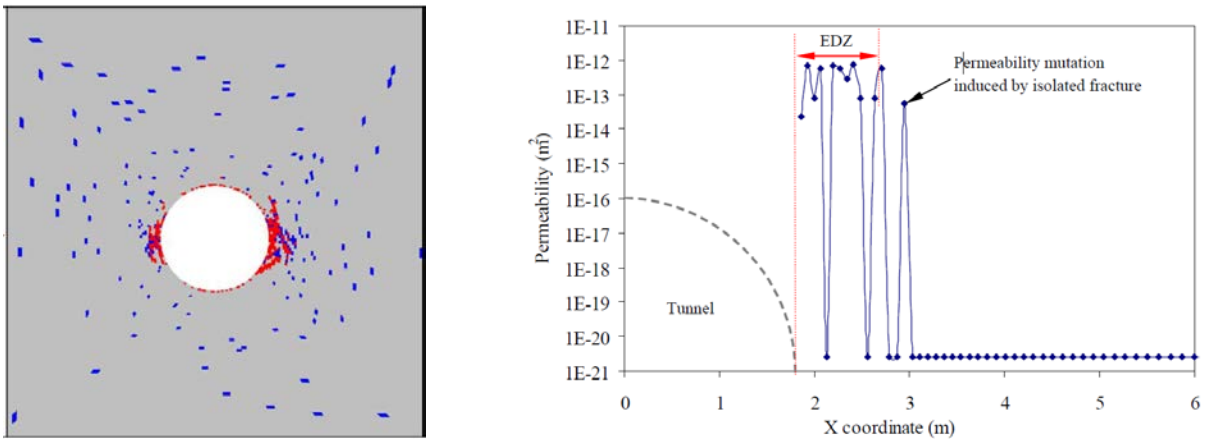

(a) (b)

Figure 2-8. (a) Calculated brittle failure and (b) permeability changes around an excavation in argillite (Liu et al., 2012).

2.4.3 Anisotropic continuum damage model

In FY2017, an anisotropic damage model named Deviatoric Stress Induced Damage (DSID) was implemented into the simulator to account for crack propagation due to microstructure changes (Zheng et al., 2017). This new damage model is hyper-elastic, i.e., the stress-strain relationship was derived from the expression of a thermodynamic potential, and was derived based on Continuum Damage Mechanics (CDM), which avoids to model cracks at the micro-scale, as opposed to micro-mechanics. Damage effects are analyzed at the scale of Representative Elementary Volume (REV) with the concept of effective stress to account for the reduction of undamaged areas (Chaboche, 1992). REV is the smallest volume over which a measurement can be made that will yield a value representative of the whole, and it ranges from 10^{-3} m to 0.1 m, depending on the material and the focused problem. The model implementation has been validated by comparison with modeling several laboratory experiments on granite and by comparing computation results with different codes. The agreements on simulation results proved the damage model was implemented correctly in our simulator and was capable to reproduce the same non-linear mechanical behavior due to damage propagation. For instance, the damage model was utilized to predict the evolution of the disturbed rock zone (DRZ) around emplacement tunnels, where the model enabled to capture the micro-crack propagation induced by the excavation (Figure 2-9).

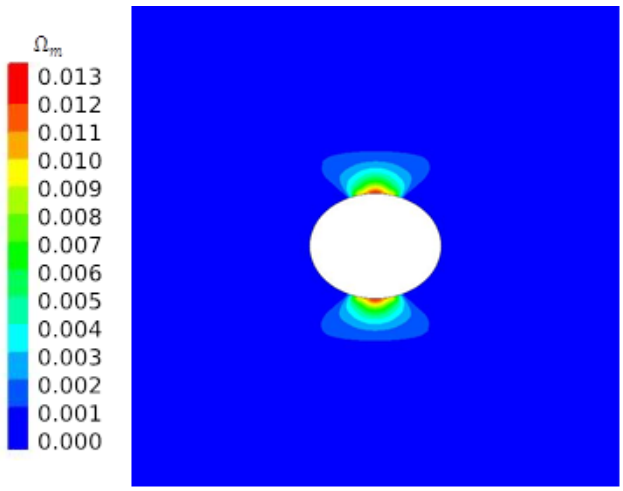

Figure 2-9. The simulation result of damage distribution at TSX experiment.

This page intentionally left blank.

3. STATUS OF TOUGH-RBSN SIMULATOR FOR COUPLED FRACTURING PROCESSES

The TOUGH-RBSN simulator (Asahina et al., 2014; Kim et al., 2017) has been used for modeling coupled THM processes related with fracture/damage behavior. The individual physical processes related to fracture propagation are represented by separate program modules: the TOUGH2 code for multiphase flow and mass transport based on the finite volume approach; and the rigid-body-spring network (RBSN) model for mechanical and fracture-damage behavior, which are sequentially coupled with each other. The discrete fracture network (DFN) approach is adopted in the coupling procedure, where fractures have enhanced flow properties as well as degraded mechanical properties in a discrete manner. This section presents more details on the TOUGH-RBSN simulator, including the status of the numerical framework for THM coupling procedure, modeling of discrete fractures for enhanced flow in the TOUGH2 code, and fracture determination in the RBSN approach.

3.1 TOUGH-RBSN Coupling Procedure

Figure 3-1 shows a schematic flow diagram of the coupling procedure between the TOUGH2 and RBSN codes. Coupling modules are implemented in each side of the modeling codes, by which material properties and mechanical boundary conditions are updated with the outputs of primary variables of physical quantities. Pore pressure and degree of saturation are primary variables of the TOUGH2 analysis, which are involved in the RBSN simulation to determine the effective stress and swelling/shrinkage strain. In return, the primary variables of the RBSN model, stress/strain states, damage index, and fracture aperture, are used to evaluate hydrological properties and conditions for the TOUGH2 simulation.

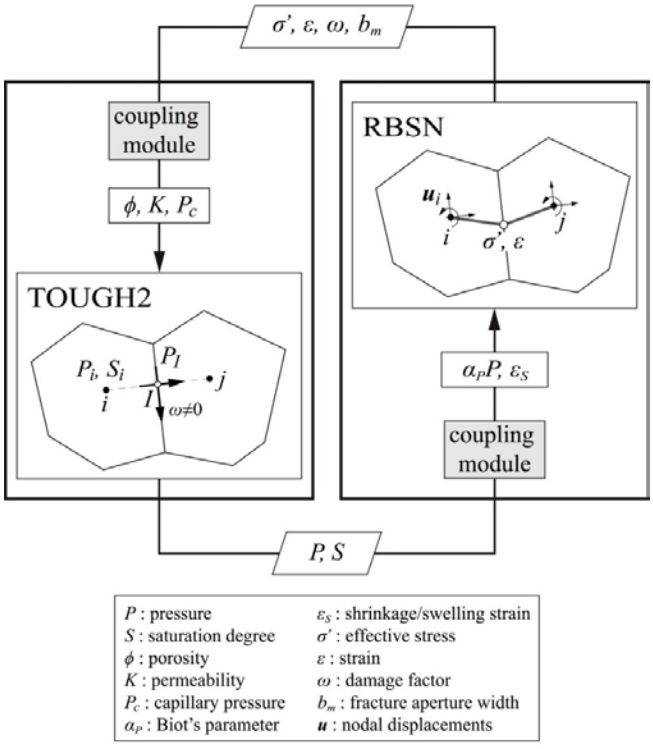

Figure 3-1. Coupling procedure of the TOUGH-RBSN simulator (adapted from Kim et al., 2017).

First, the TOUGH2 to RBSN link supplies pressure and degree of saturation to update the mechanical quantities. Based on the linear poro-elasticity theory, the effective (grain-to-grain) stress $\sigma_n{}'$ is calculated from the pore pressure P (Biot and Willis, 1957):

$$\sigma_n{}' = \sigma_n + \alpha_p P \tag{3.1}$$

where σ_n is the total normal stress obtained from overall loading, including external loads; α_p is Biot's effective stress parameter. Note that tensile stress is taken to be positive for the sign convention. Also, the shrinkage/swelling effect due to the local changes of liquid saturations ΔS can be taken into account:

$$\Delta\varepsilon_s = \alpha_s \Delta S \tag{3.2}$$

where ε_s is shrinkage/swelling strain; and α_s is the moisture swelling coefficient. If a poro-elastic geomaterial is subjected to confinement conditions, the stress due to swelling/shrinkage can be calculated as

$$\Delta\sigma' = \Delta\varepsilon_s E \tag{3.3}$$

where E is the Young's modulus.

The fracture process of a local rigid-body-spring element is realized by degrading the springs. A fracture event entails a reduction of spring stiffnesses and a release of the associated elemental forces. For the degraded spring set, the modified stiffness matrix $\mathbf{D}'$ is

$$\mathbf{D}' = (1 - \omega)\mathbf{D} \tag{3.4}$$

where ω is a scalar damage index with a range from zero (undamaged) to 1 (completely damaged). For brittle fracturing, which is applied to the cases presented in this report, ω is directly switched from 0 to 1 once a fracture event occurs (i.e., the stress state of an element violate the failure criteria).

Next, the RBSN to TOUGH2 link supplies the effective stress and the strain calculated in the lattice element to update the hydrological properties of the corresponding TOUGH2 grid blocks *i* and *j* on the left side of Figure 3-1. Porosity, permeability, and capillary pressure are generally related with the effective stress and strain values (Rutqvist and Tsang, 2002).

If fracturing occurs at element *ij* (i.e., $\omega \neq 0$), the associated fracture node *I* and additional connections are activated in the TOUGH2 model. The permeability of an individual fracture depends on the hydraulic aperture b_h (Witherspoon et al., 1980). According to a parallel-plate model, the fracture permeability is defined as $b^2/12$. The hydraulic aperture is coupled to the mechanical aperture b_m (Rutqvist et al., 1998, 2000):

$$b_h = f(b_r + \langle b_m - b_r \rangle) \tag{3.5}$$

where $\langle x \rangle = 1/2(x + |x|)$ represents Macaulay brackets, and b_r is the residual hydraulic aperture. $f \leq 1.0$ is a dimensionless factor that accounts for the slowdown of flow in a natural rough fracture in comparison to the ideal case of parallel smooth fracture surfaces.

In the TOUGH-RBSN sequential coupling, TOUGH2 is a main driver of analysis, which controls the time stepping during the coupling procedure, while the RBSN approach solves the mechanical response as a quasi-static process at each time step. The selection of small time steps is important to find stable

solutions of the mechanical response, so the TOUGH2 input defines the upper limit for time step size with a small value to avoid any abrupt change of hydrological conditions over time steps.

3.2 Model Discretization and Discrete Fracture Representation

The computational domain for both the TOUGH2 and RBSN calculations is tessellated using a Voronoi diagram (Okabe et al.,2000). The discretization process is carried out basically in three Steps: 1) nodal point insertion, 2) Delaunay tessellation, and 3) Voronoi discretization. Within the domain, nodal points are positioned in regular or irregular formation. Introducing a parameter for minimum allowable distance can define the desired nodal density of the unstructured grid. The Delaunay tessellation is conducted based on the nodal positions, where each Delaunay edge defines the nodal connection of the corresponding lattice element. Through the dual Voronoi tessellation, the spatial domain is collectively filled with discrete polyhedral cells that render the elemental volumes. More detailed procedure of the domain partitioning is presented elsewhere (Yip et al., 2005; Asahina and Bolander, 2011).

For the discrete fracture network (DFN) approach, fractures and such discontinuities are explicitly modeled within the Voronoi grid. Voronoi cells generally represent the matrix component in a geomaterial constitution, and pre-existing or newly generated fractures are placed on the Voronoi cell boundaries. The geometry of fracture networks (e.g., orientation, length, curvature) can be obtained by observational mapping data, computer-generated statistical reproductions, or mechanical simulation results. An example of the discretization procedure in 2D modeling involving a straight fracture is as follows:

1. Generate a Voronoi unstructured grid for the spatial domain,
2. Overlay the reference fracture trajectory onto the grid,
3. Test all connections of natural neighboring nodes to check if they cross the fracture. For example, compare connections *ij* and *jk* in Figure 3-2, and
4. Collect the Voronoi cell boundaries corresponding to the nodal connections that cross the reference fracture (such as *ij*) and form discretized fractures.

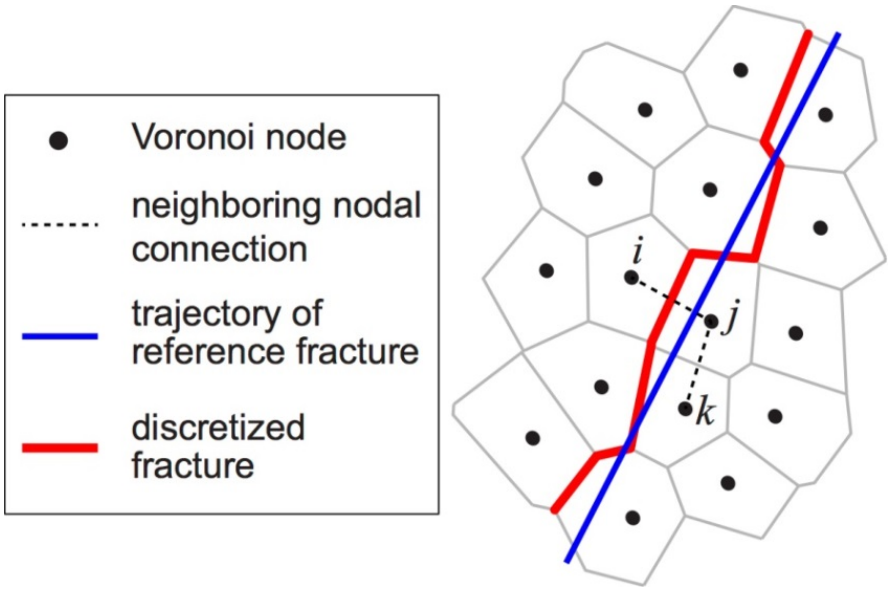

Figure 3-2. Fracture mapping and discretization within an unstructured Voronoi grid (adapted from Asahina et al., 2014).

By repeating the above process for multiple fractures, a network of discrete fractures can be generated. This fracture discretization process is completely automated and can be easily extended to more complicated geometries in 3D modeling. However, the grid size should be carefully chosen to obtain a sufficiently precise representation of the reference fracture. A finer grid can accommodate the discretized fractures that conform more closely to the reference fracture.

In the simulations using a grid structure of the ordinary Voronoi discretization, flow and mass transfer are enacted only through the connections of the neighboring Voronoi nodes (called cell-cell connections in Figure 3-3a. However, if fracturing occurs within the matrix, substantially enhanced flow may arise through the fracture path. In order to demonstrate the accelerate flow in the DFN approach, the grid structure is modified, for which additional interface nodes and the associated connections are introduced. As shown in Figure 3-3b, an interface node with increased permeability is inserted where the cell-cell connection intersects the Voronoi cell boundary. The original cell-cell connection is divided into two cell-interface (and vice versa) connections by the interface node. In addition, the connections between the interface nodes are established to activate flow channels in discrete fractures.

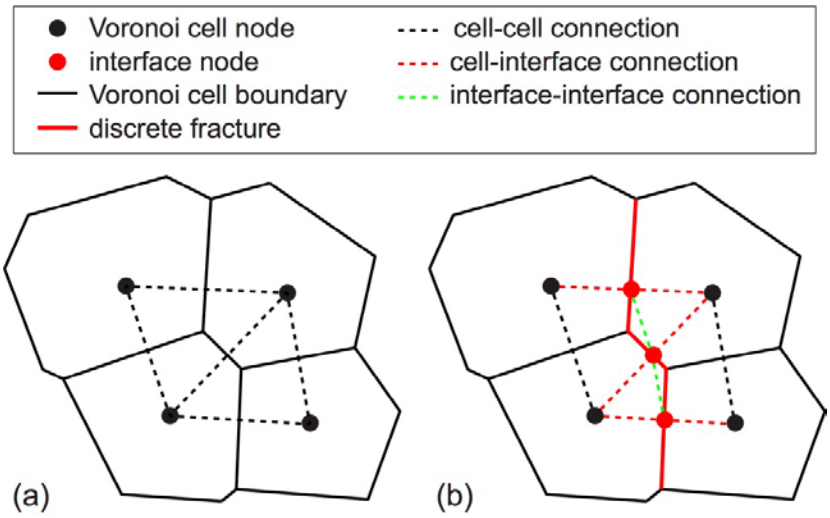

Figure 3-3. Transformation of the grid structure for enhanced flow through discrete fractures: (a) original Voronoi cell nodes and connections; and (b) insertion of interface nodes and connections.

3.3 Stress Calculation and Fracture Determination in the RBSN Approach

Elasticity and fracture-damage of geomaterials are modeled using the rigid-body-spring network (RBSN) approach. As a discrete modeling approach, the RBSN represents the mechanical system by a collection of simple lattice (two-node) elements. The lattice topology is defined by the Delaunay tessellation, and the dual Voronoi diagram is used to render the volume of a discretized domain (Figure 3-4a). The elemental formulations are based on the rigid-body-spring concept (Kawai, 1978; Bolander and Saito, 1998). A lattice element consists of a zero-size spring set located at the centroid of the common Voronoi cell boundary and two rigid arm constraints that relate the spring set to the nodes (Figure 3-4b). For 3D modeling, a spring set is formed from three axial springs and three rotational springs in local $n - s - t$ coordinates (Figure 3-4c). The $n-$axis is normal, and the $s - t$ plane is parallel to the Voronoi cell boundary.

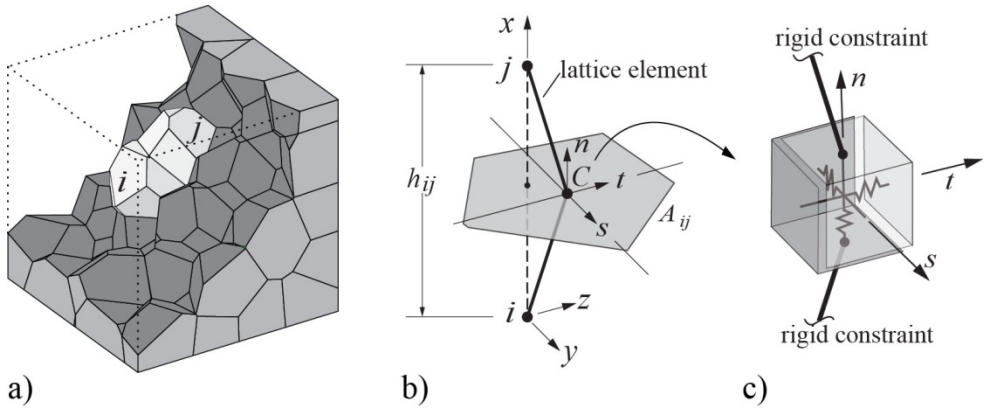

Figure 3-4. Typical RBSN lattice element *ij*: (a) within a Voronoi grid; (b) isolated from the network; and (c) a zero-size spring set located at centroid *C* of Voronoi cell boundary area A_{ij}.

A diagonal matrix $\mathbf{D} = \mathrm{diag}[k_s, k_t, k_n, k_{\phi n}, k_{\phi s}, k_{\phi t}]$ consists of the six spring coefficients which are defined according to the geometrical properties of Voronoi diagram:

$$k_s = k_t = \alpha_1 k_n = \alpha_1 \alpha_2 E \frac{A_{ij}}{h_{ij}}, \quad k_{\phi n} = E \frac{J_p}{h_{ij}}, \quad k_{\phi s} = E \frac{I_{ss}}{h_{ij}}, \quad k_{\phi t} = E \frac{I_{tt}}{h_{ij}} \tag{3.6}$$

where E is the elastic modulus, J_p, I_{ss}, and I_{tt} are the polar and two principal moments of inertia of the Voronoi cell boundary with respect to the centroid, respectively. The spring coefficients are scaled by the element length h_{ij} and the area of the Voronoi cell boundary A_{ij}. Effective Poisson ratio can be represented by adjusting α_1 and α_2. By setting $\alpha_1 = \alpha_2 = 1$, the models behave with elastic homogeneity under uniform straining, albeit with zero effective Poisson ratio (Asahina and Bolander, 2011; Kim and Lim, 2011).

Fracture may initiate within a lattice element when the stress state exceeds the given material strength. To determine the criticality of the stress state, a stress ratio is calculated for each lattice element:

$$R_f = \sigma_e / \hat{\sigma} \tag{3.7}$$

where σ_e is the element stress state and $\hat{\sigma}$ is the critical stress defined by fracture criteria. During iterative calculations, only one element, with the most critical stress state (i.e., the largest $R_f \geq 1$), is allowed to break per iteration, and the fracture event entails a reduction of spring stiffnesses and a release of the associated elemental forces. Various user-defined fracture models can be applied to evaluate stress of lattice elements and set the critical stress related to the material strength parameters. Strength properties of each element are determined as critical stress components on a Mohr-Coulomb surface. Figure 3-5 shows the fracture surface with a tension cut-off, where the envelop is defined by three parameters: the angle of internal friction ψ (surface inclination with respect to σ_n-axis); cohesive strength c (surface intersection with the shear axes); and the tensile strength f_n. Herein, two different types of stress evaluation are described within the Mohr-Coulomb based failure criteria.

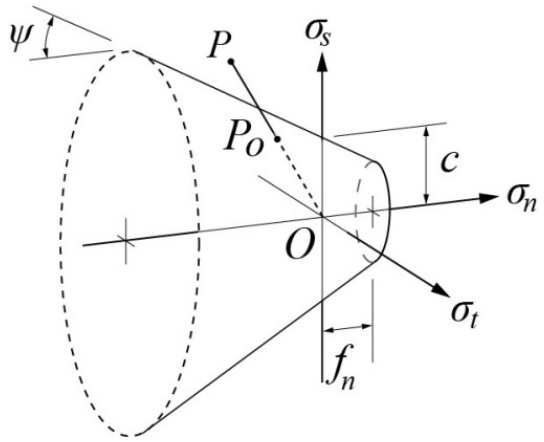

Figure 3-5. Mohr-Coulomb fracture surface with tension cut-off.

The first type is so-called the vectorial stress measurement, which uses the spring force vector for normal and shear stress components. Measures of stress $P(\sigma_n, \sigma_s, \sigma_t)$ are derived by averaging the axial spring forces F_n, F_s, and F_t over the cell boundary area A_{ij}. The criticality of the stress state is assessed as $R_f = \overline{OP}/\overline{OP_O}$, where P_O is the point at which $\overline{OP}$ intersects the fracture surface (see Figure 3-5). At the present stage of model development, there is no option to gradually damage the springs (e.g., with softening behavior) for fracture softening. However, other studies have indicated the possibility of modeling damage process by shrinking the Mohr-Coulomb surface (Shen and Shen, 2002; Kim and Lim, 2011).

The second type is to calculate the stress tensor for each nodal point, so-called the tensorial stress measurement. Stress tensors at Voronoi cell nodes are possible by considering the equilibrium conditions of the spring forces. Sets of the spring forces are applied at the boundaries surrounding a Voronoi cell (Figure 3-6 a), and nodal force components F_{nn}, F_{ns}, and F_{nt} can be calculated for an arbitrary section passing through the Voronoi cell node with its corresponding local $n - s - t$ coordinates, which satisfy the equilibrium condition with all the forces acting on the remaining cell boundaries (Figure 3-6b). Moment contributions to equilibrium are not considered here. By dividing these force components by the cut-face area, the corresponding stress components σ_n, σ_s, and σ_t can be obtained. By repeating this process for three mutually perpendicular sections, the full stress tensor is obtained (Figure 3-6c). Details are given elsewhere (Yip et al., 2005). From the stress tensors at two neighboring nodes, the stress tensor of the inter-element is calculated according to

$$\bar{\boldsymbol{\sigma}} = (\boldsymbol{\sigma}_i + \boldsymbol{\sigma}_j)/2 \tag{3.8}$$

where $\boldsymbol{\sigma}_i$ and $\boldsymbol{\sigma}_j$ are the stress tensors at the neighboring nodes i and j, respectively. The maximum principal tensile stress of $\bar{\boldsymbol{\sigma}}$ serves as σ_e in Equation (3.8). In this way, fracture under multiaxial stress conditions can be simulated. Note that the gas migration simulations using TOUGH-RBSN, presented in Section 6, have adopted this tensorial stress measurement for fracture determination.

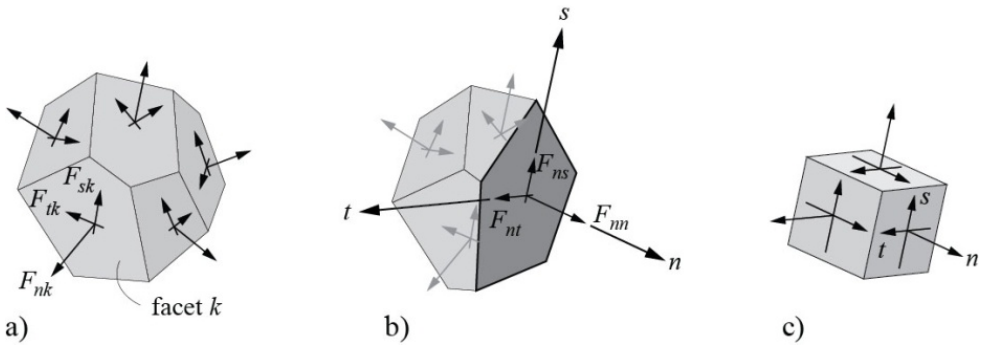

Figure 3-6. Stress tensor measurement at a Voronoi cell node: (a) components of spring force local coordinates; (b) a set of nodal forces satisfying the equilibrium; and (c) complete stress tensor at Voronoi cell node (adapted from Yip et al., 2005).

3.4 Status of TOUGH-RBSN Verification and Validation

Coupled THM processes, including fracture propagation, within argillaceous rocks and clay rich geomaterials have been simulated using the TOUGH-RBSN code with adequate constitutive models, which are verified and validated against laboratory tests and analytic solutions. In the following, completed verifications and validations of TOUGH-RBSN are listed with the references in which those activities are documented.

- Simulations of swelling stress development and desiccation cracking in geomaterials validated against independent laboratory test data (Asahina et al., 2014)
- Hydraulic fracture propagation in rock-analogue samples made of soda-lime glass with a designed fracture geometry (Kim et al., 2017)

In addition, LBNL is currently involved in DECOVALEX-2019, an international collaborative activity for validating various modeling approaches against unique laboratory and field data. TOUGH-RBSN has been used to model two-phase liquid and gas flow in saturated bentonite sample with dilatant flow path and fracture generation. Intermediate results have been presented in Tamayo-Mas et al. (2018), where extensive comparisons of simulation results using 11 different modeling approaches are made with laboratory test data. The TOUGH-RBSN models with relevant conceptual models exhibit key responses such as pressure/stress evolutions in a plausible match with the experimental data, which will be presented in Section 6.

This page intentionally left blank.

4. FE EXPERIMENT AT THE MONT TERRI SITE (MONT TERRI PROJECT)

In this section, we present the current status of the FE Experiment at Mont Terri and updated TOUGH-FLAC modeling of the experiment. In particular, in FY2018 we have extended the modeling for comparison with up to 3.5 years of field data from the experiment at additional monitoring points within the bentonite buffer and surrounding host rock. In the following, we first provide a description and status of the FE Experiment and then present the results of current THM modeling.

4.1 Description and Status of the Mont Terri FE experiment

The Mont Terri FE experiment is undertaken by NAGRA, Switzerland, as an ultimate test for the performance of geologic disposal in Opalinus Clay, with focus on both the EBS components and the host-rock behavior. It will be one of the largest and longest-duration heater tests worldwide, with focus on both the EBS components and the host-rock behavior. The FE experiment is conducted in a side tunnel at Mont Terri, excavated along the claystone bedding planes, extending 50 m in length and about 2.8 m in diameter (Figure 4-1). Heating from emplaced waste is simulated by three heat-producing canisters of 1500 W maximum power. The temperature is expected to exceed 100°C, with a target temperature of 125 to 135°C at the inner parts of the buffer. A sophisticated monitoring program has been implemented, including dense instrumentation of the bentonite buffer and host rock, and extensive geophysical monitoring.

The experiment will provide data useful for the validation of THM coupling effects regarding the processes in the host rock, while correctly accounting for (and examining) the conditions in the emplacement tunnel temperature, saturation, and swelling pressure. Due to the 1:1 scale of the experiment, it will be possible to achieve realistic temperature, saturation, and stress gradients. It will also be possible to test backfilling technology with granular bentonite, as well as lining technology with shotcrete, anchors, and steel ribs. Processes examined in the test cover many aspects of repository evolution, such as creation and desaturation of the EDZ during tunnel excavation and operation (including ventilation for about one year), as well as reconsolidation of the EDZ, resaturation, thermal stresses, and thermal pore-pressure increase after backfilling and heating (heating and monitoring period > 10 years).

In 2011, a niche in front of the FE tunnel was constructed, followed by a first phase of instrumentation of the rock mass surrounding the tunnel, using boreholes from the niche. The FE tunnel was then excavated by road-header in 2012; which was followed by another phase of instrumentation. The tunnel was open for a one-year ventilation period. This was followed by the emplacement of the heaters, bentonite buffer, and a concrete plug, after which the heating was gradually turned on during the fall of 2014 and early 2015, with full heat power of 1350 W at all three heaters (H1, H2, H3) from February 18, 2015 (Figure 4-2). The heating is expected to go on for at least 15 years, with continuous monitoring of THM processes in both the bentonite buffer and surrounding rock.

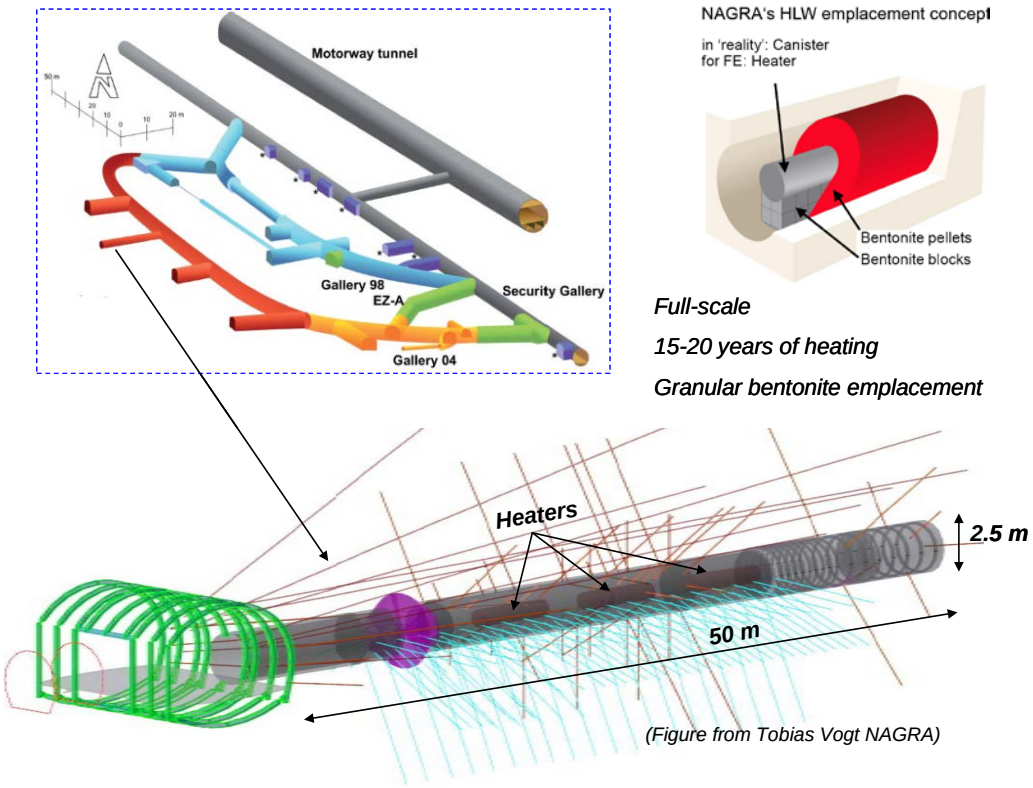

Figure 4-1. Plan view of FE experiment setup and borehole layout.

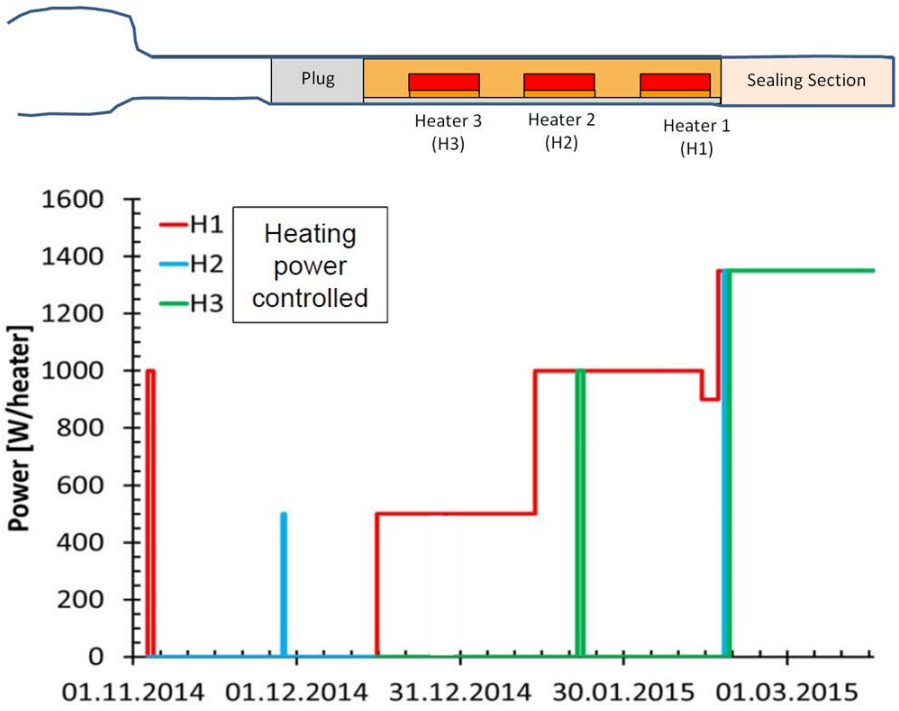

Figure 4-2. Heat power applied to H1, 2 and 3 during heater start-up at the Mont Terri FE experiment.

4.2 Progress of LBNL Modeling of FE Experiment

DOE is one of the experimental partners for the FE heater experiment, and LBNL is one of the modeling teams. In addition to LBNL, six other modeling teams are currently involved in the Mont Terri FE experiment from Germany (2 teams), U.K., Spain, Switzerland, and Canada.

Each modeling team develops its conceptual models and material properties using available literature (papers and reports) on lab experiments and previous Mont Terri *in situ* tests, etc. In the FY2013 UFD milestone report (Houseworth et al., 2013), we also made a first full THM 3D simulation of the FE heater test, including the BBM model for calculating the mechanical responses. These were scoping and preliminary predictions with the material properties available at the time, though in some cases including a different kind of bentonite.

In the FY2015 UFD milestone report (Zheng et al., 2015), we presented simulation results related to the thermal evolution for different heat power schemes. This included a staged heating during the first few months of the experiment. A staged heating schedule was also adopted in the real experiment to be able to use early data for determining the maximum heat load so that temperatures would not exceed certain limits. For example, the maximum temperature should not exceed 150°C as such high temperature could potentially damage the monitoring system. The modeling presented in the FY2015 UFD milestone report indeed showed that temperature could increase to about 150°C if the maximum heat power of 1500 W would be applied on each of the heaters. It was decided by NAGRA to limit the maximum heat power to 1350 W to maintain maximum temperature well below 150°C.

In the FY2016 UFD milestone report (Zheng et al., 2016), we presented the results of initial interpretative modeling of the FE experiment with comparison to field data for the first year of heating. The approach was to use the previously developed 3D model of the FE experiment, but with THM properties updated and determined from the modeling of the smaller scale HE-E experiment. In the modeling, we obtained a good agreement with monitored evolution of temperature and relative humidity, when using an effective diffusivity that was lowered using a tortuosity factor as low as 0.14 (Zheng et al., 2016).

In the FY2017 SFWSD milestone report (Zheng et al., 2017), we updated model simulations with comparison to monitoring data extended to more than two years, including additional comparison for monitoring points located at other sections along the tunnel, i.e., comparisons made at monitoring sections located at all three heaters. The agreement between modeling and experimental data for temperature and relatively humidity was generally good, though some disagreement was found related to the relative humidity evolution in the bentonite blocks below the heaters.

In this report, we present updated model simulations with comparison to monitoring data extended to about 3.5 years, including additional comparison for monitoring points located in the buffer as well as in the host rock. We have also conducted additional sensitivity analysis and obtained a better match of relative humidity evolution in the bentonite blocks below the heaters.

4.3 TOUGH-FLAC Model of the Mont Terri FE Experiment

For the modeling of the FE experiment, we have developed a conceptual model and modeling approach that were presented in previous milestone reports (Houseworth et al., 2013; Zheng et al., 2014; Zheng et al., 2015; Zheng et al., 2016). The host rock is modeled using TOUGH-FLAC with anisotropic properties considering bedding planes of the Opalinus Clay. To accurately model anisotropic thermal and hydrological behavior, we created an inclined TOUGH2 mesh. Anisotropic mechanical material behavior is simulated using the FLAC3D ubiquitous joint model, with initial material properties derived from the excavation design analysis of the experimental tunnels. In the ubiquitous joint model, weak planes are assumed along the bedding planes of the Opalinus Clay, in which the shear strength properties are different along bedding versus across bedding (Houseworth et al. 2013). For the bentonite, we started

with the BBM model as applied by the CINEMAT and Universitat Politècnica de Catalunya (UPC) (Garitte and Gens, 2012), and derived specific input material parameters for the MX-80 bentonite pellets, which is used as the emplaced buffer around the heaters. With this modeling approach, we are able to simulate THM processes in both the bentonite and host rock, as well as their interactions.

Figure 4-3 presents the 3D TOUGH-FLAC numerical grid of the FE experiment. This model grid includes all vital material components for the modeling of the FE experiment, including layered Opalinus Clay host rock, excavation disturbed zone, tunnel, three heaters, bentonite buffer, concrete liner, and concrete plug. The initial conditions for the model simulation are 2 MPa pore-fluid pressure and 15°C temperature for the host rock. The 2 MPa pore pressure is not under hydrostatic conditions, and the process is affected by the existing tunnel system at the site. In our simulations, we first run a simulation with an open tunnel at atmospheric pressure for one year, creating a pressure drop and hydraulic gradient around the tunnel. Thereafter, we assume instantaneous emplacement of the heater and buffer, and start our heating simulation.

The thermal and hydraulic material properties for modeling the FE experiment are given in Table 4-1. These properties are based on the modeling studies of several other smaller scale heater experiments at the Mont Terri laboratory, including the HE-D and HE-E experiments described in previous reports (Zheng et al., 2015; 2016). The intrinsic permeability of gas flow in the bentonite is about six orders of magnitude higher than the intrinsic permeability for liquid flow, and this is simulated in TOUGH2 using a high value of the Klinkenberg parameter. The initial saturation in granular bentonite and bentonite block are different that in the previous HE-E experiment, and is for the FE experiment set to 16.5% for granular bentonite and to 75% for bentonite blocks.

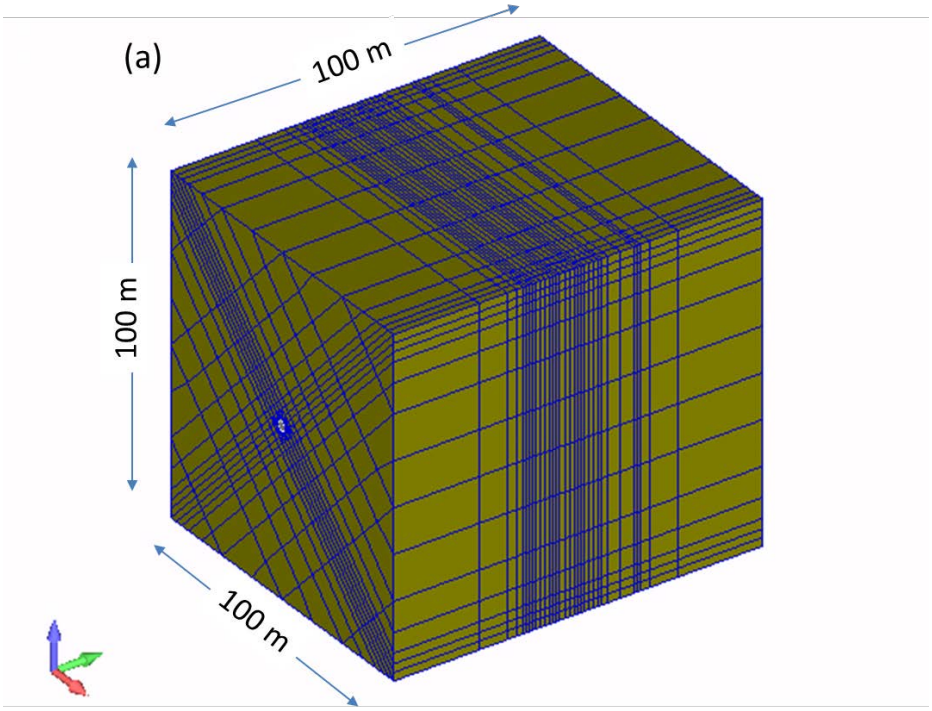

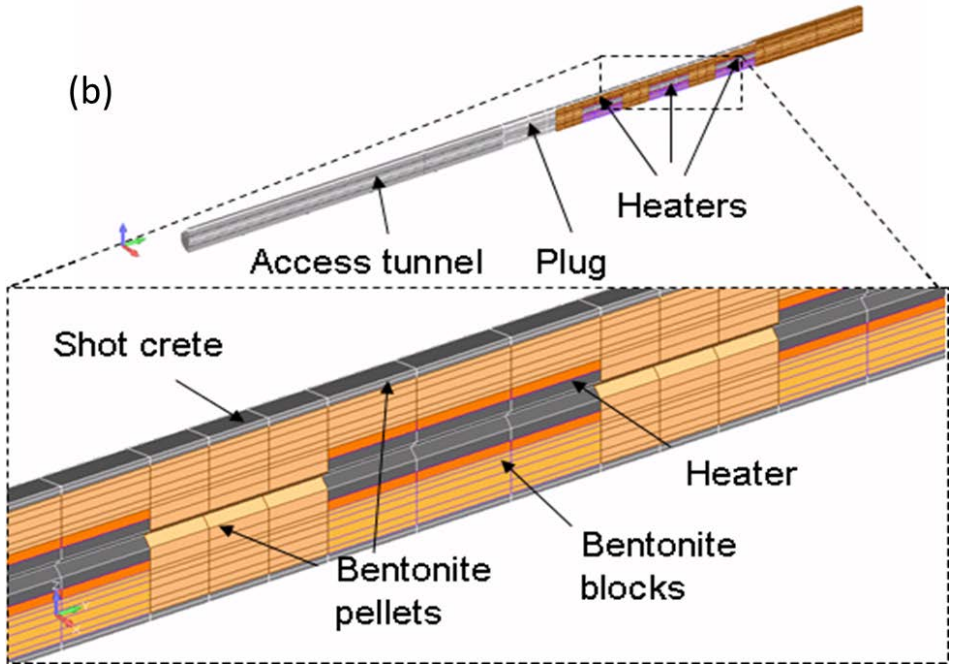

Figure 4-3. TOUGH-FLAC 3D numerical grid of the FE experiment. (a) entire model and (b) details of the materials and gridding of the EBS.

Table 4-1. Parameters used in the modeling of the Mont Terri FE experiment.

Parameters	Symbol	Opalinus Clay	Granular Bentonite	Bentonite blocks	Concrete (shotcrete and plugs)	Unit
Grain density	ρ_g	2.7×10^3	2.7×10^3	2.7×10^3	2.7×10^3	kg/m^3
Porosity	Ø	0.15	0.46	0.389	0.15	-
Intrinsic permeability	k	5.0×10^{-20}	5.0×10^{-21}	2.0×10^{-21}	3.5 x 10^{-21}	m^2
Liquid relative permeability (Corey, 1954) $k_{lr}(S_l) = \left(\frac{S_l - S_{lr}}{S_{ls} - S_{lr}}\right)^A$	A	-	5	3	-	-
Liquid relative permeability (van Genuchten, 1980) $k_{lr}(S_l) = \left(\frac{S_l - S_{lr}}{S_{ls} - S_{lr}}\right)^{1/2}\left[1 - \left\{1 - \left(\frac{S_l - S_{lr}}{S_{sl} - S_{lr}}\right)^{1/m}\right\}^m\right]^2$	m	0.52	-	-	0.52	-
Capillary curve (van Genuchten, 1980) $\psi(S_l) = Po\left\{\left(\frac{S_l - S_{lr}}{S_{ls} - S_{lr}}\right)^{-1/m} - 1\right\}^{1-m}$	P_0	1.09×10^7	1.0×10^7	3.0×10^7	1.09×10^7	Pa
	M	0.29	0.4	0.32	0.29	-
	S_{ls}	1.0	1.0	1.0	1.0	-
	S_{lr}	0.01	0.0	0.0	0.01	-
Thermal conductivity (wet)	λ_{sat}	1.7	1.3	1.0	1.7	W/m°K
Thermal conductivity (dry)	λ_{dry}	1.06	0.3	0.5	1.06	W/m°K
Grain specific heat	C	800	950	950	800	J/kg°K

4.4 Simulation Results with Comparison to Monitored Data

Here we first focus on the simulation and monitored data for the evolution of temperature and relative humidity in the bentonite buffer. A conceptual model of the evolution of moisture content is shown in Figure 4-4. The figure shows the creation of a thermal gradient due to the heating. Near the heater, liquid evaporates to vapor in the gas phase, which is then transported outwards by diffusion toward cooler regions where some of the vapor is condensed to liquid. At the same time, liquid water infiltrates from the rock into the bentonite buffer. The wetting of the outer parts of the buffer and the drying of the inner parts cause gradients in liquid saturation and capillary pressure, which will result in liquid fluid flow from the outer parts towards the inner dryer parts of the buffer.

The outward vapor diffusion is modeled in TOUGH2 using the following equation:

$$\mathbf{i}_g^w = -\rho_g \phi S_g \tau D_g^w \mathbf{I} \nabla X_g^w \tag{4-1}$$

where $\mathbf{i}_g^w$ is diffusion of water component in the gas phase, ρ_g is density of gas, ϕ is porosity, S_g is gas saturation, τ is flow tortuosity factor, D_g^w is water vapor diffusion coefficient, X_g^w is mass fraction of water in the gas phase, and **I** indicates the second order identity tensor. The vapor diffusion is from areas of high mass fraction of water vapor in the gas phase (near the heater) toward outer regions of the buffer of lower mass fraction of water vapor in the gas phase. Effective vapor diffusion for the partially saturated porous media is affected by porosity, gas saturation and the flow tortuosity factor (see also Figure 4-4).

The liquid flux from the outer parts of the buffer toward the inner parts is governed by the following equation:

$$\mathbf{q}_l^w = -\rho_l X_l^w \frac{\mathbf{k} k_{rl}}{\mu_l} \left(\nabla P_l - \rho_l \mathbf{g} \nabla z \right) \tag{4-2}$$

where $\mathbf{q}_l^w$ is the liquid water mass flux, ρ_l is density of liquid, X_l^w is mass fraction of water in liquid phase, **k** is intrinsic permeability, k_{rl} is relative permeability for liquid flow, μ_l is dynamic fluid viscosity, P_l is liquid pressure, ***g*** is acceleration from gravity, and z is elevation. The liquid flux is driven by the liquid pressure gradient, which in turn is strongly dependent on the capillary pressure and the water retention functions. At emplacement, there is a strong suction (high capillary pressure) within the partially saturated buffer and this suction becomes higher near the heater due to drying by evaporation. The flux also depends on the liquid flow mobility, including effects of intrinsic permeability and relative permeability for liquid flow.

The key parameters affecting the early time evolution of the moisture content are the water retention, absolute permeability and relative permeability, and the effective vapor diffusion coefficient for the partially saturated porous media. These parameters are usually determined from various laboratory experiments. The material parameters for the bentonite at the FE heater experiment have been determined by a number of experiments, both on granular bentonite samples and compacted bentonite blocks. Another key parameter is the saturation dependent thermal conductivity of the bentonite. The thermal conductivity impacts the temperature evolution and the thermal gradient and will therefore also impact the evolution of the moisture in the bentonite buffer.

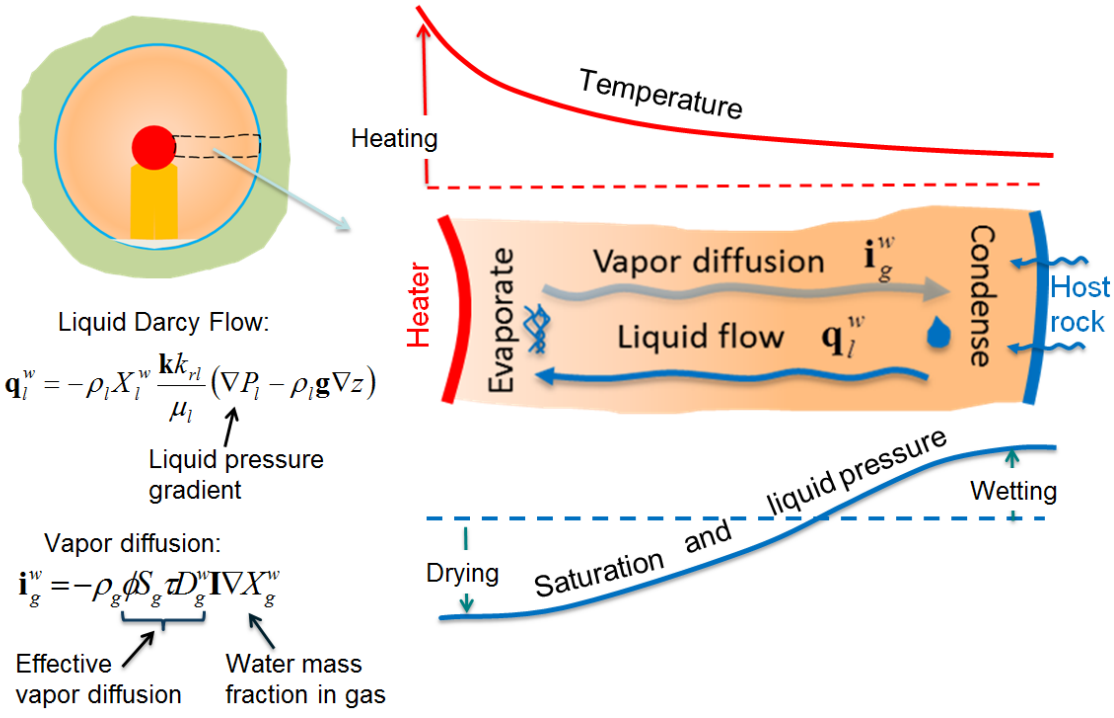

Figure 4-4. Conceptual model of the evolution of moisture in the heated bentonite buffer and equations for vapor diffusion in the gas phase and for liquid Darcy flow along the gradient of liquid pressure (capillary driven)

In the FY2016 milestone report (Zheng et al., 2016), the simulation results with comparison to the one year experimental data were presented. One of the main results reported was the fact that a tortuosity parameter as low as $\tau = 0.14$ was applied in order to obtain good match for the evolution of relative humidity in the buffer. In the FY2017 milestone report (Zheng et al., 2017), we found that this value of tortuosity ($\tau = 0.14$) still holds true for up to two years of heating and for a number of monitoring points at all three heaters.

In FY2018, we have expanded the analysis with comparison to about 3.5 years of field data with detailed comparison at all three heaters. The FY2018 updated numerical results were compared to measured data at monitoring points within the bentonite buffer, which are shown in Figures 4-5 to 4-10. The time zero in these figures are at 12/28/2014, which is just after the start of the heating at H1. The material parameters used in the modeling are almost the same as those in the FY2017 milestone report. For example, we still apply a tortuosity factor of 0.14 for the granular bentonite, but we have updated the tortuosity factor for the bentonite blocks, which is now 0.33.

Overall the results shown in Figures 4-5 to 4-10 confirm an excellent agreement in buffer temperature evolution and a good agreement in the evolution of relative humidity. An improvement in FY2018 was the match of the relative humidity evolution in the bentonite blocks below the heater (Figures 4-6b, 4-8b, and 4-10b). This was achieved by calibrating the tortuosity coefficient for the bentonite blocks, which is now set to 0.33 instead of 0.14. The simulated evolution of relative humidity near the tunnel wall is also

in good agreement with measurements, but some disagreement can be observed for the results at H3 (Figure 4-9b), where the measurements show a more rapid increase of relative humidity. However, the rate of wetting is very sensitive to how far from the rock wall the monitoring point is located. In the modeling, the tunnel is simulated as a perfect circle, while in the field the shape of the tunnel is not perfectly circular (Figure 4-11). Also in the modeling the shotcrete is modeled with a certain uniform thickness, which might be different from the heterogeneous shotcrete thickness in the field. Overall though, the rate of inflow from the rock and the relative humidity evolution is captured very well. In general, the rate of inflow to saturate the buffer is small due to the low permeability of the host rock.

Some minor discrepancies in the temperature evolution can be noted close to H1. The calculated temperature at H1 is generally smaller than the measured. In fact, the calculations show that the heater in the middle (H2) has about 2°C higher maximum temperature than at H1 and H3. In the field on the other hand, H1 has a slightly higher maximum temperature than H2 and H3. The higher temperature at H1 could be due to a heterogeneous buffer, in which the buffer density affects the local thermal conductivity. Another factor that can impact the temperature in the buffer close to the heater is the fact that the heater is not exactly centered at the tunnel axis, but shifted slightly to the right as shown in Figure 4-11.

In FY2018 we have also conducted scoping calculations related to thermal pressurization in the host rock as measured at several monitoring points near H2. The scoping calculations were conducted to understand the different pressure responses at monitoring points located in a direction perpendicular to bedding and parallel to bedding. Thermal pressurization occurs because of thermal expansion of pore fluid in a medium of low permeability. The thermal expansion coefficient of water is much higher than that of Opalinus Clay and therefore a temperature increase will cause the pore water pressure to increase. Important parameters for pressure responses during thermal pressurization are pore compressibility (which is related to bulk modulus and porosity) and permeability (Rutqvist et al., 2014).

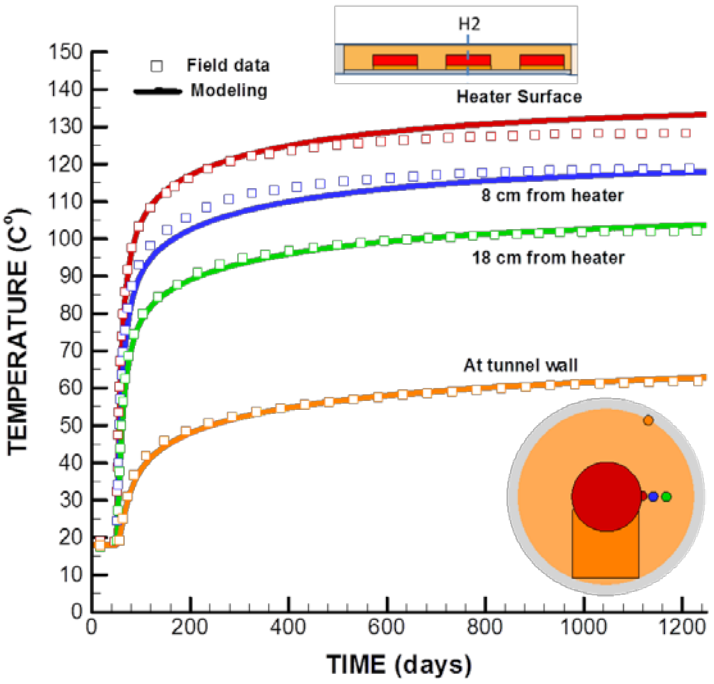

(a)

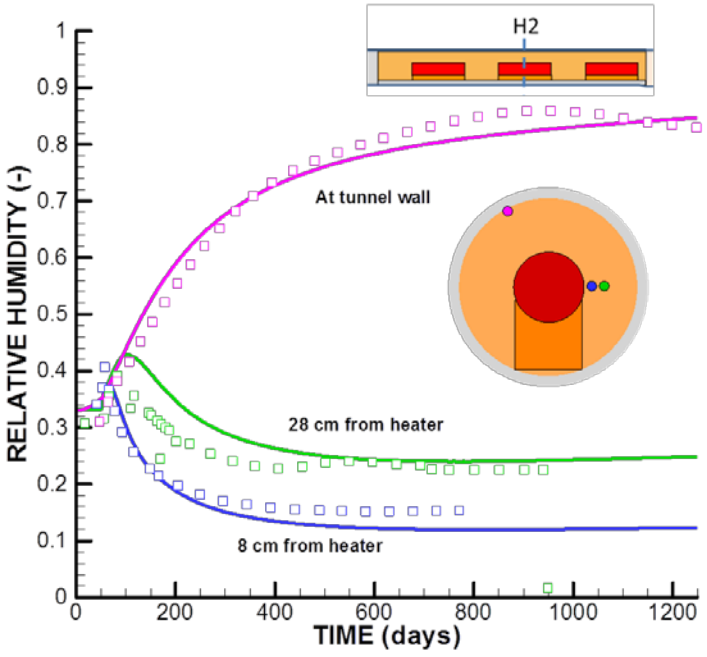

(b)

Figure 4-5. Comparison of modeled (lines) and measured (symbols) evolutions of (a) temperature and (b) relative humidity at monitoring point located in granular bentonite at H2 for over two years of monitoring data.

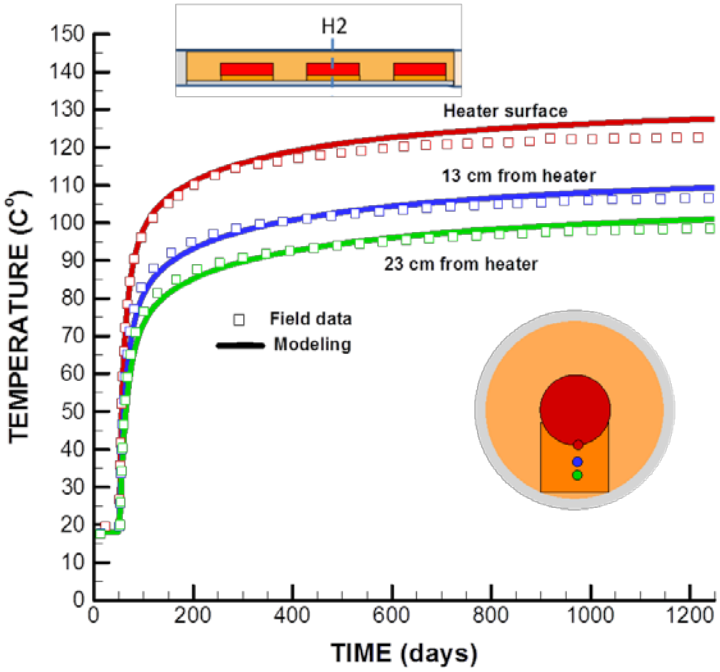

(a)

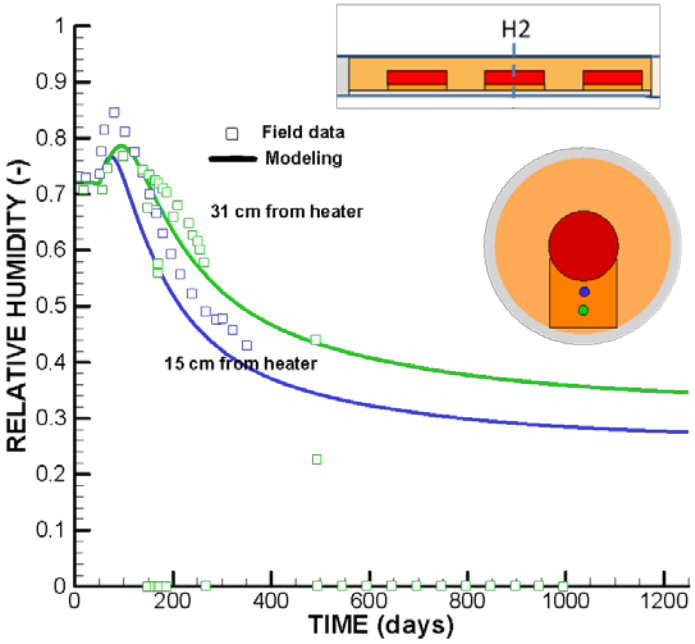

(b)

Figure 4-6. Comparison of modeled (lines) and measured (symbols) evolutions of (a) temperature and (b) relative humidity at monitoring point located in bentonite blocks at H2 for over two years of monitoring data.

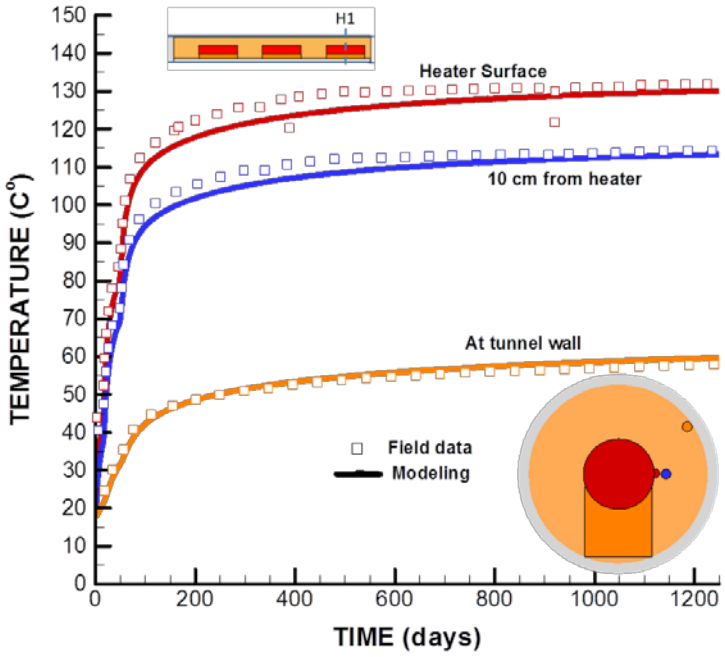

(a)

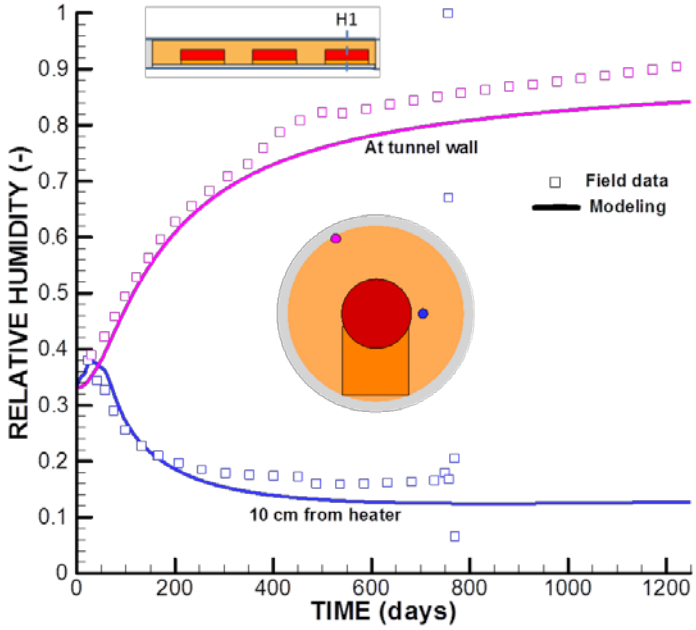

(b)

Figure 4-7. Comparison of modeled (lines) and measured (symbols) evolutions of (a) temperature and (b) relative humidity at monitoring point located in granular bentonite at H1 for over two years of monitoring data.

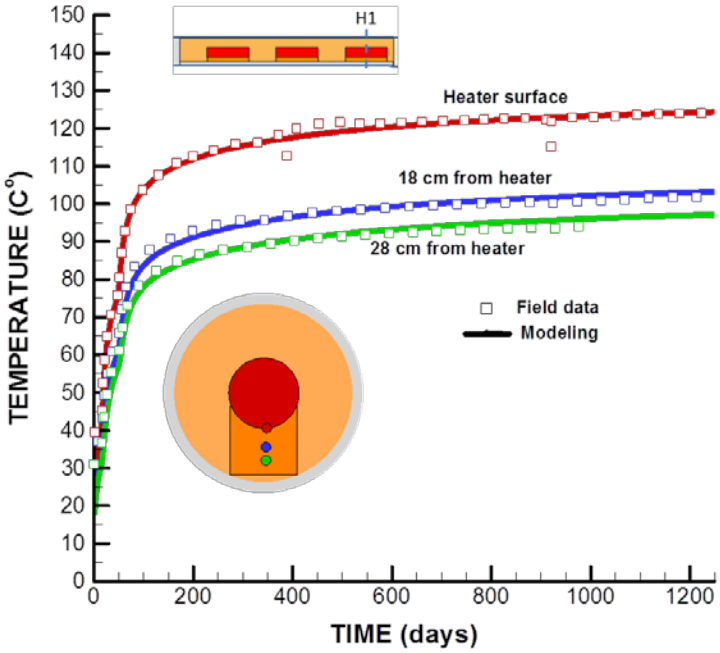

(a)

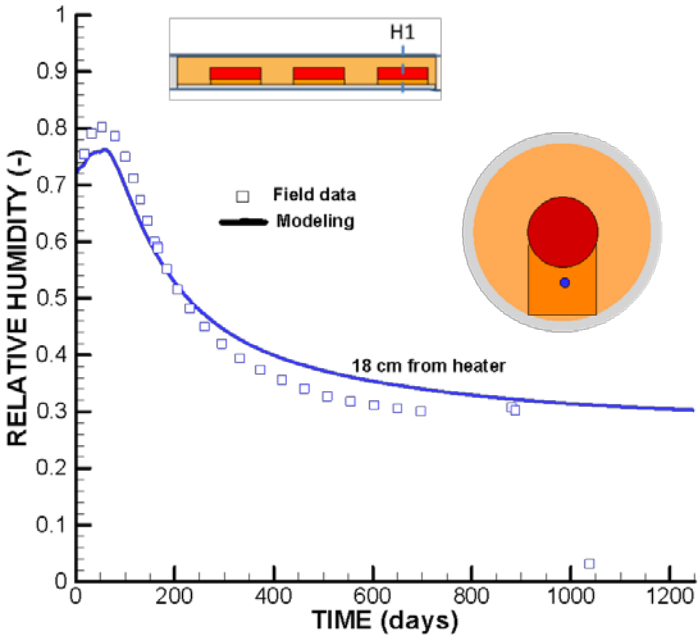

(b)

Figure 4-8. Comparison of modeled (lines) and measured (symbols) evolutions of (a) temperature and (b) relative humidity at monitoring point located in bentonite blocks at H1 for over two years of monitoring data.

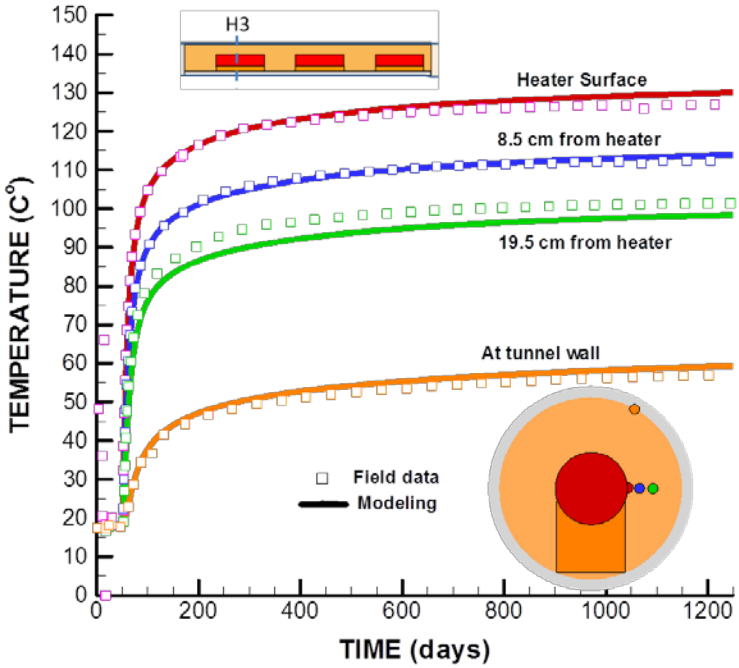

(a)

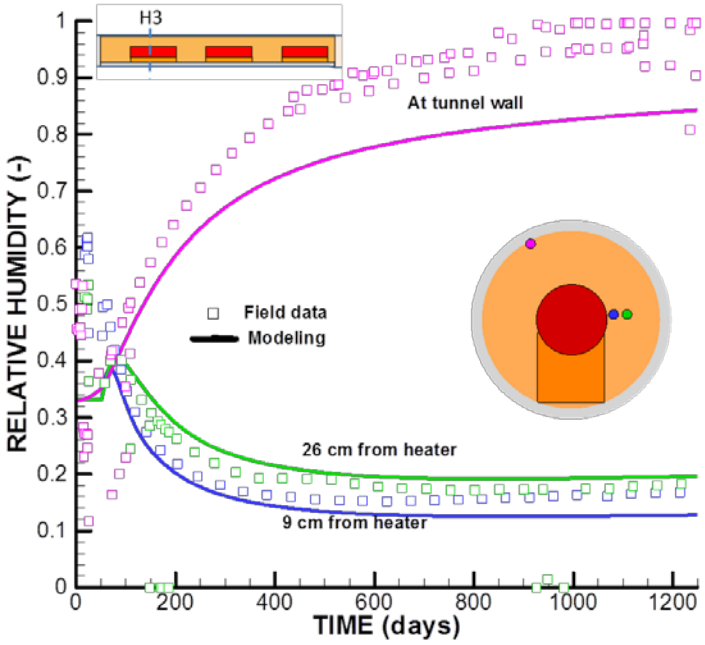

(b)

Figure 4-9. Comparison of modeled (lines) and measured (symbols) evolutions of (a) temperature and (b) relative humidity at monitoring point located in granular bentonite at H3 for over two years of monitoring data.

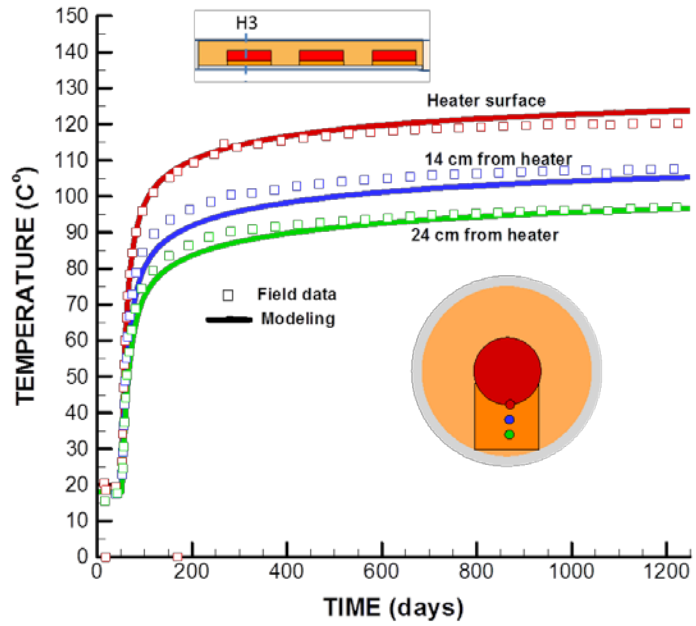

(a)

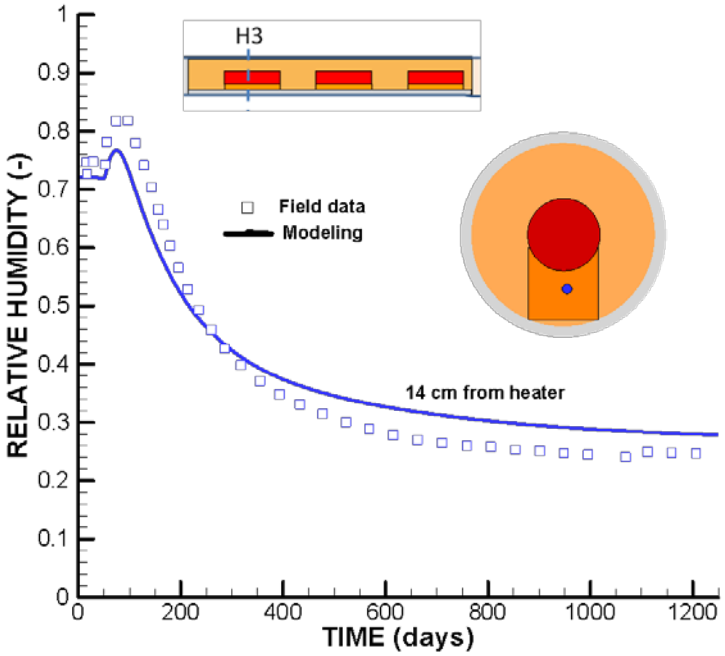

(b)

Figure 4-10. Comparison of modeled (lines) and measured (symbols) evolutions of (a) temperature and (b) relative humidity at monitoring point located in bentonite blocks at H1 for over two years of monitoring data.

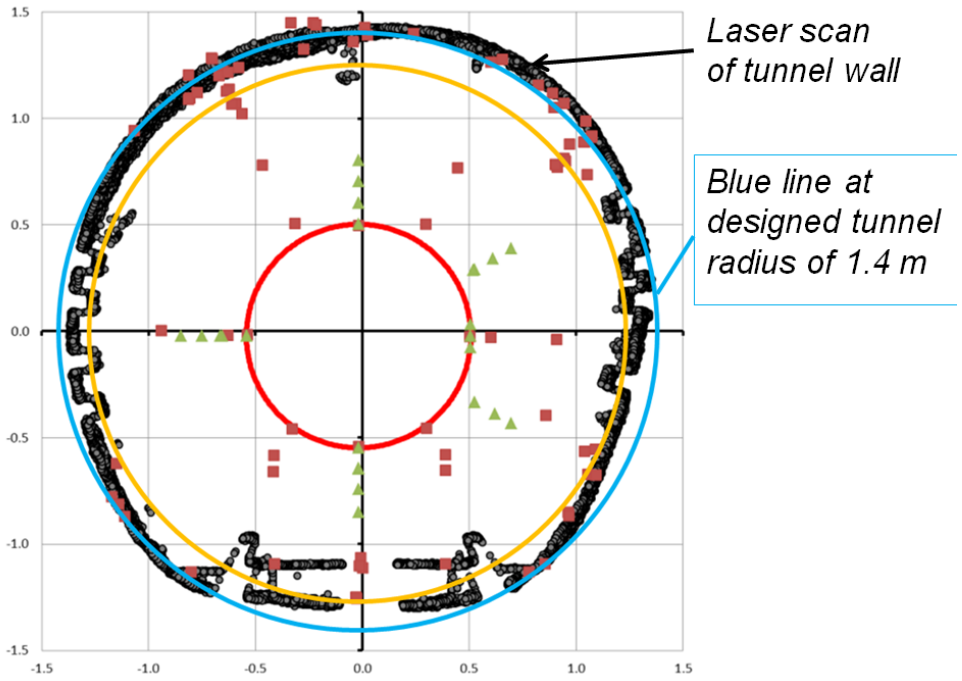

Figure 4-11. Comparison of the actual zigzag-shape cross-section of the tunnel from the laser scan with the circular shape of tunnel used in numerical modeling. The red circle in the middle is the heater. Squares and triangles indicate locations of some of monitoring sensors. Axis units are in meters.

In our base simulations for studying the evolution of temperature and relative humidly in the buffer we used the value of a permeability k = 5e-20 m^2, which is based on previous analysis of field experiments at Mont Terri. However, for better matching the thermal pressurization at the FE heater test we had to reduce the rock permeability to 1e-20 m^2 (for monitoring points located along a borehole perpendicular to bedding) and 2e-20 m^2 (for monitoring points located along a borehole parallel to bedding). Moreover, considering the average bulk modulus and porosity in Opalinus Clay at Mont Terri, the pore compressibility would be about 1e-9 Pa^{-1}. By setting permeability to 2e-20 m^2 and pore compressibility to 1e-9 Pa^{-1} we obtained a reasonably good match between simulated and monitoring pressure evolution for monitoring points located along a borehole parallel to bedding (Figure 4-12 a). For monitoring points located perpendicular to bedding, permeability was set to 2e-20 m^2 with a pore compressibility of 5e-9 Pa^{-1} (Figure 4-12b) This indicates that the difference between coupled THM responses are mainly due to a difference in fluid storage. In future modeling, we will study this in detail and will try to apply and explain these differences using anisotropic material models.

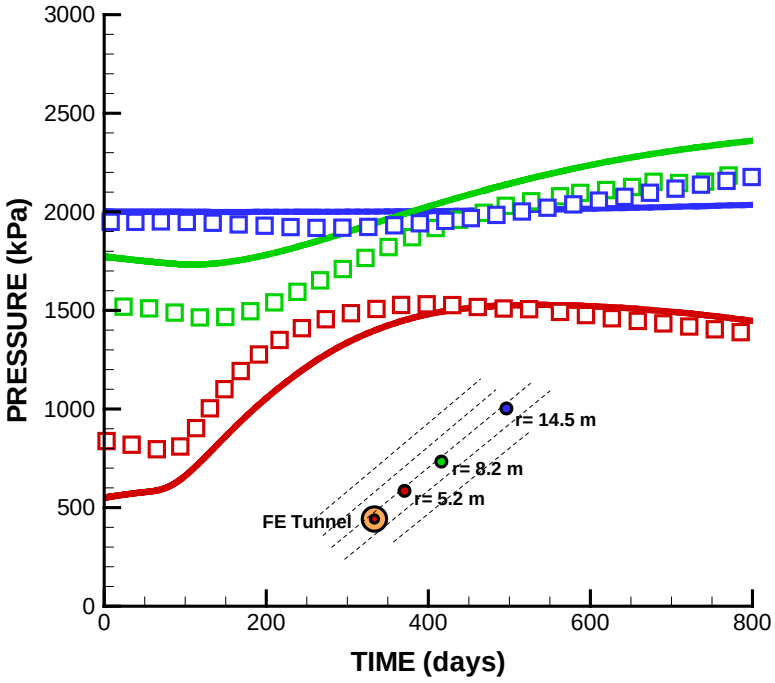

(a)

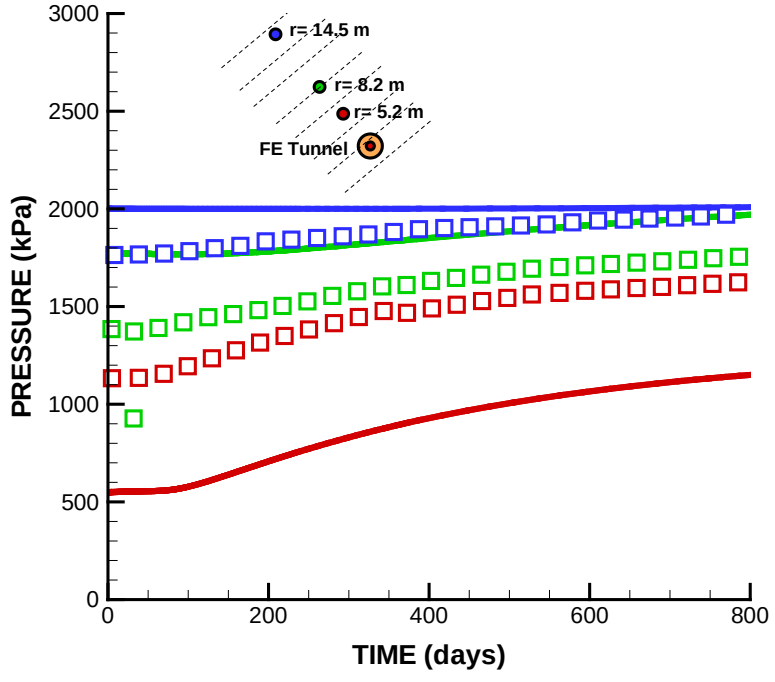

(b)

Figure 4-12. Results of scoping calculation for thermal pressurization effects in the host rock for pressure monitoring points located from the tunnel (a) perpendicular to bedding and (b) parallel to bedding.

4.5 Summary and Status the FE Experiment Modeling

As a modeling team in the Mont Terri FE experiment, we have conducted various types of modeling over the past few years, including benchmarking, heating design modeling, model predictions and interpretative modeling. Currently, we have interpreted data for up to 3.5 years of heating, including data on temperature and relatively humidity in the bentonite buffer and pressure in the host rock. Some finding and lessons learned are as follows:

- A good agreement between modeled and measured evolutions in buffer temperature and relative humidity was achieved at the FE experiment based on a model prediction using properties of bentonite and Opalinus Clay determined associated with the previous Mont Terri HE-E experiment.
- A value of the effective vapor diffusion coefficient (and medium tortuosity factor) could be precisely calibrated against measured relative humidity evolution in the granular bentonite, but the value was much lower than used for previous modeling of the HE-E experiment. This difference and the potential role of enhanced thermal diffusion of the early-time TH response in the buffer are open questions that warrant further studies.
- The values of the effective vapor diffusivity coefficient and the tortuosity factors for the bentonite block were determined based on the calibration of model parameters, and these values are much higher than for the granular bentonite.
- In a scoping calculation, thermal pressurization in the host rock could be reasonably well modeled, though local heterogeneities close to monitoring points probably affect the field data. Future modeling of thermal pressurization will focus at a mechanistic modeling of the anisotropic coupled THM responses and their impact on fluid pressure.

Still after 3.5 years of heating and water infiltration from the surrounding rock, no significant swelling stress has developed in the bentonite buffer. Measurements show the highest total pressure in the buffer is less than 0.5 MPa, but with a trend of accelerated stress increase in FY2019. We will continue modeling of the FE experiment along with new monitoring data, focusing more on the mechanical evolution of the buffer and host rock.

This page intentionally left blank.

5. HEATER EXPERIMENTS AT BURE IN COx CLAY STONE (DECOVALEX-2019)

In this section, we present recent TOUGH-FLAC modeling results related to the *in situ* heater experiment, conducted in Callovo-Oxfordian claystone (COx) at the Underground Research Laboratory (MHM URL) in Bure, France. The modeling of heater tests is one of the Tasks of the DECOVALEX-2019 project. In the following, we first provide a description of the DECOVALEX-2019 Task E and international modeling teams associated with this task; then provide a description of the *in situ* experiment and updated TOUGH-FLAC simulation results with comparison to experimental data.

5.1 DECOVALEX-2019 Task E and International Modeling Teams

DECOVALEX-2019 Task E is a study addressing important issues related to the repository design and safety calculation: how to go from a sample scale to a repository scale? Thermally induced pore pressure build-up and stress changes around a repository are important issues studied in this task, which is coordinated by ANDRA (French National Radioactive Waste Management Agency), and involves modeling of two *in situ* tests performed at the URL in Bure (France):

- The TED experiment, a small-scale heating experiment focused on the claystone THM behavior of the undisturbed rock mass in the far field; and
- The ALC experiment, a one-to-one scale heating experiment especially focused on the interaction between the surrounding rock and the support (steel casing in this case) in the near field.

Following the modeling of the two *in situ* tests, the impact of the behavior at the repository scale (considering several parallel cells) will be modeled. This application should address some key technical challenges, such as the variability of the THM parameters and the determination of appropriate boundary conditions when modeling is used to represent a series of parallel cells.

DECOVALEX-2019 Task E is conducted by a step-by-step approach, from small-scale to full-scale studies (Figure 5-1). It is structured into four main steps:

- Step 1: Simple 3D THM modeling benchmark;
- Step 2: Interpretative modeling of the TED experiment (back analysis);
- Step 3: Modeling of the ALC experiment
    - Step 3a: Predictive modeling of the ALC experiment using the reference values for the rock mass parameters determined in Step 2;
    - Step 3b: Interpretative modeling of the ALC experiment;
- Step 4: Prediction at the repository scale of an area with several high level waste cells.

The participating groups in the DECOVALEX-2019, Task E are:

- Canada: NWMO
- France: ANDRA, University of Lille
- Germany: BGR (UFZ Leipzig)
- UK: RWM (Quintessa Ltd)
- USA: DOE, LBNL

Currently, Step 1 related to 3D THM modeling benchmark, has been completed, Step 2 related to interpretative modeling of the TED experiment at Bure has been completed, and Step 3 related to blind prediction and interpretative modeling of the ALC experiment is ongoing. The prediction at the repository scale for Step 4 should be started before the next DECOVALEX-2019 workshop, which will be held in October 2018.

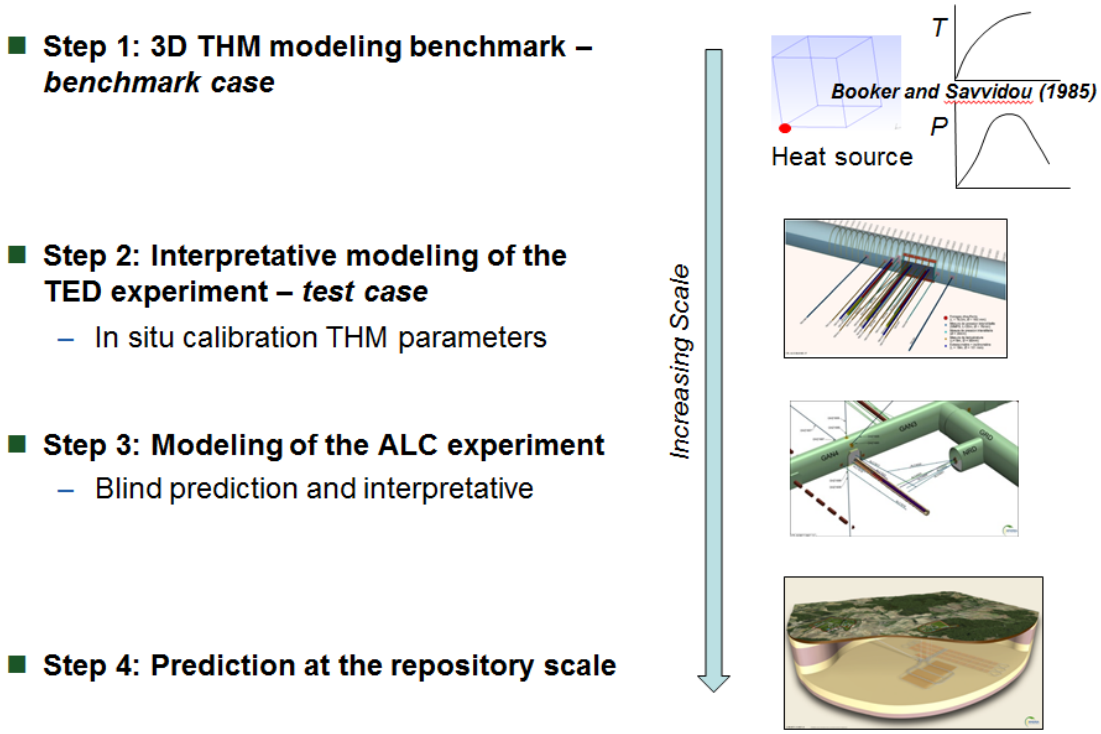

Figure 5-1. Overview of DECOVALEX-2019 Task E with steps of increasing scale.

5.2 TOUGH-FLAC Simulation Results with Comparison to Experimental Data

5.2.1 Step 1: 3D THM modeling benchmark

Step 1 of Task E is a basic benchmark test considering the consolidation of an infinite homogeneous saturated porous medium around a constant point heat input. Booker and Savvidou (1985) provided the analytical solution for this problem based on the hypothesis that the pore water and the solid grains are incompressible. The 3D model is a cube of 15m×15m×15m, which is generated with FLAC3D, shown in Figure 5-2. Considering the symmetric planes, only one eighth of the model is simulated. Due to the limitation of the temperature in the module EOS1 (equation of state) in TOUGH2, we need to assign a larger size for the heat source with high thermal conductivity to lower the temperature inside heat source. Therefore, the heat source is represented by a 1/8 cylinder with 2.5 cm radius centered at the origin point and is refined with smaller meshes. The initial temperature, pore pressure and stresses are set to 0°C and 0 Pa. Regarding thermal and hydraulic conditions and considering symmetric conditions, the three symmetry planes are impermeable and adiabatic. At far field, the temperature and pore pressure are set to 0°C and 0 Pa. At the heat source, the constant heat power of Q=700 W is instantaneously applied at time t=0. Regarding mechanical conditions, all domain boundaries are free except the symmetry planes, where null displacement conditions are applied normal to the boundaries.

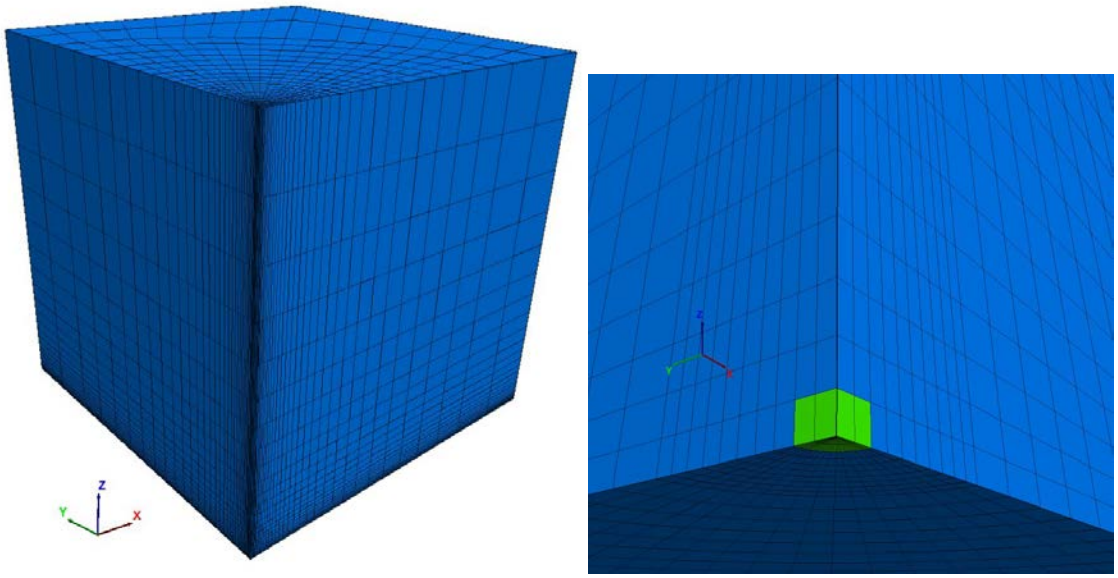

a) b)

Figure 5-2. a) Geometry of the simulation domain, and b) Heater source (green elements) is a 1/8 cylinder with 2.5cm radius.

A homogenous and isotropic material is considered. The model parameters are listed in Table 5-1. The table includes the THM parameters of the two components, solid phase and pore water.

Table 5-1. Model parameters of Step 1.

Parameters	Values
Porosity	$\phi = 0.15$
Equivalent thermal conductivity [W/m/K]	$\lambda = 1.7$
Equivalent density [kg/m^3]	$\rho = 2400$
Equivalent heat capacity [J/kg/K]	$C_p = 1000$
Permeability [m^2]	$k = 4.5 \times 10^{-20}$
Young modulus [MPa]	$E = 4500$
Poisson's ratio	$\nu = 0.3$
Density of solid grains [kg/m^3]	$\rho_s = 2700$
Heat capacity of solid grains [J/kg/K]	$C_{ps} = 773$
Volumetric coefficient of thermal expansion of solid grains [1/K]	$\alpha_s = 4.2 \times 10^{-5}$
Density of water [kg/m^3]	$\rho_w = 1000$
Compressibility of water [1/Pa]	$c_w = 0^*$
Heat capacity of water [J/kg/K]	$C_{pw} = 4180$
Dynamic viscosity of water [Pa×s]	$\mu_w = 1 \times 10^{-3}$
Volumetric coefficient of thermal expansion of water [1/K]	$\alpha_w = 4 \times 10^{-4}$

*Note: the analytical solution in (Booker and Savvidou, 1985) assumes the water is incompressible, indicating $c_w = 0$.

Comparison between modeling results and analytical solution for, temperature, pressure, displacements (u_x, u_y, u_z), and stresses evolution up to 365 days is provided at the points given in Table 5-2.

Table 5-2. Points used for comparison of numerical results and analytical solution in for Step 1.

Points	(x, y, z) coordinates	Quantity
P1	(0.35, 0, 0)	Temperature, pressure
P2	(0.5, 0, 0)	Temperature, pressure
P3	(1.5, 0, 0)	Temperature, pressure
P4	(0.35, 0.5, 0.6)	Temperature, pressure, displacements, stresses

In FY2017, we have computed the evolution of temperature, pressure, and displacements at point P1, P2, P3 and P4 as listed in Table 5-2. Comparison between numerical results with analytical solution is shown in Figures 5-3 to 5-5. An overall good agreement is obtained related to the temperature, pore pressure and displacement evolution between numerical simulations and analytical solutions, except the displacement in *x*-direction at P4 is 0.02 mm smaller than analytical solution. The reason for that could be that the position of P4 is slightly inaccurate when interpolation is used in the numerical method.

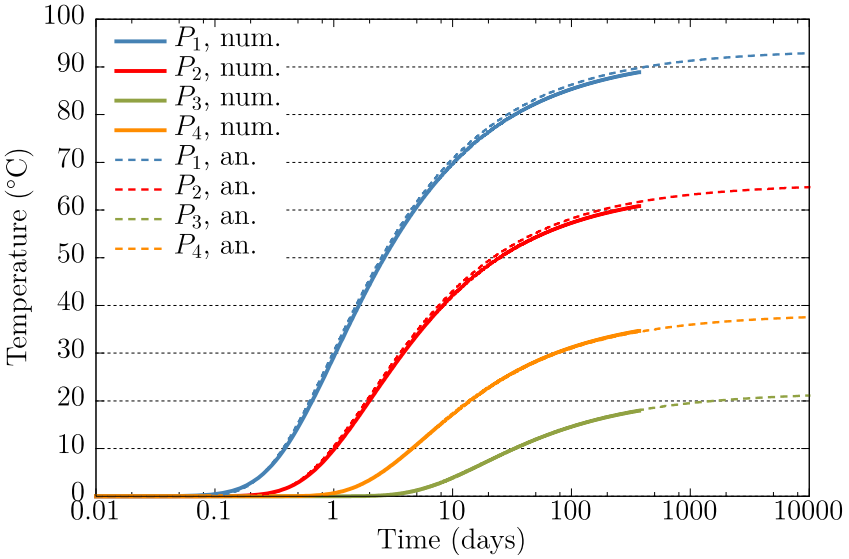

Figure 5-3. Simulation results of temperature at different points.

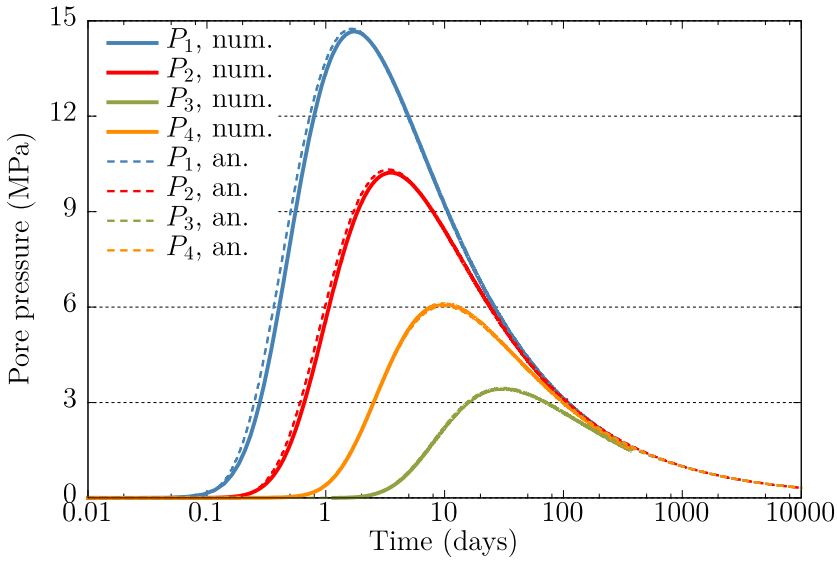

Figure 5-4. Simulation results of pore pressure at different points.

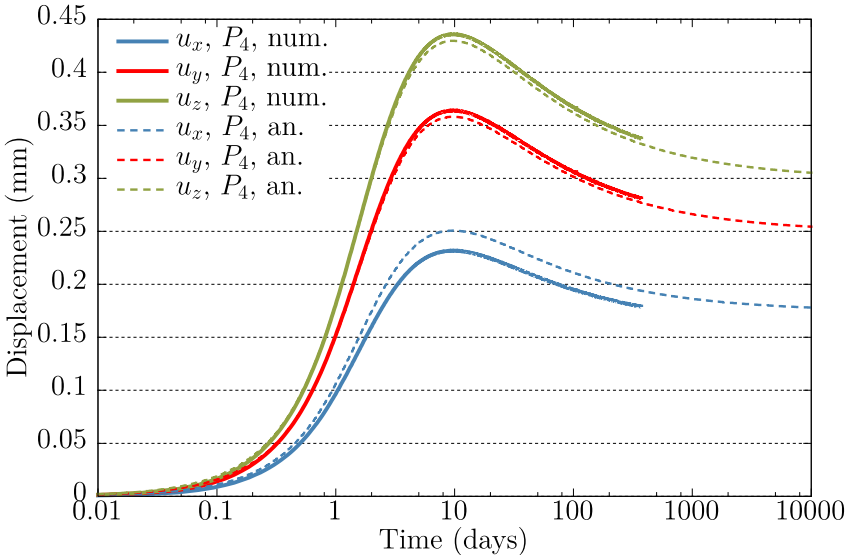

Figure 5-5. Simulation results of displacements at point P4.

Because the analytical solution of stresses in Booker and Savvidou (1985) is not correct, the stress results were not displayed in our FY2017 milestone report (Zheng et al., 2017). In FY2018, the analytical solution for stresses has been derived based on the methodology in Booker and Savvidou's paper. The simulated stress results are as presented in Figures 5-6a and b, are now in a good agreement with the analytical solution, which verifies the correctness of the TOUGH-FLAC code as well as the results of modeling of temperature, pore pressure and displacements.

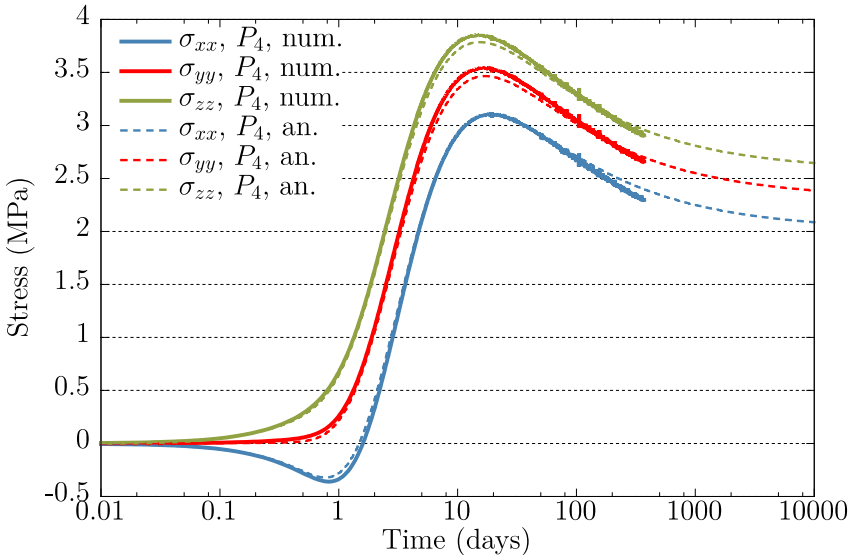

a)

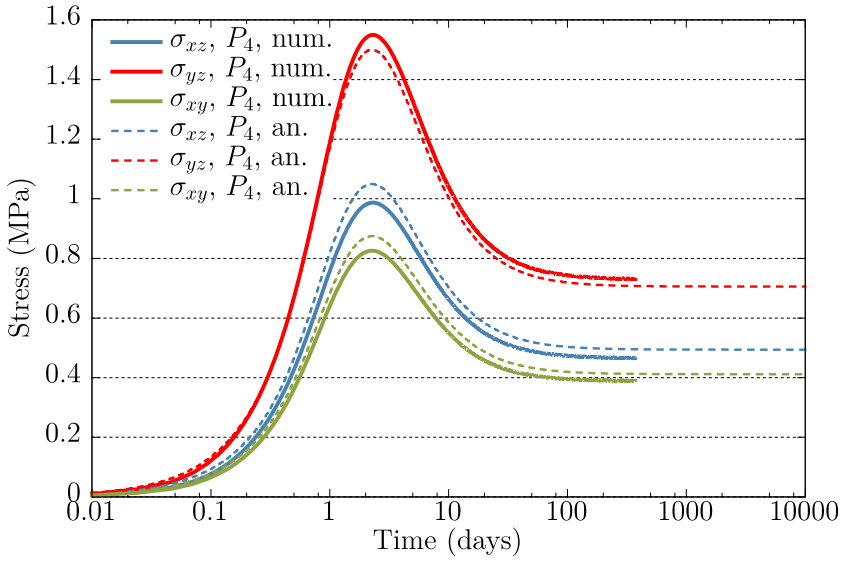

b)

Figure 5-6. Simulation results of stresses at point P4: a) Normal stresses, b) Shear stresses.

5.2.2 Step 2: TED experiment

The TED experiment lasted three years from 2010 to 2013. It involved three heaters at a depth of 490 m, in three parallel boreholes at a separation of about 2.7 m (Figure 5-7). The three heaters were 4 m long and were installed at the end of 160 mm diameter and 16 m long boreholes, drilled from a main drift and parallel to the maximum horizontal stress. This arrangement represented a similar configuration to high-level nuclear waste cells with parallel microtunnels, but at a smaller scale. The TED experiment was heavily instrumented with 108 temperature sensors in the rock mass, 69 temperature sensors in the 3 heater boreholes, 18 piezometers, 2 extensometers and inclinometers, and 10 temperature sensors

recording the temperature at the level of the main drift. The temperature measurements made during the TED experiment showed that the rock has an anisotropic thermal conductivity, because at the same distance from the heater, the temperature increase is higher in the bedding plane than that in the perpendicular direction. Observations of pore pressure also showed that its evolution depended on the location with respect to the bedding plane; following a power law increase, the pore pressure increased faster in the direction parallel to bedding than that in perpendicular direction.

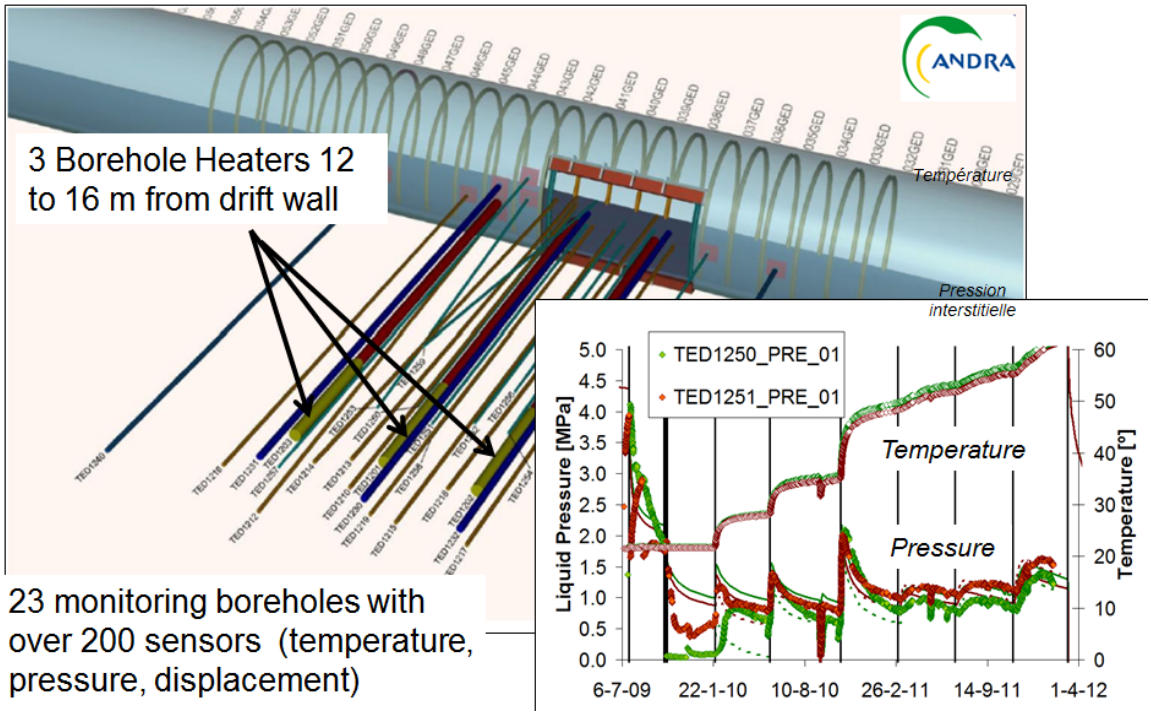

Figure 5-7. The schematic of the TED experiment at Bure. The insert on the figure is the graphs of pressure and temperature evolution, which were used by modeling teams in DECOVALEX-2019 Task E for interpretative modeling.

The purpose of Step 2 is to model the THM response of COx claystone in the TED experiment and to calibrate the numerical models against experimental data. This modeling of the TED experiment will also help improve understanding of physical phenomena observed.

The domain geometry simulated is a cube with a side length of 50 m centered in the height z = 0, i.e., almost exactly at the GED drift center at the depth of 490 m. The model represents only a half of the GED drift (Figure 5-8). Three heaters are embedded at the center of the domain with surrounded refined grids. For the modeling purposes, it is assumed that the whole domain is saturated and remains saturated during the experiment. The boundary conditions are summarized in Table 5-3.

In the previous FY2017 milestone report, the drilling of heater boreholes and extensometer boreholes were not explicitly modeled, indicating no water flow from the rock matrix into these boreholes. As a result, the pore pressure at the sensor in TED 1253, which is close to draining boreholes, was predicted much higher than experimental observation. Besides that, we did not account for the excavation of GED tunnel and drilling of the boreholes. Therefore, the effects induced by excavation ware not studied, and the pore pressure prior to the heating phase was assumed distributed uniformly in the host rock. The variability of permeability in the EDZ was not considered.

In FY2018, the updated model started with instant excavation of the GED tunnel, followed by drilling of other boreholes. Then at 506 days after excavation, the heating phase started and was running for about 1251 days. The time zero corresponds to the excavation of GED tunnel at 04/21/2008. Heater 1 was turned on first, and it took three steps to reach the planned heat power (600W). After Heater 1 had been turned on for 400 days, Heaters 2 and 3 were turned on to heat the domain, including three heat power steps. The recent model computed with the raw data of heat power is shown in Figure 5-9. As suggested by other modeling teams among the DECOVALEX participants, a cylindrical EDZ was applied around GED tunnel with 1m thickness in order to include the variability of permeability due to excavation (Figure 5-8a). The pore water pressure is considered uniform at 4.7 MPa in the entire domain when excavation started. The stress values follow the anisotropic state of stress. For calculations, the stresses proposed by the task lead from ANDRA are: the major horizontal stress σ_H =16.1 MPa, and the horizontal minor stress σ_h = 12.4 MPa, and the lithostatic stress σ_v =12.7 MPa.

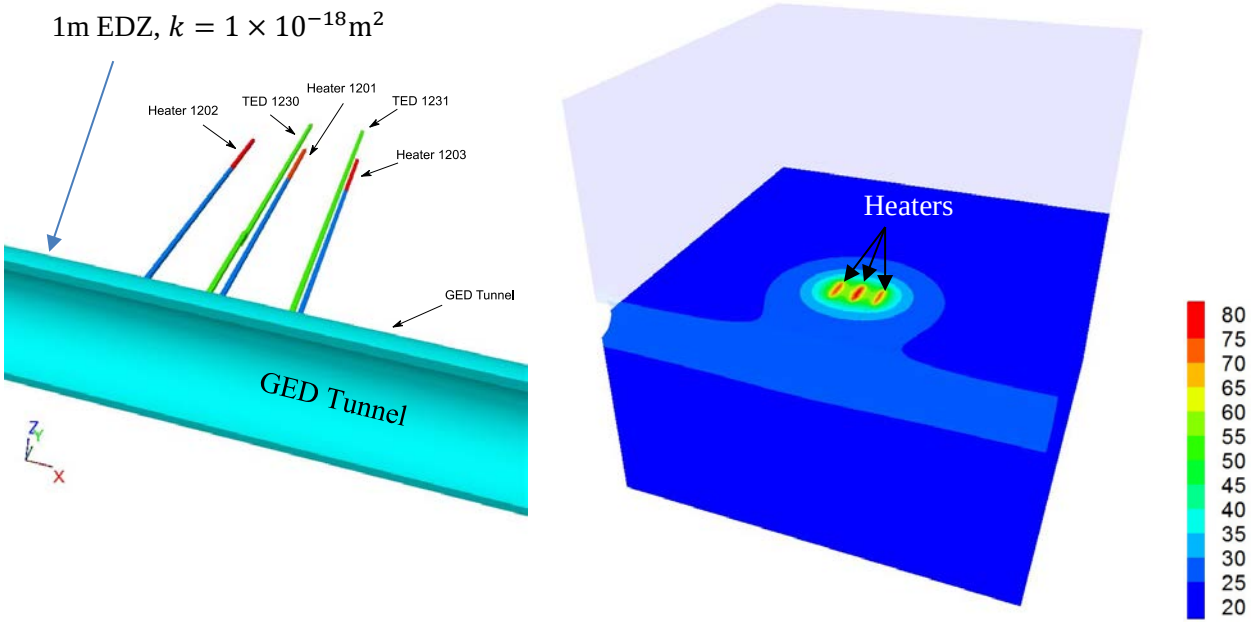

a) b)

Figure 5-8. a) The model setup the position of heater boreholes (Heater 1201~1203), extensometer boreholes (TED 1230 and TED 1231), and GED tunnel surrounded by 1m EDZ and b) Temperature distribution at 1509 days.

Table 5-3. THM boundary conditions of TED experiment modeling for Step 2.

Boundary	Thermal condition	Hydraulic condition	Mechanical condition
External faces (except top and bottom)	No heat flux	No water flux	No normal displacements
Top surface	*In situ* temperature T = 21°C	4.7 MPa	Vertical geostatic stress $\sigma_v = 12.7$ MPa
Bottom	*In situ* temperature T = 23°C	4.7 MPa	No normal displacements
GED drift wall	Temperature measurements in the GED drift	Draining condition: atmospheric pressure	No normal displacements
TED1230 and TED1231 Boreholes (extensometers)*	No heat flux	Draining condition: atmospheric pressure	No normal displacements
Heater Boreholes	History of applied power (Figure 5-9)	Draining condition: atmospheric pressure	

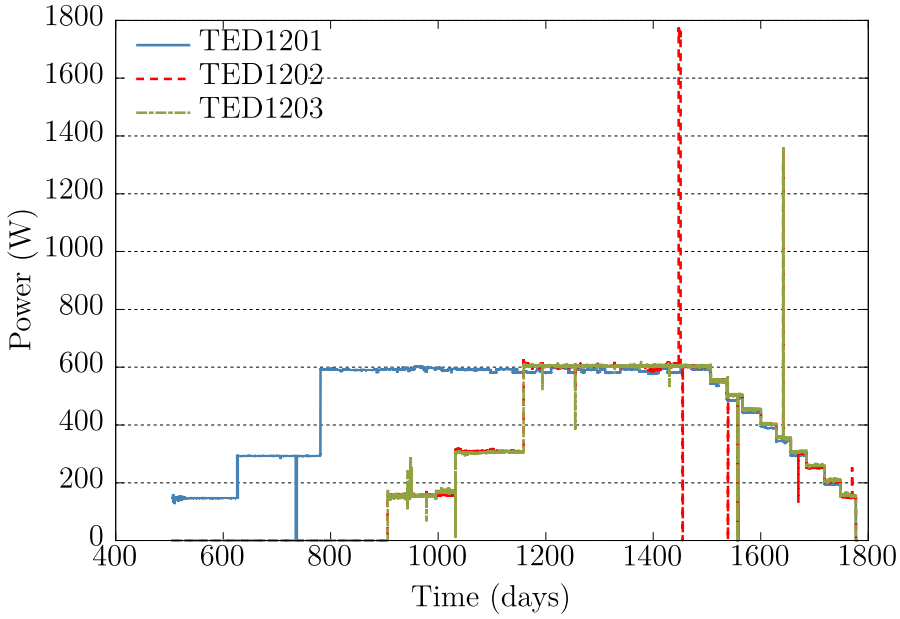

Figure 5-9. Heat power used for Heater 1, 2 and 3.

The THM computation with the simulator TOUGH-FLAC included water properties calculated from the steam table equations (IFC-1967). We have recalibrated thermal conductivity, mechanical properties and permeability of COx rock, because we applied other conditions, such as the drainage boundary. All parameters utilized in the current model are summarized in Table 5-4.

.

Table 5-4. THM parameters of Step 2 used for THM simulations.

Parameters	Values
Porosity	$\phi = 0.15$
Equivalent thermal conductivity parallel to bedding [W/m/K]	$\lambda = 2.05$
Equivalent thermal conductivity perpendicular to bedding [W/m/K]	$\lambda = 1.15$
Equivalent density [kg/m^3]	$\rho = 2400$
Density of solid grains [kg/m^3]	$\rho_s = 2600$
Heat capacity of solid grains [J/kg/K]	$C_{ps} = 800$
Permeability parallel to bedding [m^2]	$K_{\parallel} = 3 \times 10^{-20}$
Permeability perpendicular to bedding [m^2]	$K_{\perp} = 0.7 \times 10^{-20}$
Biot coefficient	$b = 0.7$
Volumetric coefficient of thermal expansion of solid grains [1/K]	$\alpha_s = 4.2 \times 10^{-5}$
Young's modulus parallel to bedding [GPa]	$E_1 = E_{\parallel} = 6$
Young's modulus perpendicular to bedding [GPa]	$E_3 = E_{\perp} = 3$
Poisson's ratio inside the bedding plane [-]	$\nu_{12} = 0.3$
Poisson's ratio between in bedding plane and out-of-plane [-]	$\nu_{13} = 0.3$
Water properties (ρ_w, c_w, C_{pw}, μ_w, α_w)	(IFC-1967)

In TED experiment, 6 sensors were placed at different boreholes near heaters to measure the temperature evolution during the heating stage. The collected data were used as a basis for calibration of thermal properties. Figure 5-10 displays the recent temperature results based on the results of simulations with calibrated parameters. As the figure shows, a good agreement at Boreholes 1210, 1219, 1250, and 1251 is achieved between the model prediction and the experimental data. Note that although the model simulation overestimated the temperature by about 3 to 5^o at the two points farthest from the heater, Boreholes 1253 and 1258, the experiment team reported that these two sensors as unreliable. So the calibration on the thermal properties based on other locations is acceptable.

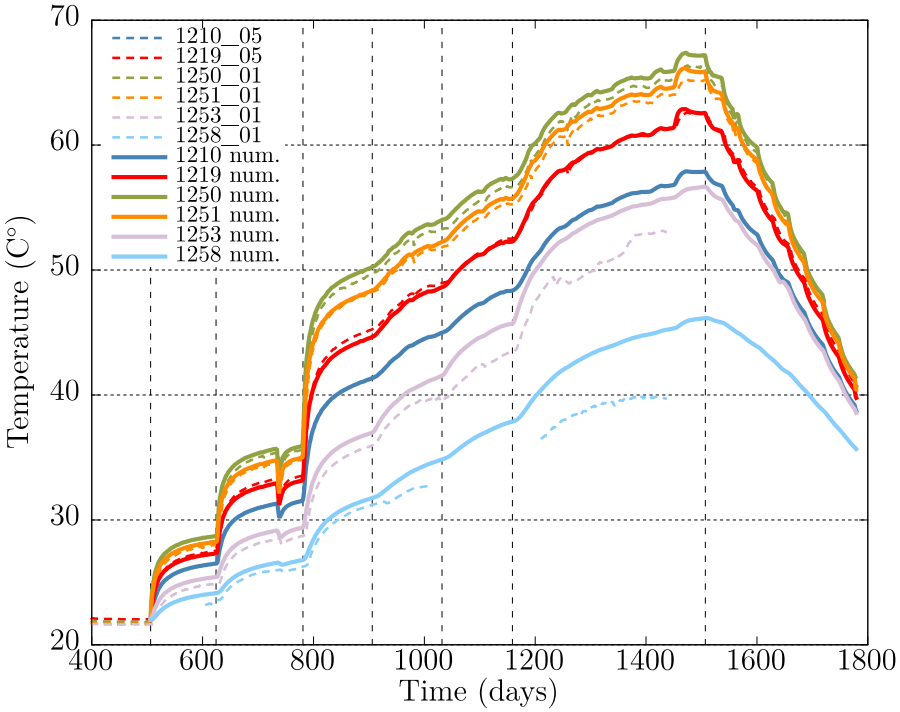

Figure 5-10. Temperature evolution simulated with calibrated thermal conductivities at measuring points.

Figure 5-11a presents the simulation results and experimental observations of pore pressure at the sensor positions in Boreholes 1253 and 1258. From the figure, the simulated pore pressure at Borehole 1253 is in good agreement with experimental data recorded by the sensor. Although some disagreements of pore pressure at Borehole 1258 are noted, especially the pore pressure at the beginning of the heating phase, but after 800 days the predicted pore pressure agrees with experimental data. The explanation is that the simulation results of pore pressure depends on the final status of the excavation phase, while the observed data were affected by the heterogeneity of rock matrix and pore pressure build-up after sensor installation. Figure 5-11b displays the simulated and observed pore pressure at five sensor positions in Borehole 1240. Compared with experimental data, the trend of pore pressure change has been captured while the magnitude of pore pressure at peak is underestimated.

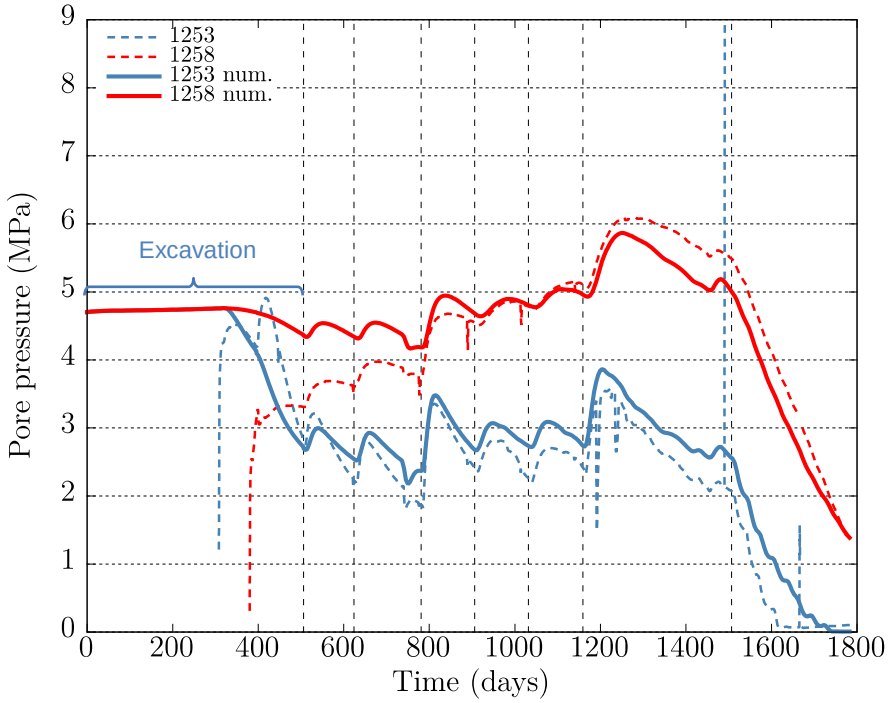

a)

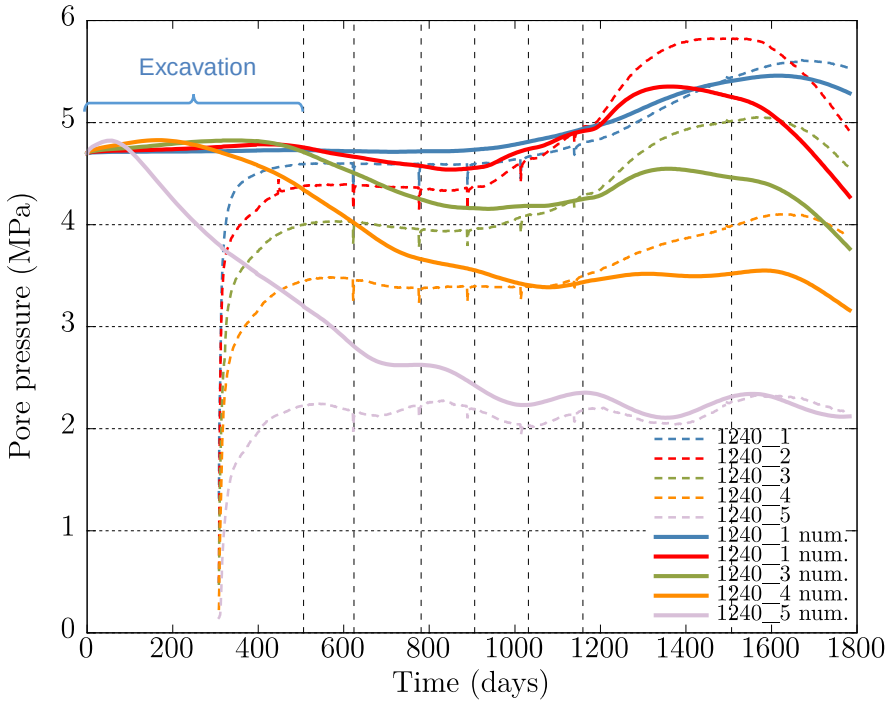

b)

Figure 5-11. a) Pore pressure evolution at Boreholes 1253 and 1258. b) Pore pressure evolution at Boreholes 1240.

In FY2018, more conditions are applied in the model, such as the tunnel excavation, boreholes, EDZ around the tunnel and the drainage boundary at boreholes. The new model simulated with re-calibrated parameters provides a better prediction of temperature and pore pressure compared to last year's results. However, no measured data on stresses are available.

5.2.3 Step 3 – ALC experiment

The ALC experiment started its heating phase in 2013 and is an ongoing *in situ* heating test performed in the MHM URL. The experiment is a full scale representation of a single high-level waste cell in Cox claystone. The ALC1604 microtunnel was drilled from the GAN drift. It has a total length of 25 m and it includes different parts. The heated part in ALC experiment is located in the body part of ALC1604 between 10 and 25 m deep (Figure 5-12) and is made up of five heating elements. Each element is 3 meters long and has a diameter of 508 mm. The ALC experiment was heavily instrumented with temperature and relative humidity sensors, piezometers, strain gauges, and displacement sensors. The temperature measurements made during the ALC experiment showed a similar phenomenon as in the TED experiment, indicating an anisotropic thermal conductivity; because at the same distance from the heater, the temperature increase is higher in the bedding plane than that in the perpendicular direction. Observations of pore pressure showed that its evolution depended on the location with respect to the bedding, and strong hydro-mechanical (HM) coupling induces opposite pore pressure change near ALC1604 after its excavation. In the vertical direction, the volumetric strain is positive (volumetric expansion), indicating the pore pressure decrease, because in the horizontal direction, the volumetric strain is negative (the volume decreases), driving pore pressure increase.

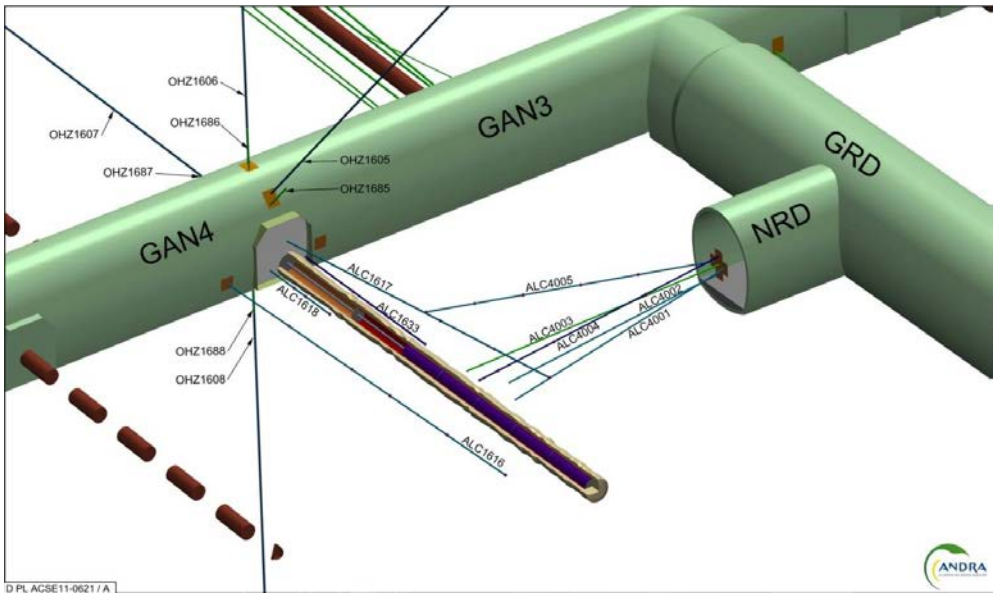

Figure 5-12. The ALC experiment at Bure with various monitor boreholes and microtunnel ALC1604 that are used by modeling teams in DEOVALEX-2019, Task E, for interpretative modeling.

The purpose of Step 3 is to predict the THM response of COx claystone in the ALC experiment with calibrated material parameters from TED experiment. Modeling of ALC experiment will help investigate the behavior of the cell and the casing under thermal loading, and to understand the THM behavior of the COx and of the interface between the rock mass and the casing.

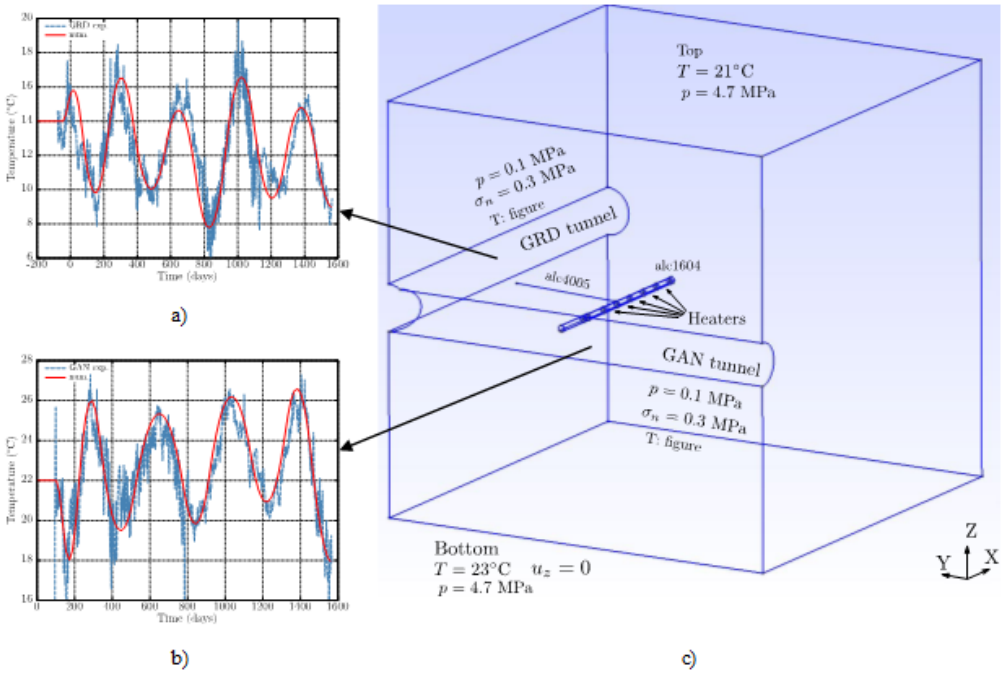

Figure 5-13. Geometry of the model with boundary conditions: a) Observed and simulated temperature evolution at GRD tunnel; b) Observed and simulated temperature evolution at GAN tunnel; and c) Geometry of the simulation domain and boundary conditions on each surface.

The geometry model domain is a cube with a side length of 50 m centered in height at z = 0, with half of the GAN tunnel excavated along the *y*-direction, and half of the GRD tunnel excavated along the *x*-direction (Figure 5-13c). Five heating elements are located in ALC1604 between 10 and 25 m along *x*-direction. The heaters are discretized with refined elements. Casing and gap inside the borehole are both explicitly discretized (Figure 5-14). For modeling purposes, it is assumed that the whole domain is saturated and remains saturated during the experiment. An additional draining borehole, ALC4005, is explicitly simulated with excavation and drainage as Figure 5-13 shows.

In the simulation, the model started with instant excavation of GAN and GRD tunnels, followed by drilling of other boreholes. Then at 458 days after the excavation, the heating phase started and was running for about 1500 days. The time zero, corresponds to the excavation of tunnels, is at 11/01/2011. A heating test at a very low power (33 W/m, 495 W in total) was conducted between January 31 and February 15, 2013. The main heating phase started on April 18, 2013, at a constant nominal power of 220 W/m (3300 W in total) for the 15 m occupied by the heater elements (i.e., 660W per element). The initial pore water pressure is considered uniform at 4.7 MPa in the entire domain when excavation started. The stress values follow the anisotropic state of stress. For the calculation the stresses are proposed as: the major horizontal stress σ_H is set to 16.1 MPa in *y*-direction, and the horizontal minor stress σ_h and the lithostatic stress σ_v are set respectively to 12.4 MPa in *x*-direction and 12.7 MPa.

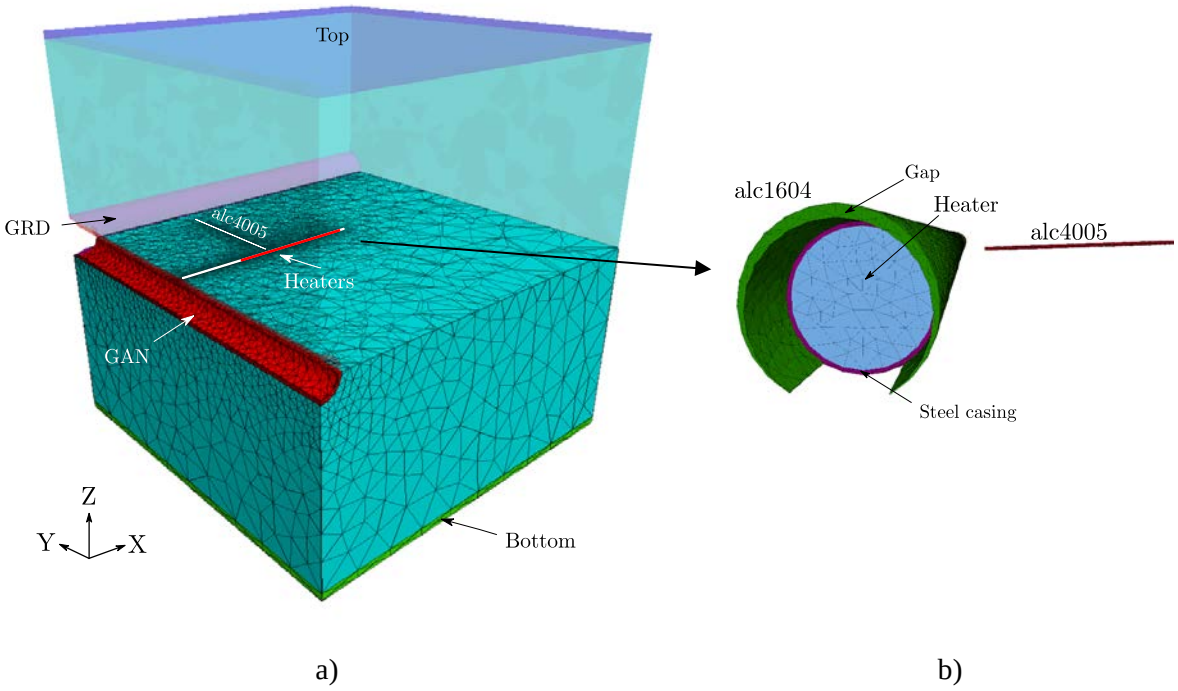

Figure 5-14. Mesh generation in simulated domain. a) Mesh in the entire domain. b) Mesh generation for heater, casing and the gap between them.

The THM computation of ALC experiment is conducted with the parameters, calibrated from TED test, which are listed in Table 5-4.

In the field, six sensors were placed at different boreholes near heaters to measure the temperature evolution during the heating stage. These collected data are used as a basis for calibration of thermal properties. Figure 5-15 displays the temperature results compared with experimental data recorded by the sensors. As the figure shows, a good agreement is achieved between the model prediction and the experimental data. However, at sensors 1617-1 and 1617-2, our model predicted higher temperature than observed data, while at sensors 1616-5 and 4005-4, the model underestimated the temperature. A possible explanation is that the simulation is based on an assumption of homogeneous host rock, while the *in situ* COx clay stone is heterogeneous.

Figure 5-16 presents simulation results of pore pressure at the sensor positions in the boreholes. From the figure, it is found that the pore pressure decreases after the initial excavation of the GAN and GRD tunnels, which is due to the drainage conditions applied on tunnel surfaces. Then, around 0 day, corresponding to the day of 10/23/2011, the drilling of the microtunnel (ALC1604) is computed, and the results indicate the relevant hydro-mechanical (HM) coupling. Volumetric expansion due to excavation of ALC1604 occur at sensors 1617-1 and 1617-2, which are above ALC1604. As a result, pore pressure at these two positions decreases. In the horizontal direction, volumetric compression occurs at sensors 1616-2 and 1616-5, which raises the pore pressure. After the heating started, the pore pressure increased due to thermal pressurization except at sensor 1616-5, which was close to the GAN tunnel, and affected by the temperature boundary on the surface of the tunnel. Sensor 4005-4 shows similar response. Since it is far from the heaters, the temperature changes are small and the peak of pore pressure is lower than at other sensors.

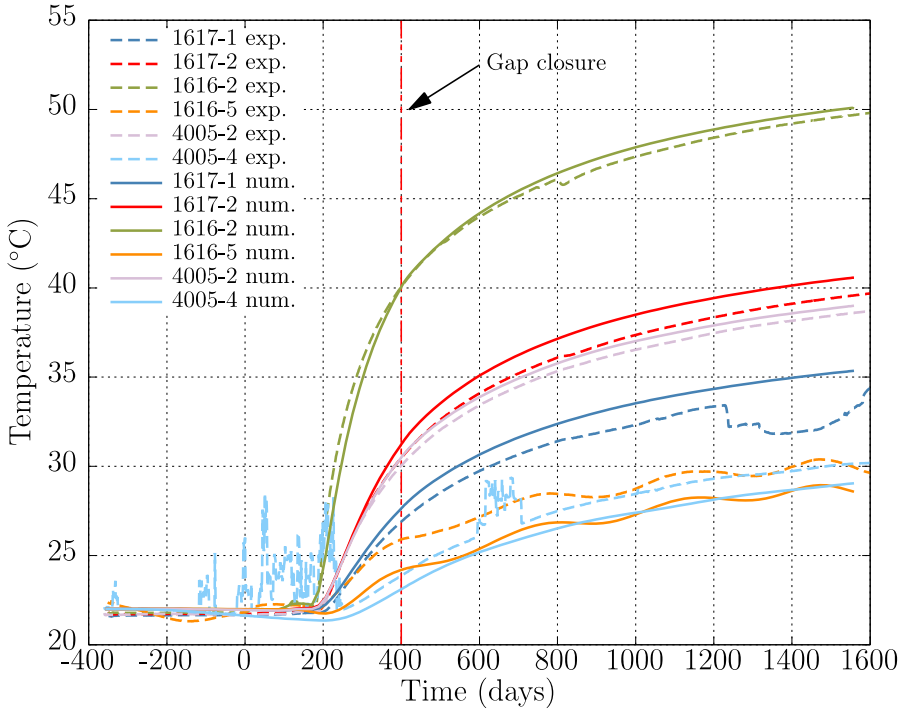

Figure 5-15. Simulated and observed temperature evolution at measuring points.

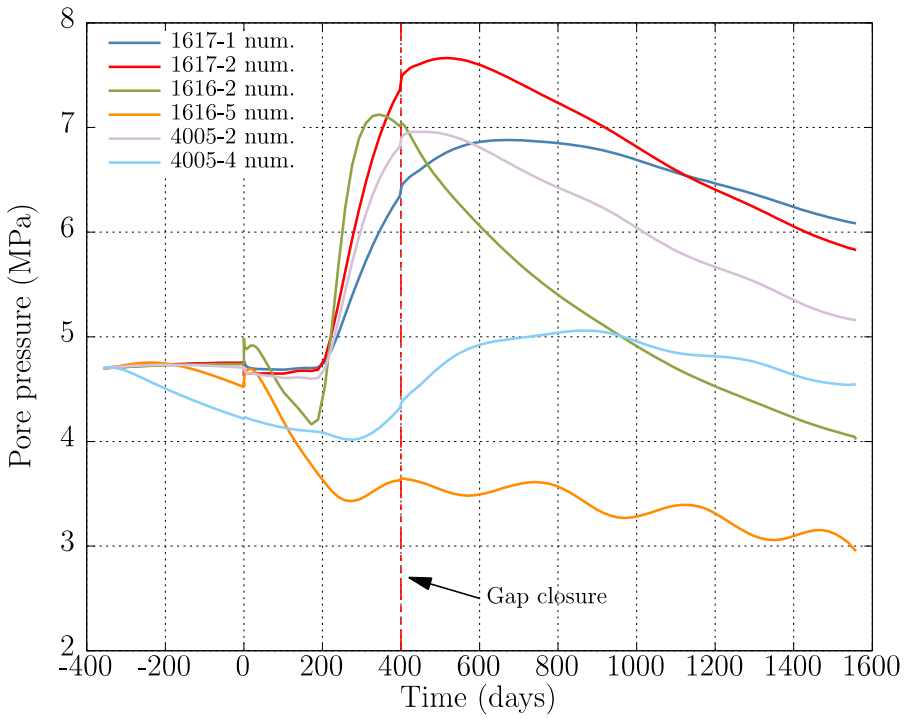

Figure 5-16. Simulated pore pressure evolution at sensor points.

In FY2018, we have investigated the THM behavior of COx rock associated with the ALC experiment with the TOUGH-FLAC simulator. In the numerical simulation, excavation of tunnels and boreholes were explicitly computed, and drainage conditions were applied at boreholes. A good agreement was achieved between numerical simulation and experimental observation of temperature. After we receive the measured data on pore pressure from the experiment team, we will compare our results with the experimental data, which will help us to understand THM processes in COx host rock.

5.3 Summary and Status of the Bure Heater Experiment Modeling

In FY2018, along with Task E of the DECOVALEX-2019 project, we have updated our model to simulate coupled THM processes associated with the TED *in situ* heating test performed in COx claystone, and completed new simulations to predict THM processes at the larger scale ALC *in situ* heating experiment. The current progress on this task is:

- For Step 1, we have corrected the analytical solution results of stress for the 3D THM modeling benchmark problem, a good agreement was achieved between our model simulation and theoretical solutions.
- For Step 2, we have determined THM parameters of claystone from the TED experiment, including calibration on thermal conductivities to match the temperature evolution during the heating phase, and back analysis on the simulation results to correct permeability. The heating phase of the TED experiment has been simulated with TOUGH-FLAC with good match to experimental data.
- For Step 3, we predicted THM behavior of COx clay stone during the ALC experiment by utilizing parameters of claystone from calibrated from the modeling of the TED experiment. The heating phase of the ALC experiment has been simulated with TOUGH-FLAC to experimental temperature data. We will compare our result on pore pressure with experimental data after we receive the measured data from the DECOVALEX-2019 Task E coordinators.

The next step for the rest of FY2018 and FY2019 will be to model Step 4 of DECOVALEX-2019 Task E; that is, we will conduct model predictions at the repository scale of an area with several high level waste cells.

This page intentionally left blank.

6. MODELING OF GAS MIGRATION IN CLAY USING TOUGH-FLAC AND TOUGH-RBSN (DECOVALEX-2019)

In this section, we present LBNL's activities for modeling gas migration in clay related to Task A of the DECOVALEX-2019 project. This is an international collaborative activity, in which DOE and LBNL gain access to the results of unique laboratory experiments of gas migration. These results are now used for numerical modeling to better understand the processes, to improve numerical models, and which will ultimately be applied in the performance assessment of nuclear waste disposal in clay host rocks and bentonite backfill. The Task A of DECOVALEX-2019 is coordinated by the British Geological Survey (BGS), that is also sharing their extensive data set on coupled THM responses during gas migration in bentonite and clay stone. In FY2018 LBNL has continued to participate in Task A of DECOVALEX-2019, as one of 11 international research teams (a list of research teams in given in Section 6.2), and conducted new simulations of gas flow through bentonite with comparison to the experimental data. In the following, we first introduce the issue of gas migration, the DECOVALEX-2019 tasks, experimental data and finally the LBNL modeling results.

6.1 Gas Migration in Clay

Gas migration in clay-based buffer materials has been the subject of a number of international research programmes in the field of nuclear waste disposal, including both laboratory scale and *in situ* experiment (e.g. Horseman et al., 2004; Harrington et al., 2012; Cuss et al., 2014). Substantial insight has been gained in the phenomenology of gas transport processes in bentonite and clay stone under different THM conditions. A number of model approaches have been proposed for the interpretation of the experimental results and for the analysis of gas release scenarios from geological repositories in the context of long-term safety assessment. The predictive capability of the gas transport models is yet limited, indicating that basic mechanisms of gas transport in bentonite are not understood in sufficient detail to provide the ground for robust conceptual and quantitative models.

The processes governing the movement of repository gases through bentonite and argillaceous host rocks can be split into two components: (1) molecular diffusion (governed by Fick's law), and (2) bulk advection (Harrington, 2016). In repository concepts such as the Swedish KBS-3, corrosion of metallic materials under anoxic conditions will lead to the formation of hydrogen. Radioactive decay of the waste and the radiolysis of water are additional source terms. If the rate of gas production exceeds the rate of gas diffusion within the pores of the barrier or host rock, a discrete gas phase will form. Under these conditions, gas will continue to accumulate until its pressure becomes sufficiently large for it to enter the surrounding material.

Four primary phenomenological models describing gas flow, shown in Figure 6-1, can be defined as following: (1) gas movement by diffusion and/or solution within interstitial fluids along prevailing hydraulic gradients; (2) gas flow in the original porosity of the fabric, commonly referred to as viscocapillary (or two-phase) flow; (3) gas flow along localized dilatant pathways, which may or may not interact with the continuum stress field; and (4) gas fracturing of the rock similar to that performed during hydrocarbon stimulation exercises (Harrington, 2016).

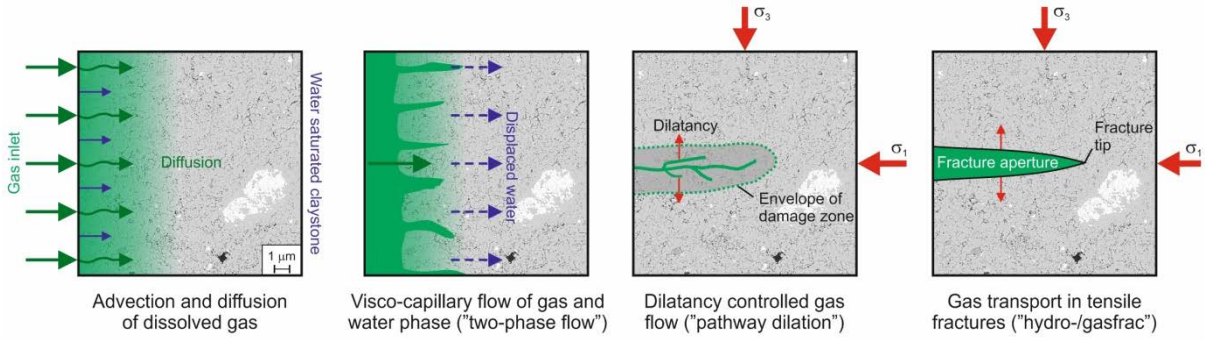

Figure 6-1. Conceptual models of gas flow (Harrington, 2016)

Studies on gas migration in clays (Horseman et al., 1999; 2004; Harrington and Horseman, 1999) indicate that classic concepts of porous medium two-phase flow are inappropriate and continuum approaches to modeling gas flow may be questionable, depending on the scale of the processes and resolution of the numerical model. However, the detail of the dilatant mechanisms controlling gas entry, flow and pathway sealing are unclear. As such, development of new and novel numerical representations for the quantitative treatment of gas in clay-based repository systems is therefore required (Harrington, 2016).

6.2 DECOVALEX-2019 Task A and International Modeling Teams

The purpose of Task A in DECOVALEX-2019 is to obtain better understanding of the processes governing the adjective movement of gas in low permeability clay barrier materials (Harrington, 2016). Special attention is given to the mechanisms controlling factors such as gas entry and flow, as well as pathway stability and sealing, which will impact barrier performance. In Task A of DECOVALEX-2019, new numerical prediction of gas fluxes will be developed by the participating international modeling teams. The models will be tested against a series of controlled laboratory tests, in a staged manner, building in complexity (both in terms of the experimental and modeling approaches). It is anticipated that the development of these models will provide a valuable tool to assess the impact of gas flow on barrier and host materials, providing information which could be used to support future repository design.

Data from a series of flow tests performed on initially saturated samples will be made available to project participants. These long-term tests, performed under carefully controlled laboratory conditions, provide detailed datasets applicable to examine gas migration behavior under steady state conditions. As such, a number of test geometries have been used, ranging in complexity from relatively simple one-dimensional flow tests on bentonite to triaxial tests performed on natural samples of COx claystone. To gain insights into the adjective movement of gas through these materials, laboratory data will be used to guide and benchmark numerical model development in an iterative process, increasing in model complexity from one test stage to the next (Harrington, 2016).

The initial plan of the task includes 4 distinct stages (Harrington, 2016):

- Stage 0: Code development:
  - Initial aim is to understand and reflect on the apparent fluctuating behavior of all experimental data. References and publications will be made available and the teams will be asked to develop one or more modeling approaches.
- Stage 1: 1D gas flow through saturated bentonite under controlled laboratory conditions

    - Data will be provided from a 1D gas flow test, performed on saturated bentonite subjected to a constant volume boundary condition.
- Stage 2: 3D spherical gas flow under controlled laboratory conditions
    - A: spherical flow through saturated bentonite, under a constant volume boundary condition.
    - B (optional): a second dataset under the same experimental boundary conditions is also offered, against which the models can be tested.
- Stage 3: Application of previous models to a natural clay-based system
    - A: triaxial test performed on a sample Callovo-Oxfordian claystone (COx). This dataset comprises a number of stages including initial hydration, hydraulic testing and gas injection.
    - B (optional): gas flow through hydrated bentonite pellets under constant volume conditions. If appropriate, data from a long-term test performed by the Commission for Atomic Energy and Alternative Energies (CEA) will be made available for Teams participating in this task.

The following international organizations and modeling teams are involved in DECOVALEX-2019, Task A (gas migration in clay):

- UK: British Geological Survey (BGS-Task Leader).
- UK: Quintessa
- Germany: Bundesanstalt für Geowissenschaften und Rohstoffe (BGR)
- Germany: Helmholtz-Centre for Environmental Research (UFZ)
- USA: Sandia National Laboratory
- USA: Lawrence Berkley National Laboratory
- France : Institut de Radioprotection et de Sûreté Nucléaire (IRSN)
- Korea: Korea Atomic Energy Research Institute (KAERI)
- Canada: Canadian Nuclear Safety Commission (CNSC)
- Spain: Universitat Politècnica de Catalunya (UPC)
- Taiwan: Taiwan Power Company (Taipower)

The research teams have completed Stage 1 (1D gas flow test) and are currently working on Stage 2 (3D spherical gas flow). Related to the initial Stage 0, initial code development was completed though the code development continues along with modeling of the various experimental data in Stages 1 through 3. In Section 6.3, we briefly present Stage 1 and Stage 2 experimental data. In FY2018 LBNL has updated simulations of Stage 1 (1D gas flow test) as well as completely new simulations of Stage 2 (3D gas flow test).

6.3 Laboratory Experiments of Gas Migration in Bentonite

Stage 1 experimental data consists of 1D gas flow test through a saturated sample of MX-80 bentonite. The experimental data is provided to the DEOCOVALEX-2019 modeling teams by the task coordinators from BGS, who is also conducting the gas-migration experiments. The experiment is conducted on a cylindrical bentonite sample, 120 mm in height and 60 mm in diameter. The sample is placed in a pressure vessel that allows for monitoring of the evolution of pressure and stress at different locations along the sample, as well as inflow and outflow rates through filters (Figure 6-2).

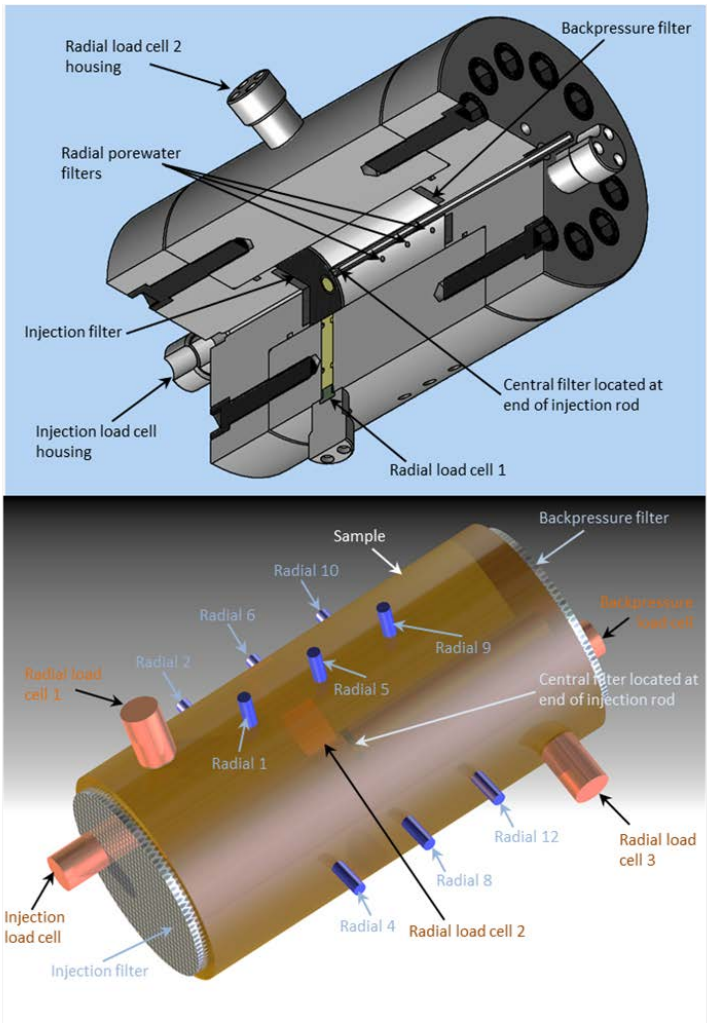

Figure 6-2. Above: Cut-away diagram of the pressure vessel showing the apparatus components and instrumentation. Below: image of the sample showing the relative positions of the load cells and pore pressure filters (Harrington, 2016).

Part of the experimental results related to pressure and outflow is shown in Figure 6-3. In the experiment, the bentonite sample was hydrated prior to gas testing through all radial and backpressure filters. The water was infiltrated and equilibrated at a pressure of 1 MPa. The hydration resulted in swelling and development of swelling stress within the sample (not shown here). Once total stress began to plateau, helium gas was introduced in to the injection filter at an initial pressure of 3 MPa (blue line in Figures 6-3a and b). This was left to equilibrate with the water in the pump for seven days. Thereafter, gas was injected into the injection chamber resulting in a gradual increase of injection gas pressure (blue line in Figures 6-3a and b), while keeping the back pressure constant at 1 MPa (yellow line in Figure 6-3a). When the injection pressure reached about 10 MPa, an abrupt increase in pressure was observed at monitoring points along the sample (green, red, purple lines in Figure 6-3a). At the same time there was a sudden temporal increase of gas outflow (green line in Figure 6-3b). The injection was then shutdown and the injection pressure went down slowly along with the pressure measured at other points along the sample.

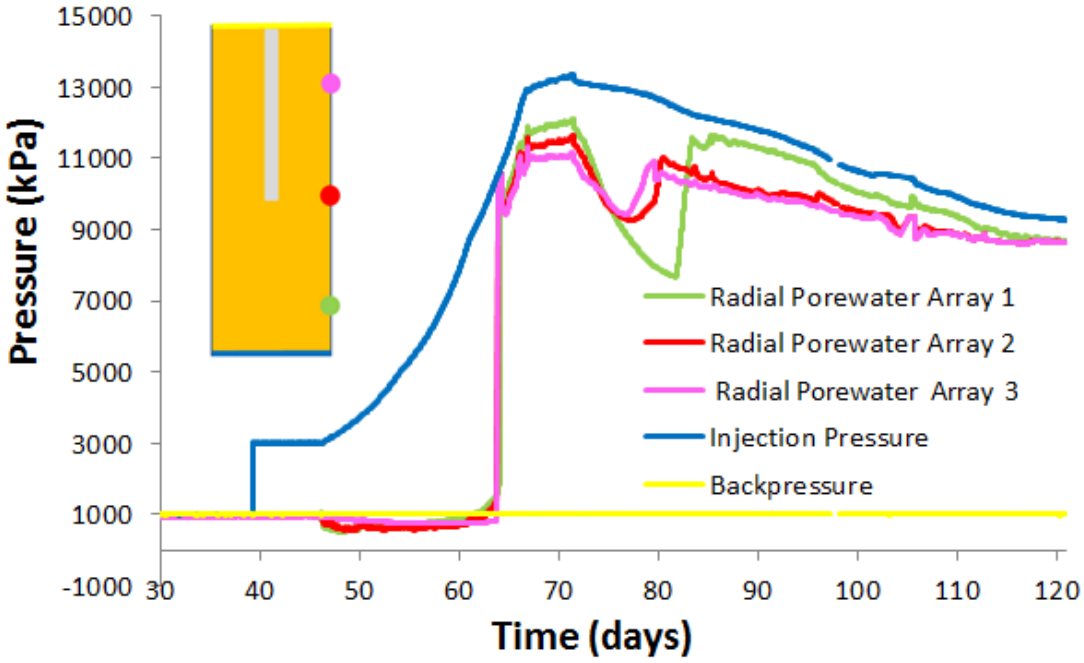

(a)

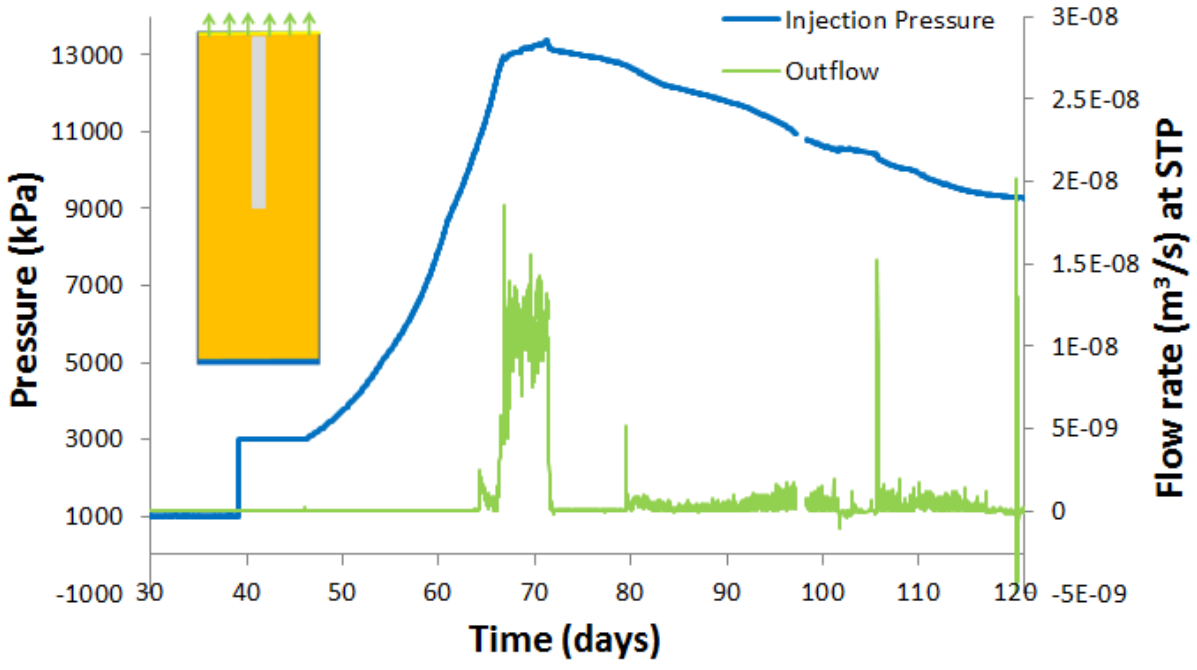

(b)

Figure 6-3. Observed (a) pressure evolution and (b) outflow rate (Modified from Harrington, 2016).

Stage 2 experimental data were collected to describe 3D spherical gas flow through a saturated sample of MX-80 bentonite. The experiment has been conducted by BGS, who has also tested the 1D gas flow through bentonite to obtain the Stage 1 experimental data. They have adopted the same sample geometry as used in Stage 1, but varied the injection location from one side of base surface (Figure 6-4a) to the center of the sample (Figure 6-4b). Staged hydration and gas injection processes have been carefully controlled over 700 days to minimize the perturbation of the system/sample and better reflect realistic conditions of a deep geological disposal facility. The DECOVALEX teams performed numerical simulations of coupled gas pressure and stress responses for the period from 735 to 835 days, when the gas breakthrough occurred.

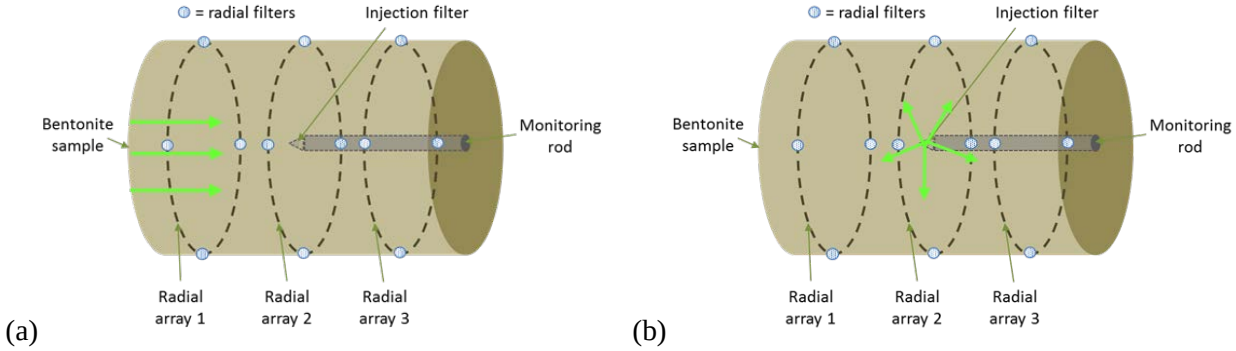

Figure 6-4. Schematic drawings of gas injection location and gas flow direction for (a) 1D gas flow test (Stage 1) and (b) spherical gas flow test (Stage 2).

Figure 6-5 shows experimental results in terms of pressure/stress evolutions and inflow/outflow rates between 735 days and 835 days of gas injection. Standard temperature and pressure (STP) are defined as 273.15 K, 101.325 kPa respectively. The peak in gas pressure (around day 767.6) is followed by a protracted negative pressure transient leading to a quasi-steady state by around day 825 (Figure 6-5a). During this period, the change in injection pressure is crudely mirrored by stress which exhibits none of the apparent chaotic patterns observed at earlier breakthrough events. The reduction in the variability of stress from day 768 onwards is accompanied by the development of stable outflow conditions, with flux localized to one drainage array (Figure 6-5b).

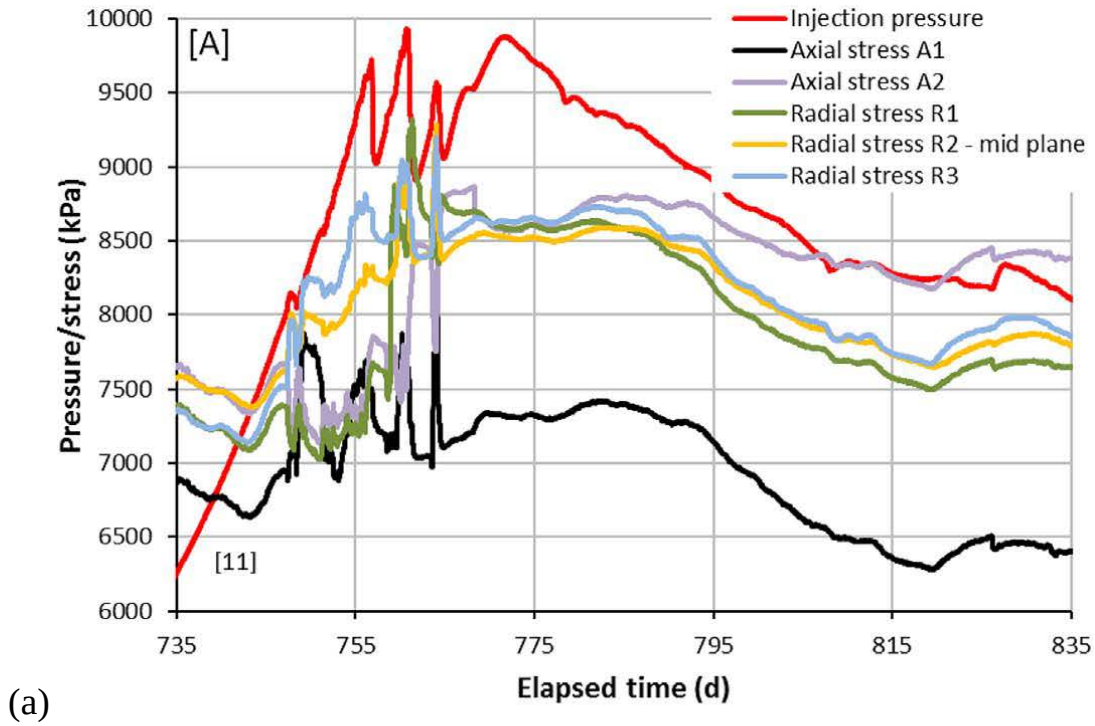

(a)

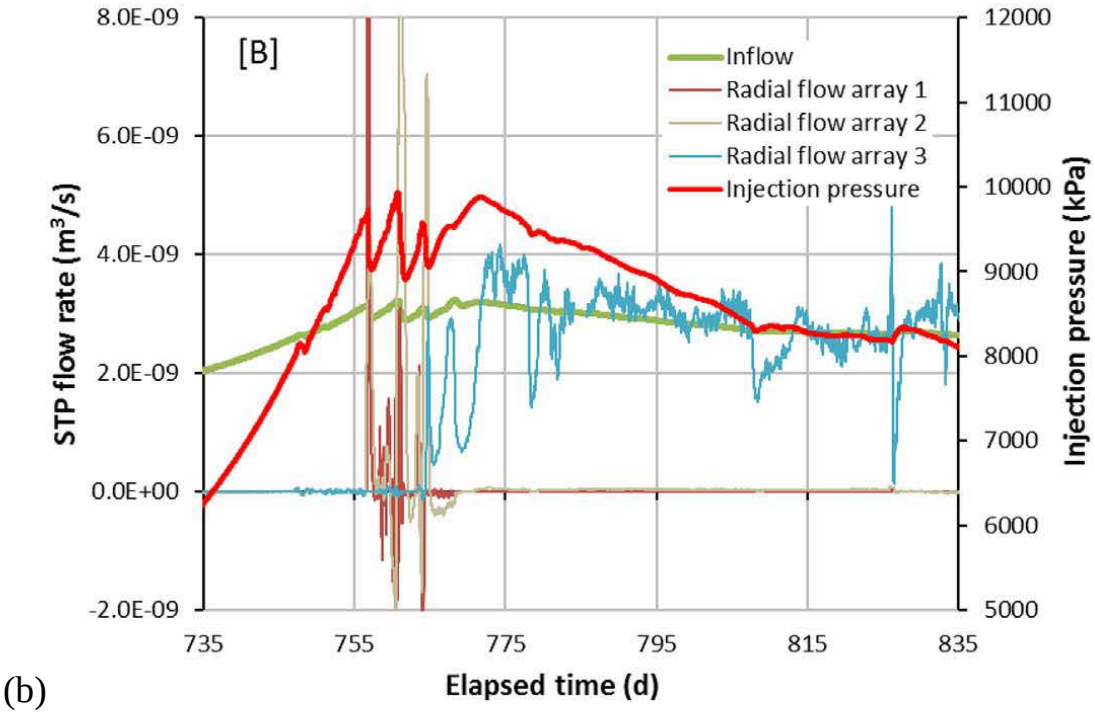

(b)

Figure 6-5. Observed 3D spherical gas flow test results: (a) pressure/stress evolutions and (b) inflow/outflow rates (Harrington et al., 2017).

6.4 LBNL Model Approaches for Gas Migration

LBNL is exploring two different approaches for modeling gas migration associated with DECOVALEX-2019, Task A (Figure 6-6):

1) Continuum modeling approach using TOUGH-FLAC simulator (Rutqvist, 2011), and

2) Discrete fracture modeling approach using TOUGH-RBSN simulator (Kim et al., 2017)

The two approaches are complementary. The continuum approach is based on current developments and applications of TOUGH-FLAC on bentonite and clay host rocks for the modeling of long-term THM performance of nuclear waste repositories in clay host rocks. The TOUGH2 code and other continuum models have been used in the past to model gas migration in clay considering heterogeneous clay properties with pressure dependent permeability, but without considering geomechanical coupling (e.g., Senger and Marschall, 2008; Senger et al., 2014). In this study, such a continuum approach will be extended to include full geomechanics coupling within the framework of TOUGH-FLAC. The discrete fracture modeling approach is based on current development of the TOUGH-RBSN simulator, in which the opening of grain boundaries for dilatant gas migration is modeled explicitly using a fracture mechanics approach. The TOUGH-RBSN has previously been applied for modeling fluid driven hydraulic fracturing and complex fracturing in clay host rocks (Kim et al., 2017). The TOUGH-RBSN should be suitable for modeling of complex flow paths associated with dilatant gas migration in clays.

In Sections 6.4 and 6.5, the continuum and discrete modeling results are presented, respectively. They cover the experimental works for Stage 1—1D gas migration and provide preliminary simulation results, and for Stage 2—spherical gas migration through a 120 mm long sample of water saturated MX-80 bentonite.

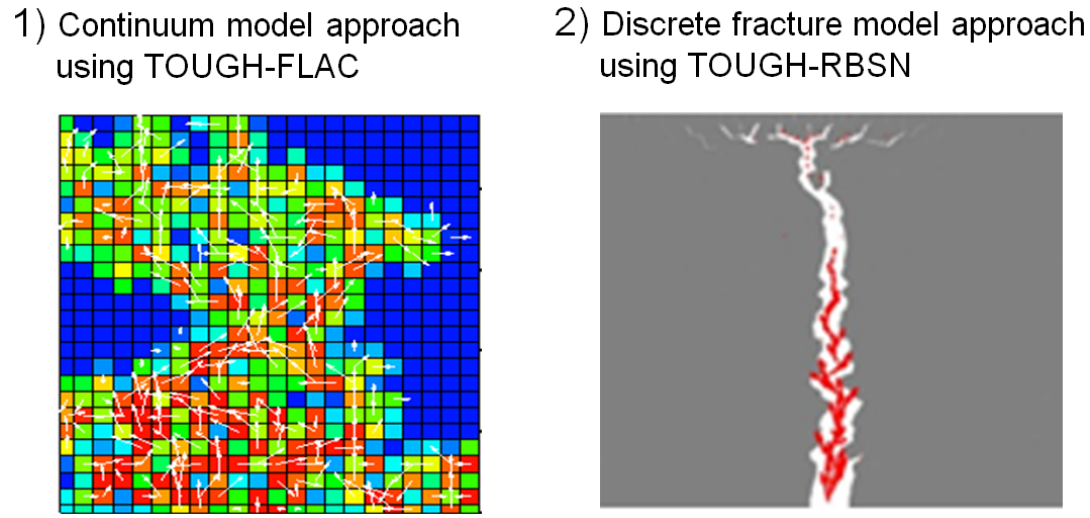

Figure 6-6. Schematic of modeling approaches employed by LBNL for modeling gas migration through clay associated with DECOVALEX-2019 Task A. To the left, the continuum approach using TOUGH-FLAC is illustrated involving heterogeneous properties with the possibility of the formation of dilatant flow paths through pressure or strain dependent permeability in individual cells. The actual color figure to the left is from TOUGH2 modeling in Senger and Marschall (2008), in which the white arrows show gas flow velocity and colors are gas saturation. To the right, the discrete fracture modeling approach using TOUGH-RBSN, involving complex fracturing to simulate the formation of dilatant flow paths. The red shows the fluid flow pathways through the fracture shown in white color.

6.5 TOUGH-FLAC Modeling of Gas Migration Experiments

In FY2018, the continuum modeling results have been updated based on the comparison to experimental data. Based on a large number of simulation tests with comparison to experimental data, we arrived at the following basic approach and material models

1) Multiphase (gas and liquid) flow;
2) Linear poro-elastic model;
3) A linear moisture swelling model;
4) A gas permeability model related to minimum effective compressive stress.

The linear poro-elastic model is based on the assumption of a linear elastic response, and we assume an effective stress law, which responds to the maximum phase pore pressure, which could be either gas pressure (for partially saturated media) or liquid pressure (for fully saturated media). That is:

$$\sigma' = \sigma - P^{\emptyset} \tag{6.1}$$

where

$$P^{\emptyset} = Max\left(P^{l}, P^{g}\right) \tag{6.2}$$

where P^{ϕ} is the pore pressure, and P^{l} *and* P^{g} are liquid and gas phase pressures, respectively.

The linear moisture swelling model implies a swelling strain as a function of liquid saturation, leading to a swelling stress according to

$$\Delta\sigma_{sw} = 3K\Delta\varepsilon_{sw} = 3K\Delta S_{l}\beta_{sw} \tag{6.3}$$

where S_l is liquid saturation, and β_{sw} is the moisture swelling coefficient. These models have been used in the past for simplified modeling of bentonite behavior, and are described in Rutqvist et al. (2011). The applied gas permeability model considers a fracture-like behavior of permeability for dilatant flow paths (Figure 6-7). In this model, permeability is a non-linear function of the effective minimum compressive stress.

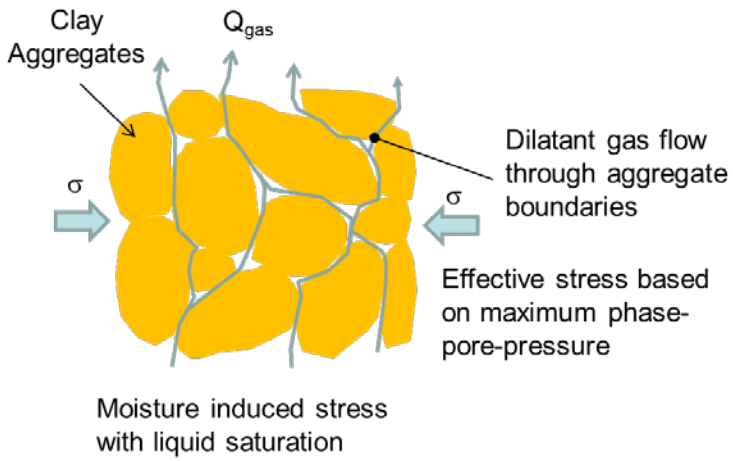

Figure 6-7. Conceptual model for dilatant gas flow through aggregate boundaries considered in a continuum model simulations with TOUGH-FLAC.

A full 3D model has been developed to model heterogeneous material properties. However, the modeling simulations conducted to date have been done assuming homogeneous properties of the MX-80. The test geometry in this case is a 3D model as shown in Figure 6-8. The sample dimensions are 120 mm long and 60 mm diameter. We included additional elements on the top and bottom in the TOUGH2 fluid flow domain to simulate the injection and back-pressure filters.

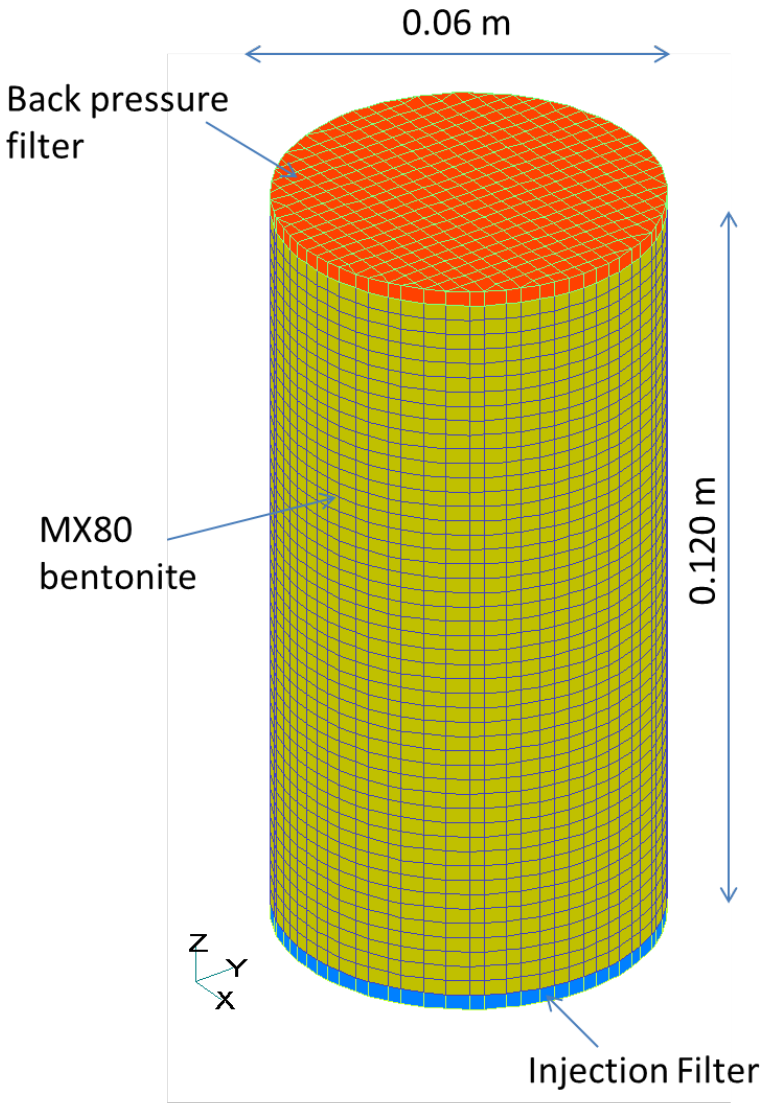

Figure 6-8. 3D TOUGH-FLAC model of cylindrical sample.

Initial conditions of 1 MPa fluid pressure and fully water saturated sample were used for modeling. In the current modeling, the injection pressure was controlled at the injection boundary elements at full gas saturation, with variable pressure ranging according to measured data. A back pressure of 1 MPa was maintained in the elements simulating the back pressure filter. The simulation starts at 20 days assuming fully saturated sample, the initial axial stress of

9.5 MPa and the radial initial stress of 6.5 MPa. In simulations, the sample was assumed to be mechanically confined.

Numerous sensitivity studies were conducted for matching the simulation results. Finally, some material properties were fixed, while others where used for final matching of simulation results. Table 6-1 lists the basic and specific material parameters that will be explained. The parameters marked in bold in Table 6-1 were calibrated. Other parameters were fixed, including those denoted as basic reference values, which are typical values for MX-80 bentonite and given by the DECOVALEX-2019 task lead.

Table 6-1. Material parameters for TOUGH-FLAC modeling of Stage 1 experiment.

	Meaning	**Symbol [units]**	**Value**
Basic reference values	Young's modulus	E [MPa]	307
	Poisson's ratio	ν [-]	0.4
	Porosity	ϕ_0 [-]	0.44
	Intrinsic permeability	k_0 [m^2]	3.4×10^{-21}
HM coupling parameters	Pore compressibility[1]	c_p [Pa^{-1}]	4.44×10^{-9}
	Biot's coefficient	α_p [-]	1
	Swelling coefficient	$\boldsymbol{\beta_{\beta sw}}$ **[-]**	**0.02**
	Max aperture for stress-k	**bho [m]**	$\mathbf{29x10^{-6}}$
	Reference stress for stress-k	$\boldsymbol{\sigma_{n,ref}}$ **[MPa]**	**0.2**
van Genuchten capillary pressure model	Apparent gas entry pressure	P_0 [MPa]	18
	Residual liquid saturation	S_{lr} [-]	0.01
	Shape factor	λ [-]	0.45
Corey relative permeability	Residual liquid saturation	S_{lr} [-]	0.1
	Residual gas saturation	$\boldsymbol{S_{gr}}$ **[-]**	**0.11**
	Enhancement factor for k_{rg}	$\boldsymbol{m_g}$ **[-]**	**375**

Based on the results of matching the stress evolution from experimental data and modeling, it is required to consider both the poro-elastic stress changes and the moisture swelling effect. During gas injection, the poro-elastic stress change will tend to increase the compressive stresses, because the sample is confined mechanically. The poro-elastic stress increase is roughly proportional to the pressure changes, which far exceeds the observed stress changes. However, considering the effect of moisture swelling, or in this case shrinkage due to reduced water saturation as gas is injected, some of the poro-elastic stress changes will be offset and the observed stress evolution can be matched reasonable well. In the simulations the

Young's modulus was fixed to 307 MPa, which is a reasonable approximation for saturated or near saturated bentonite, taking into account the dry density and a confining stress. To match the observed stress magnitude as moisture swelling parameter of 0.02 was determined through sensitivity analysis. Poisson's ratio was set to 0.4.

The van Genuchten (1980) capillary pressure model is used to define the water retention curve given by

$$P_c(S) = P_0\left([S^*]^{-1/\lambda} - 1\right)^{1-\lambda} \tag{6.4}$$

with $S^* = (S - S_{lr})/(1 - S_{lr})$. The relevant capillary pressure parameters are adopted for bentonite (Senger and Marschall, 2008): apparent gas entry pressure P_0=18 MPa, shape factor λ=0.45, and residual liquid saturation S_{lr}=0.01.

The relative permeability-saturation relationships of liquid and gaseous phases are parameterized using Corey's model as

$$\begin{aligned} k_{rl}(S) &= \hat{S}^4 \\ k_{rg}(S) &= m_g\left(1 - \hat{S}\right)^2\left(1 - \hat{S}^2\right) \end{aligned} \tag{6.5}$$

where $\hat{S} = (S - S_{lr})/\left(1 - S_{lr} - S_{gr}\right)$, and m_g is a multiplying factor for the enhanced gas permeability (Corey, 1954). The residual saturations S_{lr} and S_{gr} are provided to limit the mobility of the respective phase, i.e., both liquid and gaseous phases mobility can vary only in the range of $S = \left[S_{lr}, 1 - S_{gr}\right]$.

For matching the abrupt gas breakthrough occurred at a gas pressure of about 10 MPa in the gas injection chamber, the concept of an effective gas entry pressure, P_{ge}, was applied according to Senger and Marschall (2008). The concept is illustrated in Figure 6-9, where a residual gas saturation of S_{gr} = 0.11, which is a parameter of the gas relative permeability function) corresponds to the effective gas entry pressure P_{ge} = 10 MPa.

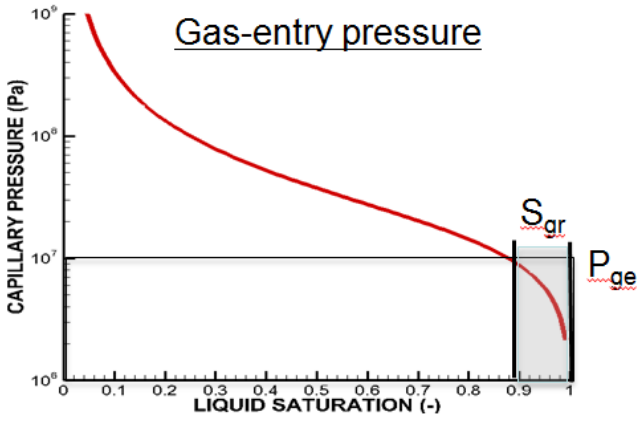

Figure 6-9. The concept of effective gas entry pressure used for the evaluation of the initial pressure response.

In the current simulations, the intrinsic permeability was set to a fixed value of $k = 3.4\times10^{-21}$ m^2 based on other independent laboratory tests. The gas entry pressure was necessary to prevent any gas migration and pressure changes to occur in the sample until about 60 days, when abrupt increases of sample pressure occurred. The gas permeability can increase more strongly with the gas saturation as well as a result of changes in effective stress. A relation between permeability and effective minimum compressive stress is shown in Figure 6-10. The two parameters, bh0 = 2.9×10^{-6} m, and $\sigma_{n,ref} = 0.2\times10^{6}$ Pa were determined by trial simulations to obtain the best possible match with experimental data.

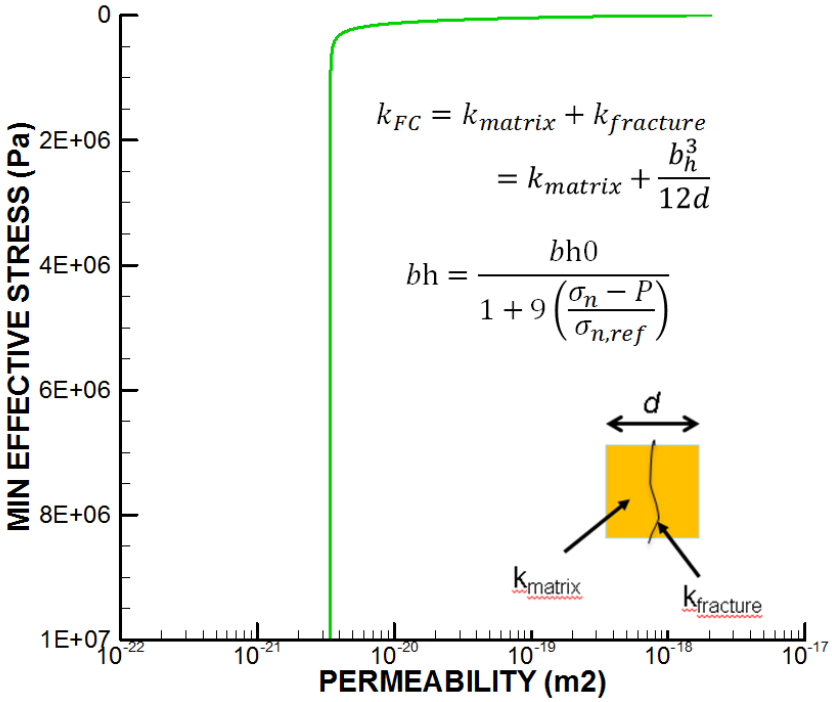

Figure 6-10. Relation between min effective stress and permeability used in numerical modeling.

The simulation results with comparison to measured data are shown in Figures 6-11 to 6-14. The measured abrupt pressure increase within the sample after about 67 days was captured very well in the modeling (Figure 6-11). The subsequent general pressure decline is also captured, though some of the pressure fluctuations at around 80 days are not captured in the modeling. .

The abrupt increase in outflow rate and the maximum magnitude is also accurately captured in the modeling (Figure 6-12). The observed subsequent complete shut-down of gas flow is not captured in the modeling, which shows a more gradual decline in gas flow rate.

The general evolution and magnitudes in radial and axial stresses are also modelled quite accurately (Figures 6-13 and 6-14). The modeling shows a bit more uniform stress compared to the data, and the stress decline toward the end is not captured in the modeling.

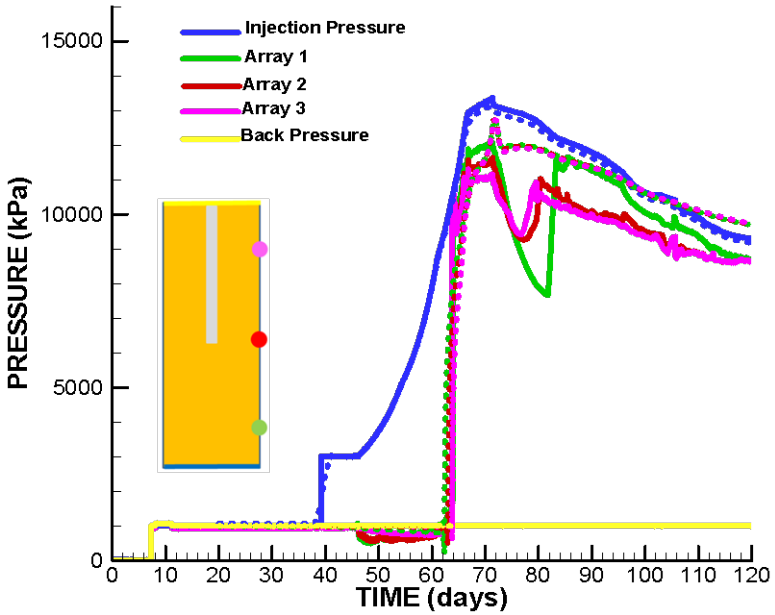

Figure 6-11. 3D TOUGH-FLAC model of cylindrical sample and the results of simulations of pressure.

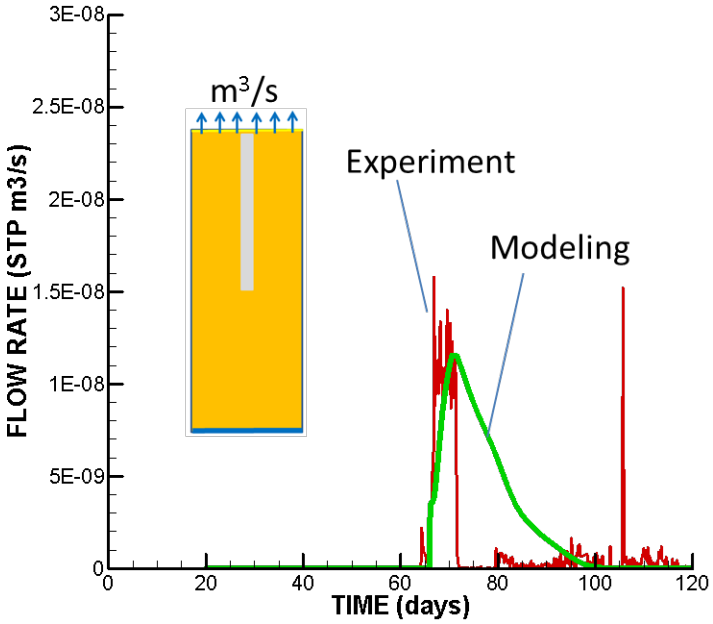

Figure 6-12. Simulated (green line) and measured (red line) gas flow rate out of the sample.

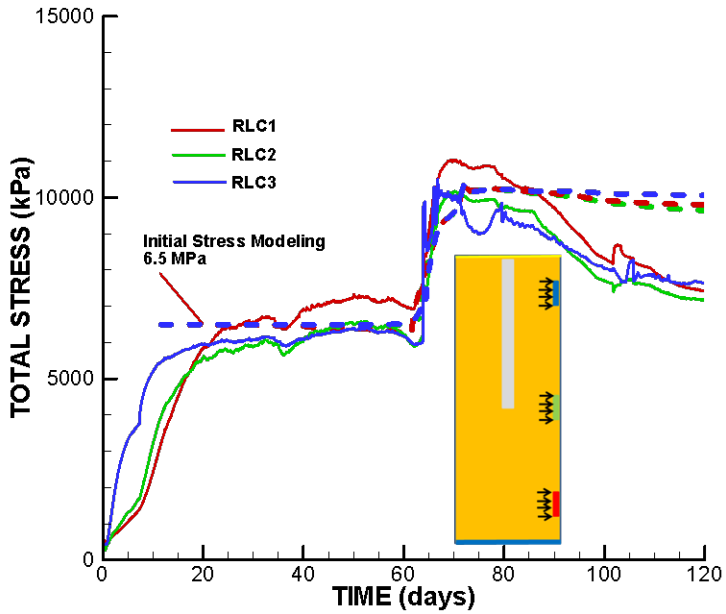

Figure 6-13. Simulated (dashed lines) and measured (solid lines) total radial stress at load cells 1, 2 and 3.

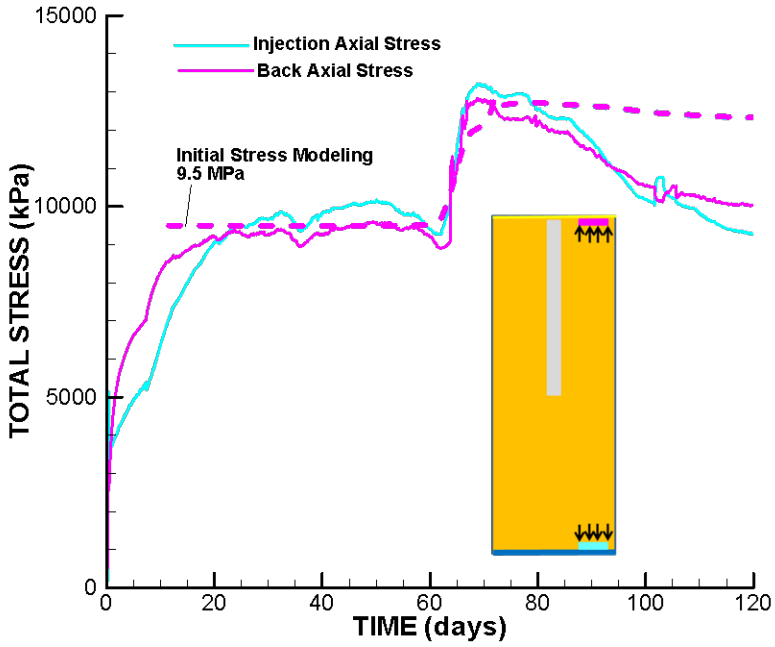

Figure 6-14. Simulated (dashed lines) and measured (solid lines) total axial stress at injection and back ends of the sample.

In summary, the homogeneous material model with simple linear poro-elastic and moisture swelling model and model for stress-dependent gas permeability, and an effective gas entry pressure, could capture the main features of the experiment, including pressure, stress and flow evolution. The biggest deviation from the data occurred just after 70 seconds, when the experimental gas flow appears to shut-down completely.

Future improvements to this model could include:

1. Application of the BBM for matching stress evolution;
2. Modeling of the injection system and imposed flow rate rather than imposing the injection pressure;
3. Modeling of the initial stage of loading and saturation of the sample; and
4. Utilizing heterogeneous properties of media in the model development.

The BBM is used to simulate the non-linear elastic (rather than linear elastic) mechanical behavior, and, therefore, it might be possible to better match the stress evolution post 70 seconds. Taking into account heterogeneous properties will help simulate the formation of localized flow paths, which would be especially important for modeling the Stage 2A, 3D spherical flow experiment.

6.6 TOUGH-RBSN Modeling of Gas Migration Experiments

We have used the TOUGH-RBSN simulator for modeling two-phase flow with mechanical deformation and fracture/damage processes. The TOUGH-RBSN simulator is distinguished from continuum-based approaches (e.g., TOUGH-FLAC) by its capability of the discrete representation of fracture formations affected by coupled THM processes. The general coupling procedure of TOUGH-RBSN is similar to the sequential coupling in TOUGH-FLAC (Rutqvist et al., 2002; Rutqvist, 2011), but the TOUGH-RBSN coupling modules have been substantially modified to account for the fluid flow through discrete fractures (Asahina et al., 2014; Kim et al., 2017).

This section presents simulations of two types of gas flow experiments: (1) 1D flow through a saturated bentonite (MX-80) sample, and (2) spherical flow in a saturated bentonite sample. The 2D rectangular and 3D cylindrical models for numerical simulations were generated based on the Voronoi discretization. The discrete fracture network (DFN) approach was used to demonstrate enhanced gas flow through discrete fracture paths. Simulated porewater pressure, total stress, and flow rate were compared with the laboratory test results for model validation. Comparison of fracture patterns and pressure distributions during fracturing processes were used for the qualitative analysis of gas pressure-induced fracture propagation and fracture-assisted flow.

6.6.1 1D flow through saturated bentonite under constant volume boundary conditions

A 120×60 mm rectangular 2D mesh was constructed, comprising of 1401 Voronoi cells and 3840 lattice elements. An additional 2 mm-thick layer of elements was padded on each side of the domain boundaries to provide a uniform mechanical confinement (i.e., fixed displacement boundary conditions). Figure 6-15 shows the resulting mesh geometry, where colored marks indicate the measuring points of pressure evolutions during simulations.

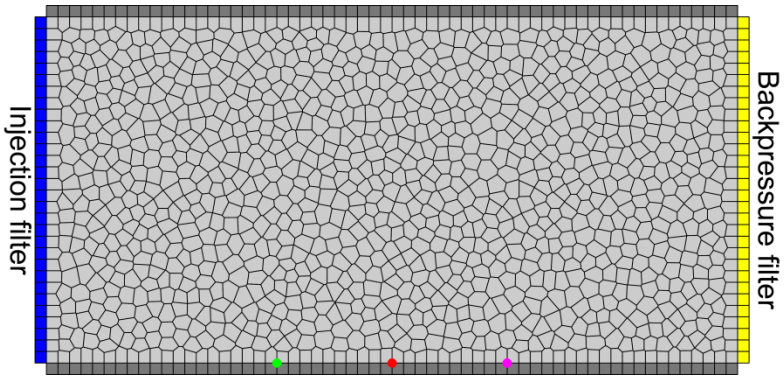

Figure 6-15. 2D rectangular model geometry of an MX-80 bentonite sample.

The initial confining stress values are given from the measurements of load cells in the experimental program, which reads 9 MPa in the axial direction and 6 MPa in the radial direction. The initial pore pressure was 1 MPa, and the initial saturation of the domain was 0.999 to represent fully saturated conditions. While the padding elements surrounding the specimen were fixed with the initial stress loaded, gas injection at the left boundary was controlled to match the injection pressure measured from the experiment. 1 MPa backpressure at the right boundary was upheld during simulations. Hydrologically, the left and right padding elements are highly permeable as for the filter boundaries, whereas the top and bottom elements have zero permeability representing insulation.

Table 6-2 lists the parameters for mechanical and hydrological model assumptions adopted in this study. The current TOUGH-RBSN model observes all the baseline parameters conforming to the values suggested from the DECOVALEX Task A coordinator from BGS. The Poisson's ratio of 0.4 is used for deriving the pore compressibility of the bentonite material. The RBSN models adopt the zero Poisson's ratio to avoid an unwilled artificial heterogeneity, which aggravates the elastic homogeneous representation in the mechanics of the lattice network. Pre-calibration processes have been performed to match the experimental data, and the calibrated parameters are given in the notes of Table 6-2.

Because of the granular texture of the bentonite sample, the grain-to-grain strength is considered to be very low. Herein, a Mohr-Coulomb failure criterion is adopted, for which the tensile strength f_t = 0.1 MPa, cohesive strength c = 0.1 MPa, and the internal friction angle β = 18°. Due to the fully confined boundary conditions with the initial pressure and stress conditions, the fracture surfaces are more likely to be in contact during simulations, and, thus, the mechanical resistance may exist between the fracture surfaces. In that sense, it is simply assumed that a fractured element regain the mechanical properties of intact material when the crack displacement indicates the fracture closure.

In the TOUGH-RBSN simulations, the TOUGH2 model configuration comprises of two types of elements. The first element type is the cell elements, whose geometry is associated to the Voronoi cells. The cell elements represent the matrix/grain bulk, for which the porosity-dependent permeability is defined as

$$k = k_0 \frac{\phi^3}{(1-\phi)^2} \frac{(1-\phi_0)^2}{{\phi_0}^3} \tag{6.6}$$

where k_0 is the intrinsic permeability, and ϕ_0 is the initial porosity.

Table 6-2. Material parameters for TOUGH-RBSN modeling of 1D gas flow through MX-80 bentonite samples.

	Meaning	Symbol [units]	Value
Basic reference values	Young's modulus	E [MPa]	307
	Poisson's ratio	ν [-]	0.4
	Porosity	ϕ_0 [-]	0.44
	Intrinsic permeability	k_0 [m^2]	3.4×10^{-21}
HM coupling parameters	Pore compressibility[1]	c_p [Pa^{-1}]	4.44×10^{-9}
	Biot's coefficient	α_p [-]	1
	Swelling coefficient[2]	α_s [-]	0.1
Mohr-Coulomb failure criterion	Tensile strength	f_t [MPa]	0.1
	Cohesive strength	c [MPa]	0.1
	Internal friction angle	β [deg.]	18
van Genuchten capillary pressure model[3]	Apparent gas entry pressure	P_0 [MPa]	18
	Residual liquid saturation	S_{lr} [-]	0.01
	Shape factor	λ [-]	0.45
Corey relative permeability	Residual liquid saturation	S_{lr} [-]	0.8
	Residual gas saturation[4]	S_{gr} [-]	0.0877
	Enhancement factor for k_{rg}	m_g [-]	1

Note:

[1] The pore compressibility is analytically derived from the bulk modulus K: $c_p = \frac{1}{K\phi} = \frac{3(1-2\nu)}{E\phi}$.

[2] The swelling coefficient is calibrated to match the peak values of total stress responses.

[3] The parameters are adopted from Senger and Marchall (2008).

[4] S_{gr}= 0.0877 corresponds to the air-entry pressure P_{ae}= 8 MPa, which is the pressure difference between injection and backpressure points at the breakthrough.

The other element type is the interface elements, which represent potential fractures or pre-existing fractures embedded in a portion of the matrix volume. It is assumed that the interface element is positioned at the common boundary of two adjacent cell elements, and one fracture plane cut the element into two parallel plates. The permeability is calculated as the sum of two components:

$$k = k_{matrix} + k_{fracture} \tag{6.7}$$

where each component is conditionally calculated based on the fracture activation. If an interface element is yet to be fractured, k_{matrix} is calculated based on Equation (6.6) and $k_{fracture}$ is simply assumed to be zero. On the other hand, if the interface element is fractured, $k_{fracture}$ will be predominant to enhance the

total permeability, and k_{matrix} is assumed to revert to the initial intrinsic permeability k_0. This conditional expression of the permeability is written as

$$k = \begin{cases} k_0 \frac{\phi^3}{(1-\phi)^2} \frac{(1-\phi_0)^2}{{\phi_0}^3}, & \text{if unfractured} \\ k_0 + \frac{b^3}{12a}, & \text{if fractured} \end{cases} \tag{6.8}$$

where a is the element width, and b is the aperture.

The van Genuchten capillary pressure Eq. (6.4) is used to define the water retention curve. The relevant capillary pressure parameters are adopted for MX80 bentonite (Senger and Marschall, 2008): apparent gas entry pressure P_0=18 MPa, shape factor λ=0.45, and residual liquid saturation S_{lr}=0.01.

The relative permeability-saturation relationships of liquid and gaseous phases are parameterized using Corey model as

The relative permeability-saturation relationships of liquid and gaseous phases are parameterized using Corey model as

$$\begin{aligned} k_{rl}(S) &= \hat{S}^4 \\ k_{rg}(S) &= m_g\left(1-\hat{S}\right)^2\left(1-\hat{S}^2\right) \end{aligned} \tag{6.9}$$

where $\hat{S} = (S - S_{lr})/\left(1 - S_{lr} - S_{gr}\right)$ and m_g is an multiplying factor for the enhanced gas permeability. The residual saturations S_{lr} and S_{gr} are provided to limit the mobility of the respective phase, i.e., both liquid and gaseous phases can vary their mobilities only in the range of $S = \left[S_{lr}, 1 - S_{gr}\right]$. Note that S_{lr}=0.8 in this equation is different from that in Equation (6.4) for the capillary pressure. To avoid unphysical situation with $P_c = \infty$, larger S_{lr} for the relative permeability is usually chosen as compared to S_{lr} for the capillary pressure (Pruess et al., 2012). Residual gas saturation, S_{gr}, can be used to define the air entry pressure in relationship with the capillary pressure function. S_{gr}=0.0877 corresponds to the air entry pressure of 8 MPa.

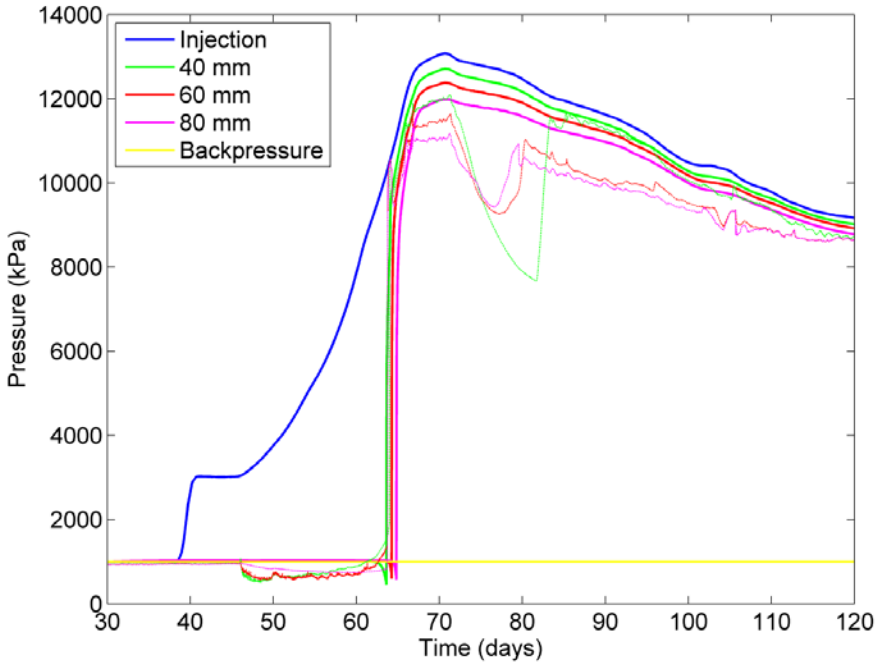

Figure 6-16. Comparison of simulated pressure (solid thick lines) with experimental data (dotted thin lines).

Figures 6-16 to 6-18 compare simulation results with the experimental data for pore pressure, axial and radial stress, and outflow rate over time, respectively. As shown in Figure 6-16, the simulated pore pressures exhibit an abrupt increase after around 65 days of injection, which are in a good agreement with the experimental data. In the post-peak region, the uniform pressure evolutions along the length indicate that permeability of the sample has increased after the gas breakthrough.

Figure 6-17 presents axial and radial total stress evolutions, which accord quite well with the experimental data. The initial stress configuration (σ_x:σ_y = 9 MPa:6 MPa) is maintained until the gas entry around 60 days due to the 8 MPa air entry pressure corresponding to the assigned residual gas saturation. The axial stresses measured at the injection boundary and the backpressure boundary both well agree with the experimental data (Figure 6-17a), and the radial stress evolution curves indicate the gas breakthrough with abrupt pressure increase (Figure 6-17b). Note that the linear swelling/shrinkage model with a calibrated coefficient α_s=0.1 is used to match the peak stress levels.

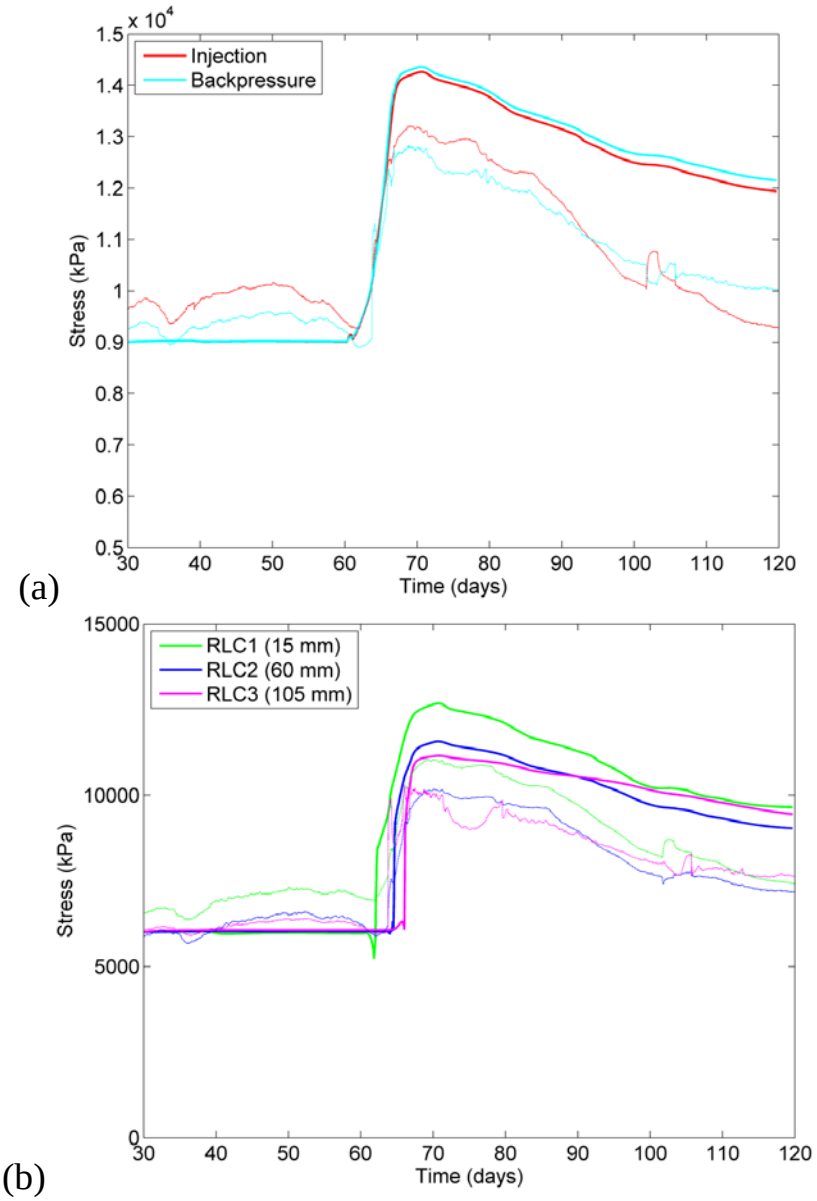

Figure 6-17. Comparisons of simulated (a) axial stresses and (b) radial stresses with experimental data.

In Figure 6-18, the simulated outflow rate could match the level of peak flow rate. However, the activation of outflow is delayed by about five days compared to the experimental result. We hypothesize that the simulations of the gas breakthrough process would be improved by changing the relative permeability function. Also, the complete cut-down of flow after 72 days is not captured since the injection boundary condition is not physically controlled by the flow rate.

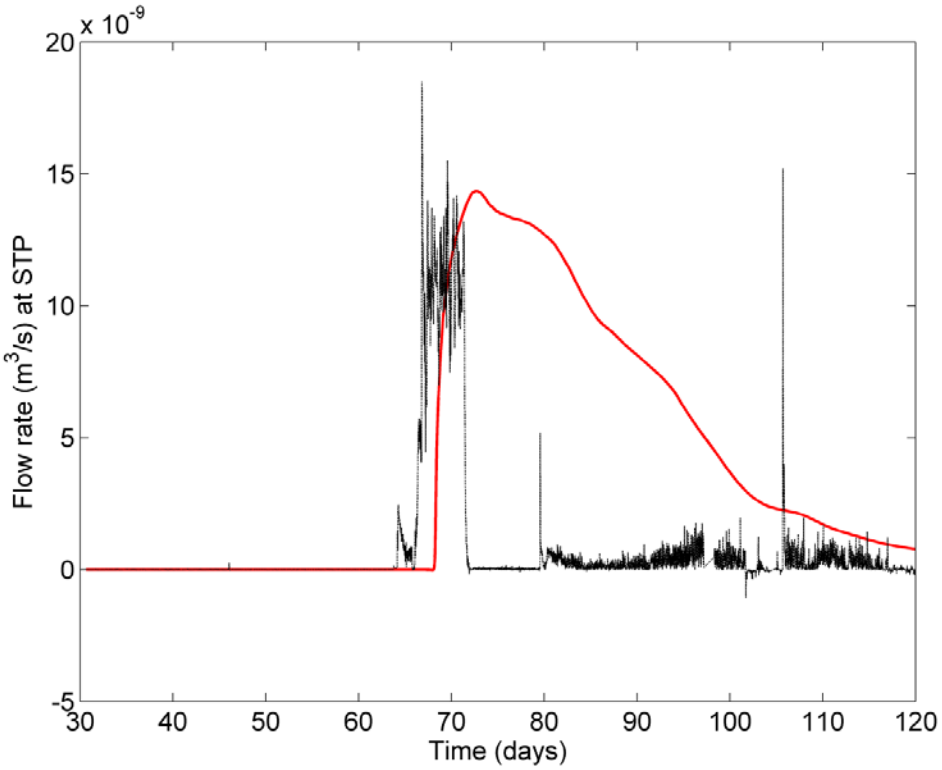

Figure 6-18. Comparison of simulated gas flow rate (red line) with experimental data (black line).

Figure 6-19 presents snapshots of the fracture pattern and the pore pressure contour during the breakthrough. The fractures initiate from the injection boundary and propagate into the sample. In the early stage with relatively low injection pressure, Figure 6-19a presents the fracture paths selectively activated to make distinct flow pathways. As shown in Figures 6-19b and c, with higher injection pressure, the whole cross section is somewhat uniformly fractured to enhance the gas flow (i.e., 1D flow). Figure 6-19d shows the fracturing is accelerated on the upper side of the sample when the fractures reach the backpressure boundary. However, the pressurized zone does not closely follow the fractured zone until the whole cross section is fractured, shown in Figure 6-19e.

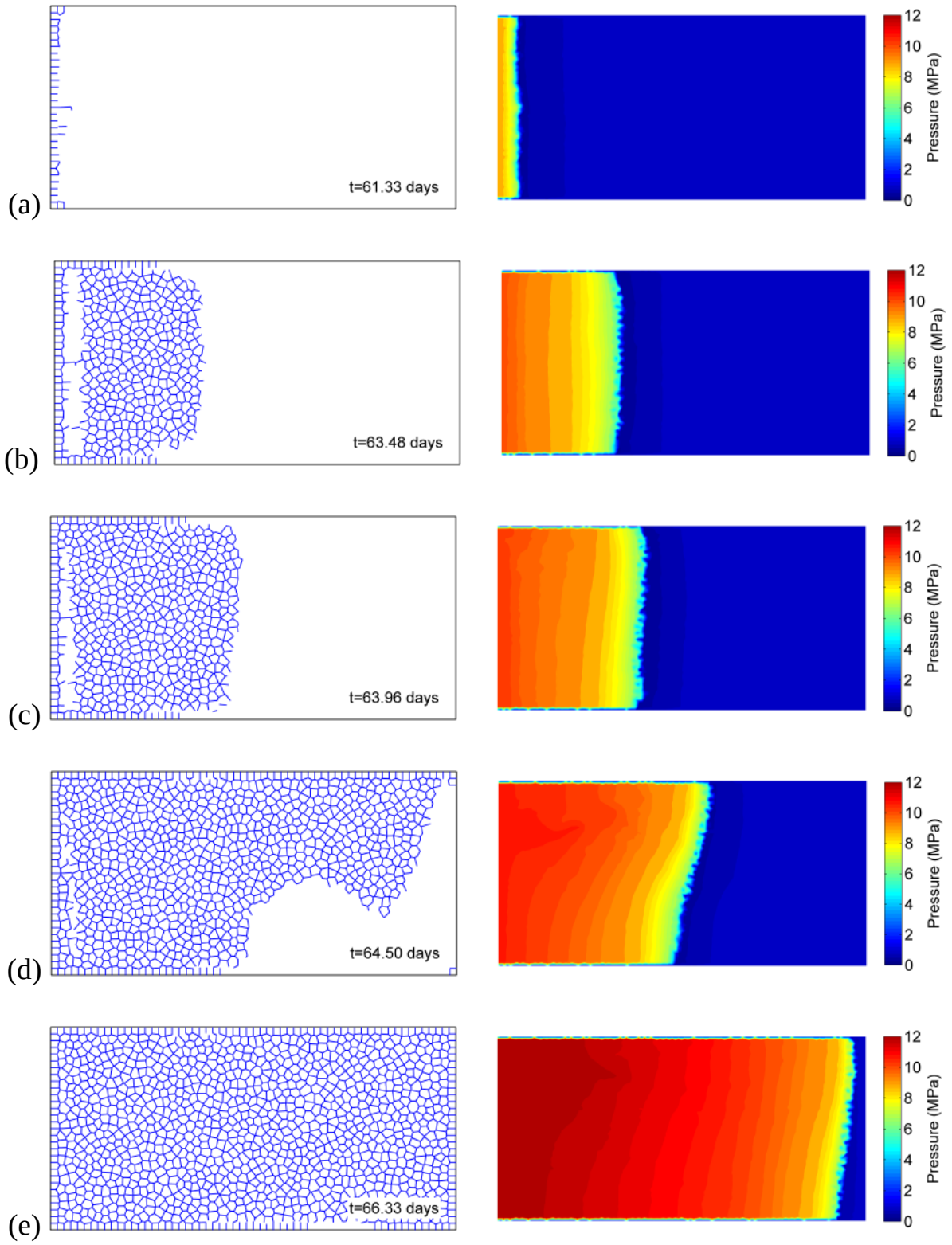

Figure 6-19. Snapshots of the mesh geometry, showing fracture patterns (left), and pressure contours (right) around the breakthrough.

6.6.2 Spherical flow through saturated bentonite under constant volume boundary conditions

For spherical flow modeling, we generated 3D Voronoi mesh of a cylinder with 120 mm height and 60 mm diameter (Figure 6-20), which is composed of 7,856 Voronoi cells and 33,316 lattice elements. Additional elements are added on the axial and circumferential surfaces to provide a constant volume boundary condition (zero-displacement constraints). Initial confinement with isotropic stress of 7.5 MPa is assumed in the sample as a mechanical condition, and the initial pore pressure of 1 MPa is given with fully saturated hydrological condition. While the padding elements surrounding the sample domain are constrained, 168 ml of gas (air) is injected into a boundary element with full gas saturation. A constant injection rate of 2.75×10^{-9} m^3/s at STP is maintained throughout the simulation. Elements at 12 locations on the circumferential surface of the sample, indicated by green marks in Figure 6-20a, are connected to the backpressure boundary element with a constant 1 MPa pressure. Outflow values are measured at the connections between those circumferential elements and the backpressure boundary element. Reactions are measured at the constrained padding elements to derive stress values at the load cells, which are colored in red in Figure 6-20b.

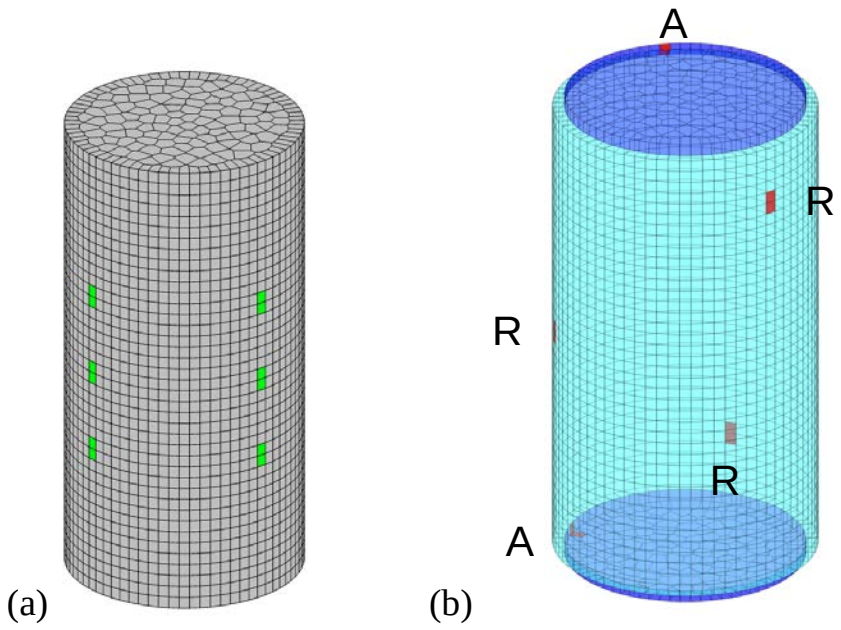

Figure 6-20. 3D Voronoi mesh generation: (a) Mesh discretization of bentonite domain. six Green marks (and six hidden on the other side) indicate the locations of porewater sensors for outflow measurement; and (b) Outer elements are padded for zero-displacement constraints. Red marks indicate the location of load cells, where the local stress values are measured.

The conceptual model is basically identical to the 1D gas flow model described in Section 6.5.1, except the scaling of the fracture capillary pressure. The fracture capillary pressure tends to decrease as the fracture aperture increases, so the water retention and air entry pressure in the fracture can be reduced. The water retention curve is defined using Equation (6.4). For a fracture element, the apparent gas entry pressure P'_0 of the element will be scaled by the permeability function given by

$$P'_0 = P_0 \left(\frac{k_0}{k}\right)^{1/3} \tag{6.10}$$

where k_0 is the intrinsic permeability (before fracturing), and k is the permeability of the fracture element.

Fundamental model parameters are kept as those given in Table 6-2. However, the residual gas saturation has changed to 0.0709, which corresponds to the air-entry pressure of 7 MPa. Pre-calibration for the compressibility of the injection boundary element has been performed to match the initial injection pressure development.

Figure 6-21 shows snapshots of fracture development during gas injection. Fractures are initiated at the center of the sample, where the gas injection occurs. Then, the main fracture cluster grows into a spherical shape toward the lateral surface of the sample. After the fracture cluster reaches the lateral surface, near-surface fractures propagate in the longitudinal direction. These non-uniform fracture patterns form heterogeneous enhanced permeability domain within the sample, where preferential flow paths would be generated.

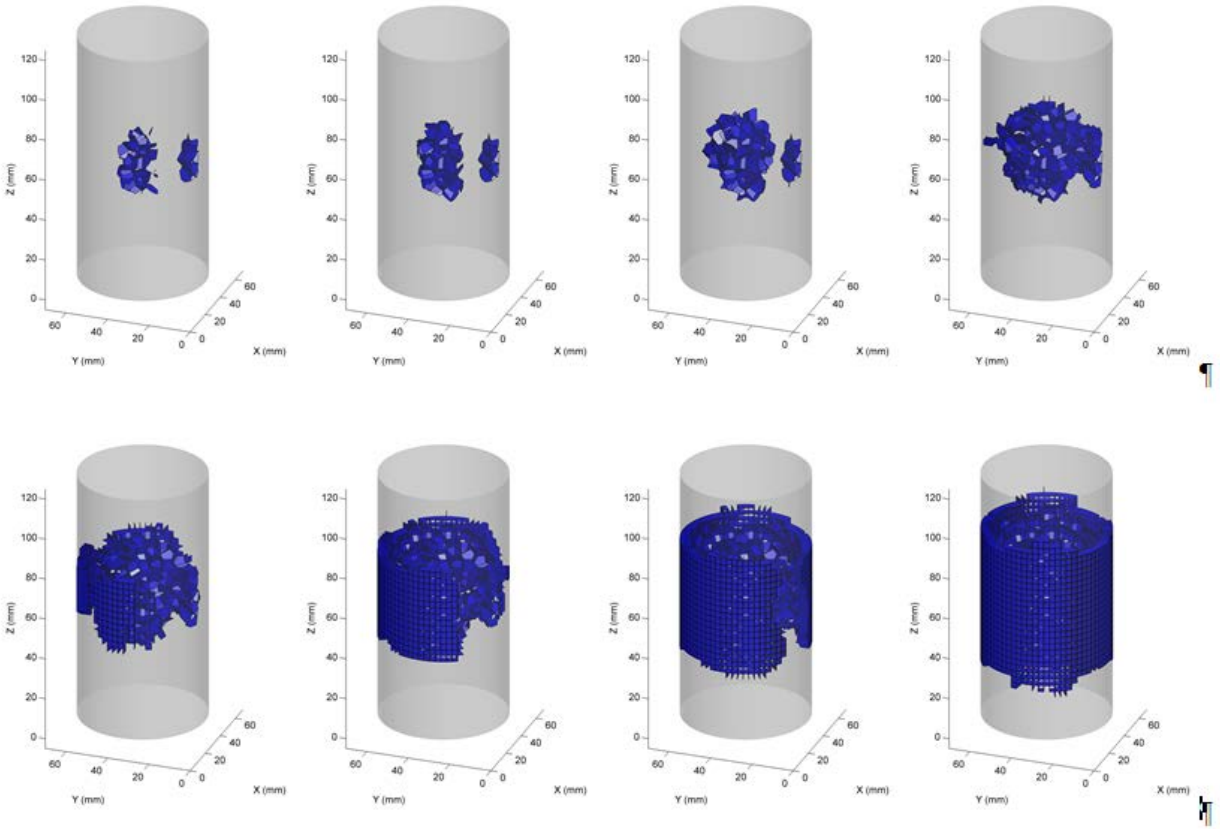

Figure 6-21. Non-uniform fracturing process development during gas injection.

Figure 6-22 presents the injection pressure evolution compared to the experimental result. With a constant injection rate, the pressure of the injection boundary element develops with a decent agreement with the experimental curve up to the peak, and the timing and the level of the peak pressure are comparable to the experimental results. However, the simulation does not demonstrate the recursive recovery and the pressure drop, which were observed in the experiment. Simulated pressure in the post-peak region shows similar trend of diminution and final pressure level compared to the pressure evolution in the experiment.

Figure 6-23 shows inflow rate to the sample and outflow rates through radial pore water arrays. Inflow rate was gradually increasing starting from about 744 days, when the initial gas entry occurred, and then around 758 days jumped to match the level of injection rate setting, which implies the gas breakthrough. About one day after the inflow rate jumped, the gas breakthrough affected the flow responses through radial pore water arrays. In the experiment, only one radial array took a dominant outflow in concordance with the inflow rate. However, contrary to the experimental observation, the simulation exhibits lower outflow rates for all three radial arrays. Multiple lower outflow rates with no dominant flow direction indicate that the inflow diverges to multiple outflows connected through the fractures.

Figure 6-24 shows the stress evolutions measured at the locations of load cells. Unlike the experimental results shown in Figure 6-24b, the simulated stresses in Figure 6-24a are maintained until the initial gas penetrated into the sample. The largest stress increase occurred at the radial load cell R2 placed in the middle of the sample, which is attributed to the closest distance from the injection location. The axial load cells, with the eccentric location from the center of the sample, do not gain as much stress increase as the load cell R2. Later, around 760 days, load cells R1 and R3 gain stress values as the fractures reach out to axial direction and the corresponding gas flow and pressure increase occurred.

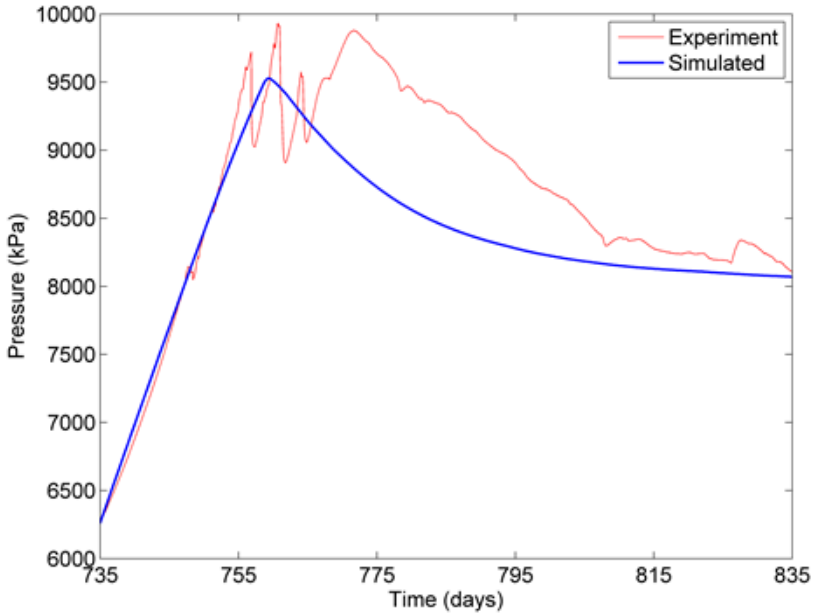

Figure 6-22. Comparison of simulated and experimental injection pressure evolutions.

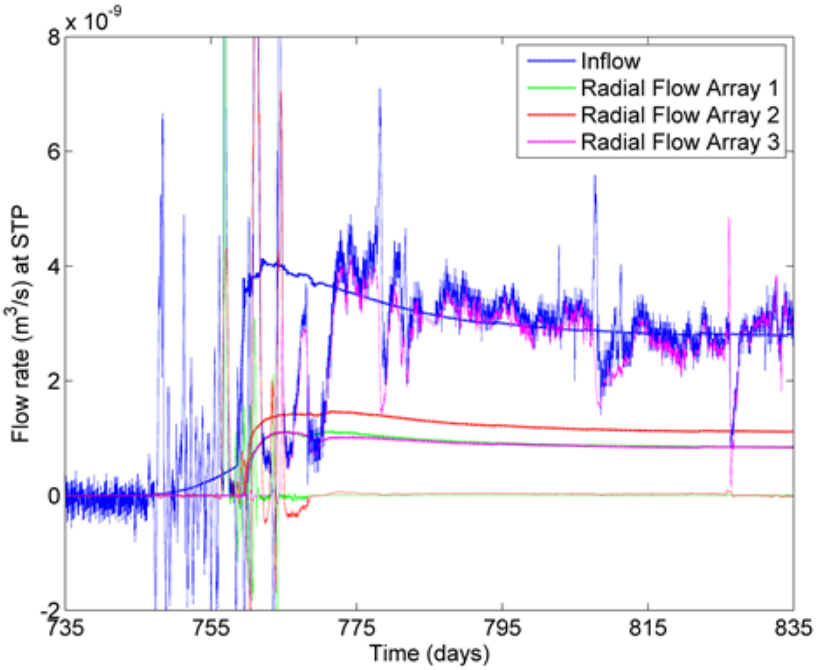

Figure 6-23. Comparison of simulated and experimental flow rate evolutions.

6.6.3 Summary of TOUGH-RBSN simulations for gas migration

For the 1D gas flow simulation, the DFN approach with enhanced fracture permeability demonstrated the gas breakthrough, where the pore pressure evolutions were matched well to the experimental data. The adoption of air entry pressure and swelling/shrinkage concepts helped simulate total stress evolutions in a decent accordance with the experimental results. However, the simulated outflow rate deviates from the experiment in terms of the flow activation time and the overall shape of the evolution curve.

The results of simulations of 3D spherical gas flow show the developed model captured some of key responses in gas pressure-induced fracturing processes. However, the current simulations are computationally very demanding, because the time step size becomes very small, especially during the fracturing stage. The capillary pressure values of fracture elements are varying depending on the fracture permeability (calculated using the cubic law based on the fracture aperture) for every time step, so some nonlinearity in the flow calculation hinders time marching with big strides. We expect to be able to retain the time step size using a constant scaling of capillary pressure values for the fractur elements.

For FY2019, we plan to continue to participate in the DECOVALEX-2019 Task A, with access to additional laboratory data for different types of geologic barrier materials. We will strive to resolve the convergence rate issues in the coupled multiphase flow simulations and find better and more efficient concepts and model parameters to demonstrate more realistic gas breakthrough features.

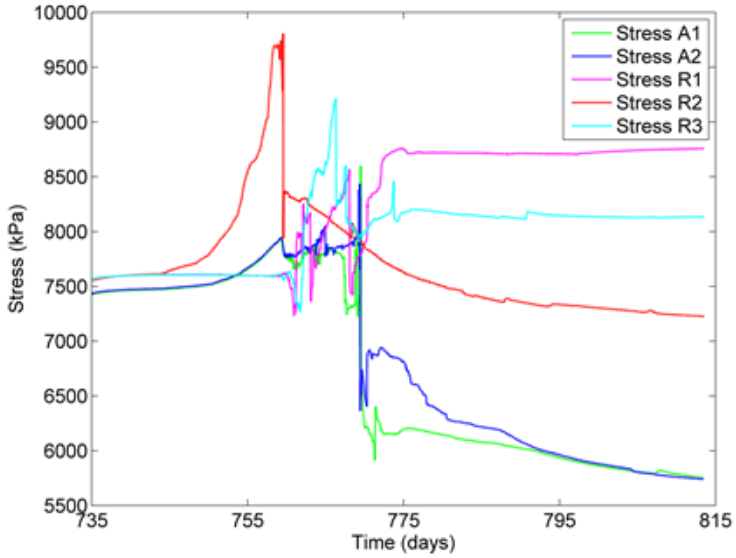

(a)

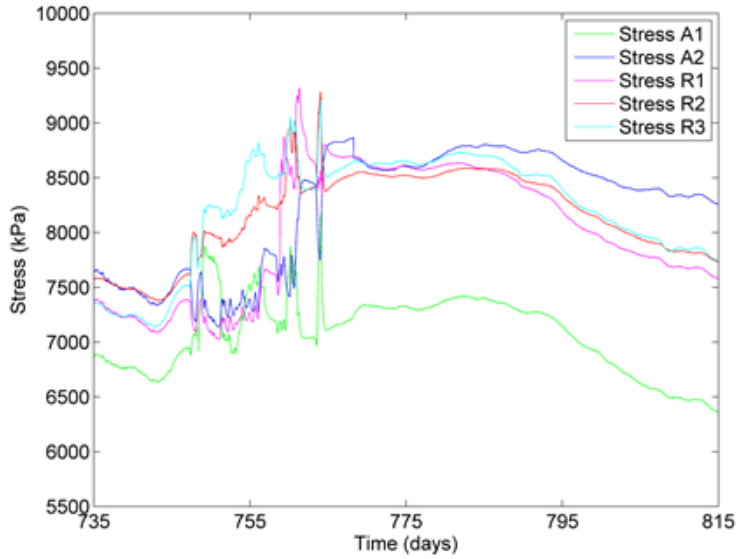

(b)

Figure 6-24. Comparison of (a) simulated stress evolutions, and (b) experimental stress data.

7. FAULT ACTIVATION MONITORING USING SIMFIP TOOL

7.1 Introduction

Faults of various sizes may be reactivated by thermal, hydraulic and mechanical disturbances during operational or post-closure periods. Observations suggest that remote earthquake waves can enhance basin-wide fluid transport extending to depths of a few kilometers. Understanding these phenomena has great importance for the design of geologic disposal of radioactive wastes, because the performance depends on the integrity of the natural system and barriers to contain radionuclides for tens of thousands of years. It is thus crucial that the permeability changes in response to earthquakes, specifically those occurring in fault zones and other preferential subsurface pathways such as the EDZ, can be better understood and eventually be predicted with confidence. LBNL has been developing a new instrument called Step-Rate Injection Method for Fracture *In-situ* Properties (SIMFIP) that may allow for probing the physical processes affecting fault reactivation in low permeability host rock layers at field scale. In parallel to instrument development, LBNL is being conducting *in situ* fault activation experiments at depths relevant to nuclear repository sites, using the SIMFIP to probe fault movements and to estimate fault permeability variations.

In this chapter, we first describe the current SIMFIP sensor developments that are conducted within the frame of this project. Second, through preliminary field test observations and numerical analyses, we explore how fault permeability can vary with slip and/or slip rate under pressurization in the range that could be expected in a host rock. Our results indicate that a good knowledge of the initial state of stress, permeability and friction parameters are key constituents to explore the hydraulic and mechanical response of a fault to a fluid pressurization. They also show that fault displacement rate might play a larger role than fault displacements in fault permeability variations, highlighting the importance of developing a sensor such as the SIMFIP sensor to track minor fault displacements, but at eventual high slip rate and their repeated effects on fault potential leakage in low permeable argillite host rock. Finally, we describe the perspectives to improve the SIMFIP ability to capture the fault displacements and pore pressure variations over a broad band of frequencies from 1 to 500Hz and in very low permeability rocks and to implement the physics of short-to-long term fault pressure and strain/strain rate evolution in numerical model(s) to predict fault permeability evolution in response to weak loadings by passing seismic waves.

7.2 Development of a New SIMFIP Sensor

The SIMFIP (Guglielmi et al., 2015a) technique combines the advantages of a stress relief method (because it allows constraining the full components of the stress tensor using a 6-component displacement sensor) with the advantages of a hydraulic or sleeve fracturing method (because the sensor is integrated in a straddle packer system which is easy to move downhole). Figure 7-1 shows a photograph of the SIMFIP tool just prior to deployment in a deep mine setting. Figure 7-2 shows a schematic representation of the SIMFIP tool, as well as a representative dataset from a real-world test.

The first SIMFIP instrument developed by Y. Guglielmi has been used for several research experiments in mine-based environments (Guglielmi et al., 2015b). In 2015, the SIMFIP allowed for the first direct in-situ continuous measurement of a field-scale fault transitioning from aseismic to seismic slip. Since 2017, further engineering of the SIMFIP performed at LBNL allowed for increasing the pressure conditions under which the SIMFIP can operate, and it is currently being tested in the deep Sanford Underground Research Facility (SURF), which is an underground research laboratory, within the framework of the EGS Collab SIGMA-V project (see Figure 7-1). The current state of development of the SIMFIP is at a TRL of 3-to-4. It has been tested in field boreholes in more than 20 tests at depths relevant to host rock

depository sites. Some tests were performed in argillite underground laboratory at Mont Terri (Switzerland) and Tournemire (France).

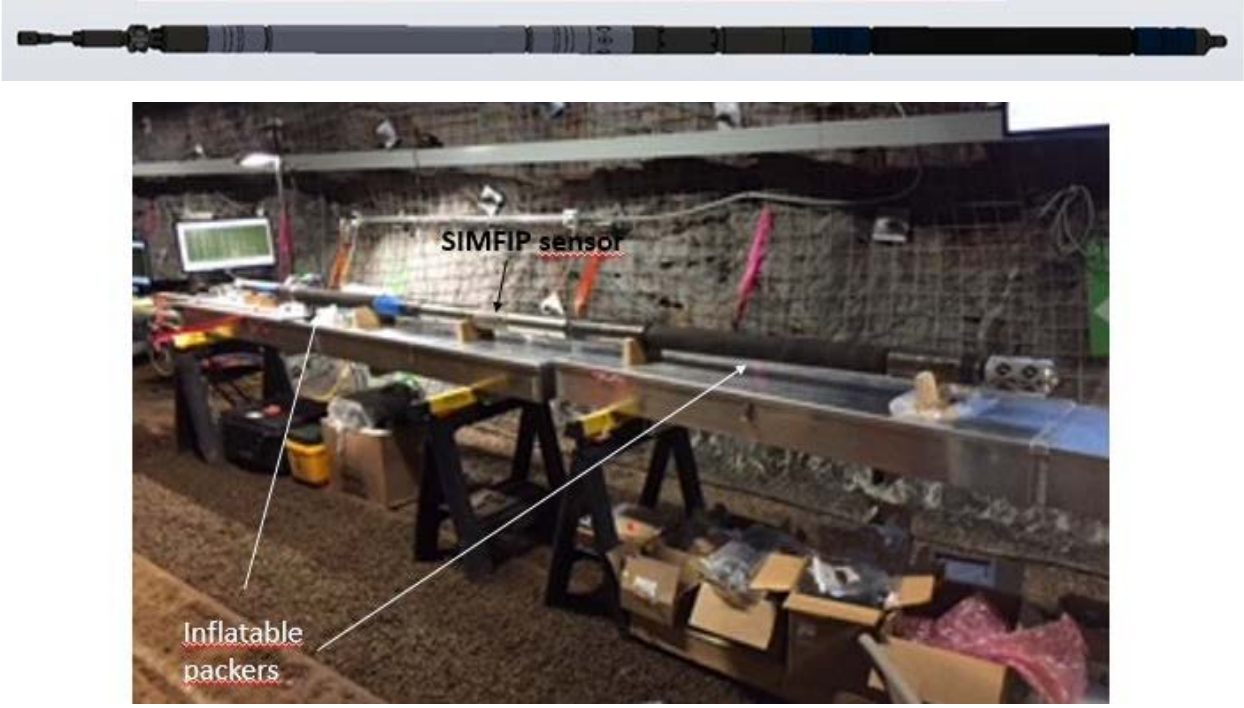

Figure 7-1. SIMFIP probe currently used for the fracture stimulation experiment in the SURF underground research laboratory (fracture pressure applied by the SIMFIP will be about 40MPa). Upper figure shows a Solid Works design of the SIMFIP and the photo shows the current SIMFIP probe.

The SIMFIP borehole probe allows for measuring simultaneously fluid pressure and three-dimensional displacements at high frequency (Figure 7-2). The injection interval is isolated in an open borehole using two inflatable rubber packers. The sealed interval length is currently of length 1.6 m, but can be varied to >20 m long by setting a chain of SIMFIP cages (Figure 7-3). Each SIMFIP cage is 0.2 m long and 0.1 m diameter pre-calibrated aluminum cage that can either: (Case 1) be connected to two 0.25 m long elements to allow for clamping both ends of the cage on borehole wall, or (Case 2) be directly connected to the packers. Dimensions of the SIMFIP cage can be varied depending on the target borehole conditions. In Case 1, when it is clamped, the cage is disconnected from the straddle packer system. In Case 2, the SIMFIP replaces the mandrel that connects the packers. When packers are inflated, they play two roles: (a) sealing the test interval, and (b) anchoring the SIMFIP cage. Case 2 is the simplest and easiest to set the SIMFIP probe, but the SIMFIP signal must be calibrated to account for the packers' effect during the test (this results in a relatively lower resolution of the SIMFIP signal in Case 2 compared to Case 1). Case 1 allows for a very high-resolution measurement.

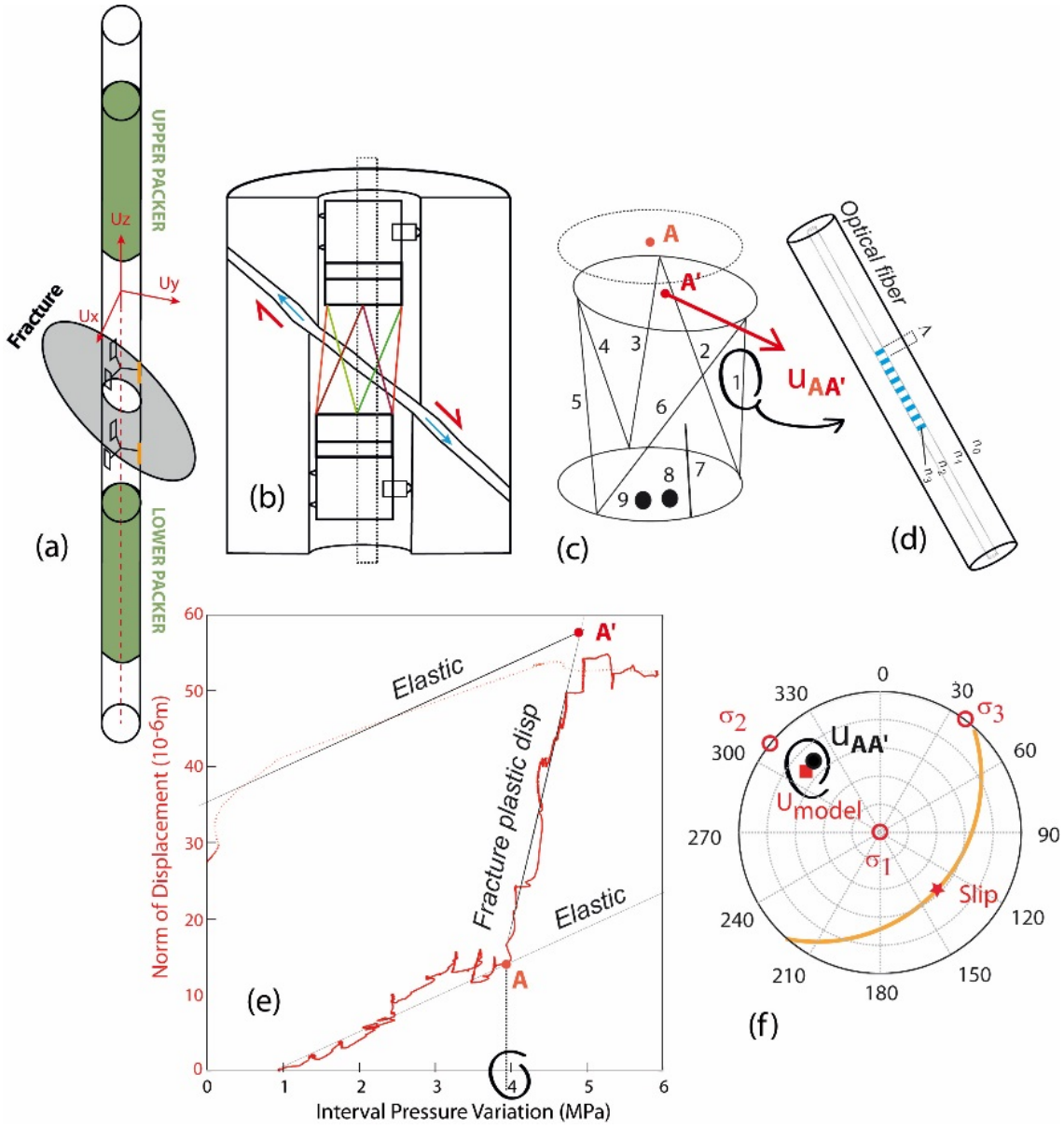

Figure 7-2. SIMFIP probe currently designed at LBNL: (a) Schematic typical SIMFIP setting across a natural fracture; (b) Details of the SIMFIP anchoring across the fracture; (c) Principles of the sensor which is a deforming cage in 6 different directions + 1 reference (7) + one pore pressure (8) + one temperature (9); (d) We build all our sensors using Bragg gages all connected on the same optical fiber; (e) Example of a fracture response to a pressure variation in the straddle packer interval, here showing the fracture plastic movement from A to A'; (f) Plastic displacement of the fracture's walls $U_{AA'}$ is plotted in a stereographic projection with the fracture plane orientation. Knowing both the fracture activation pressure and the three-dimensional plastic displacement allows a refined estimation of the absolute values of all the stress tensor components (including SH) by fitting a calculated vector with the measured one.

The SIMFIP is designed to capture micrometer to nanometer displacements of fractures affecting the borehole. In the case of a preexisting natural fracture the SIMFIP will be set across the fracture, anchored on either side of the fracture. A logging OPTV-type tool can be coupled to the SIMFIP probe to target the tested fracture interval in real-time. In the case of an induced fracture, the Case 2 configuration will be used to capture the orientation and the pressure at which the fracture grows from the borehole interval. In both cases, when the fracture is deforming according to the water pressure increase in the interval, the cage allows for obtaining angle dependent strain measurements, which are used to constrain the full three-dimensional strain tensor and the three rotations. The raw data are 6 strain measurements performed with optical fiber Bragg gratings (FBG) that are mechanically clamped on the 6 wings of the deforming cage. In addition, there is a reference FBG that is subject to ambient pressure and temperature, and which remains unstressed. It is used to correct linearly the strain measurements from temperature and pressure variations in the chamber. The 6+1 FBG are distributed along one single fiber that brings the sensor signals to an FBG interrogator set at the surface. A MicronOptics Si155 acquisition system is currently used. This interrogator allows picking shifts in the FBG wavelength that relate to FBG deformation over a large spectrum of FBG wavelengths.

The 6 components of the tensor describing the relative displacement and rotation between the upper and lower rings are calculated as a linear function of the 6 strain components (named A to F in Equation 7-1). The transfer matrix is calculated as the product of two 6 × 6 matrices calibrated in the laboratory: **A** converts strain data to efforts, i.e., forces and moments applied on the deforming body, and $\mathbf{C_0}$ converts these efforts to the translation and rotation components of the tensor, given by the following equation

$$\begin{pmatrix} u_x \\ u_y \\ u_z \\ r_x \\ r_y \\ r_z \end{pmatrix} = \mathbf{Co} \cdot \mathbf{A} \cdot \begin{pmatrix} A \\ B \\ C \\ D \\ E \\ F \end{pmatrix} \tag{7-1}$$

By convention, u_y corresponds to the axial strain, u_x and u_z to the radial strains. The variables r_x, r_y and r_z are the counter-clockwise rotations (right-hand convention) along the corresponding axes. The displacement range is 0.7 and 3.5 mm in the axial and radial directions of the borehole, respectively; the current accuracy is ± 0.1×10^{-6} m. A compass set on the probe provides the orientation of measurements with a 0.1° accuracy. The strain data are logged together with pump parameters (pressure and flow rate); water pressure in the anchoring hydraulics and water pressure in the packer hydraulics are measured at the surface. Temperature and pressure are measured in the borehole above, between, and below the packers using specially designed pressure and temperature sensors, which are also based on FBG technology. The chamber P/T sensors are run on the same fiber as the SIMFIP strains. The upper and lower P/T sensors are run on a second independent optical fiber. Ranges can be adapted depending on the depth of tests.

During the tests, the injection pressure is imposed by the pump, while flowrate, pressure, temperature and displacement variations from the SIMFIP probe are continuously monitored at a 1000 Hz sampling frequency. Raw data are saved into one ASCII file every five minutes. Pre-processing of the SIMFIP raw data is automated in the acquisition software (written in the LabView format), including the following steps: (1) correction of fiber Bragg gauges measurements from temperature and pressure, (2) detection of

the FBG spectra overlapping problems (and filtering), and (3) filtering from outliers using a medium filter (outliers can occur when the interrogator cannot calculate the FBG wavelength because of some wavelength heterogeneity in the assigned FBG spectral region).

7.3 Observations of fault permeability variations induced by pore pressure increase

Here we show observations from a controlled fault activation experiment conducted in the Mont Terri underground laboratory (Switzerland), affecting the Opalinus clay layer. One of the goals of this experiment was to apply the SIMFIP sensor to monitor a slip pulse propagation between an injection and a monitoring vertical borehole, both drilled about 5m away across the fault. The Fault "core" consists of a thrust zone about 0.8 to 3 m wide, which is bounded by two major fault planes. At the depth of the experiment, the upper fault boundary plane is oriented N050° and dipping 60°SE and the lower boundary plane is oriented N050° and dipping 40°SE (Figure 7-3). The detailed fracture structures visible on cores, and the strain intensity within the core zone of the Main Fault, are clearly heterogeneous, including zones with fault gouge, C'-type shear bands, meso-scale folds, microfolds, numerous fault planes and apparently undisturbed parts. Parts of the Main Fault comprise a 'scaly' fabric, where the rock splits progressively into smaller fish-like flakes. The different sets of faults in the Main Fault can be interpreted as Riedel P- and R-shears. The very low fault permeability determined before activation is ~10^{-17} m^2, which is close to the permeability of the host rock. State of stress estimated in and around the fault is characterized by a normal regime with the maximum principal stress σ_1 = 5.3±0.2 MPa sub-vertical, σ_2 = 4.5±0.2 MPa sub-horizontal, and striking N310±10° and σ_3 = 3.8±0.2 MPa sub-horizontal and striking N040±10°E (Figure 7-3).

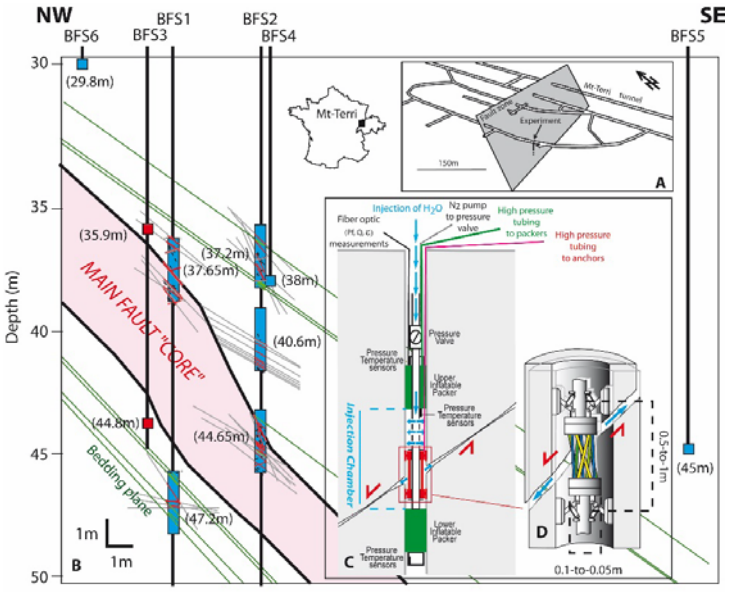

Figure 7-3. Schematic of the Mt Terri Main Fault activation experiment setting. A – Location of the experiment in vertical boreholes intersecting the Main Fault Zone, which is shown as a grey plane cross-cutting the Mt-Terri galleries. B – Vertical cross section perpendicular to the fault, showing the SIMFIP pressurization intervals as blue rectangles. C and D – Schematic of the SIMFIP probe and sensor used for these tests.

In Figure 7-4, we are presenting the graphs depicting the permeability change during repeated pressure pulses conducted at the interval located 40.6 m below the galleries (see Figure 7-3(A) for location). The upper red and blue curves show the imposed step-by-step pressure variations. Red segments of the pressure curve correspond to time intervals of the pressure increase in the borehole. Blue segments of the pressure curve correspond to the transient pressure evolution caused by the fault hydromechanical response after the pressure was increased in the test interval. Green segments show the fault displacement rate variations measured by the SIMFIP sensor (here it is the rate of the total displacement vector, which was continuously monitored by the SIMFIP during the test). For comparison, the lower graph shows the fault permeability variations obtained from fully coupled hydromechanical modeling with the TOUGH-FLAC simulator.

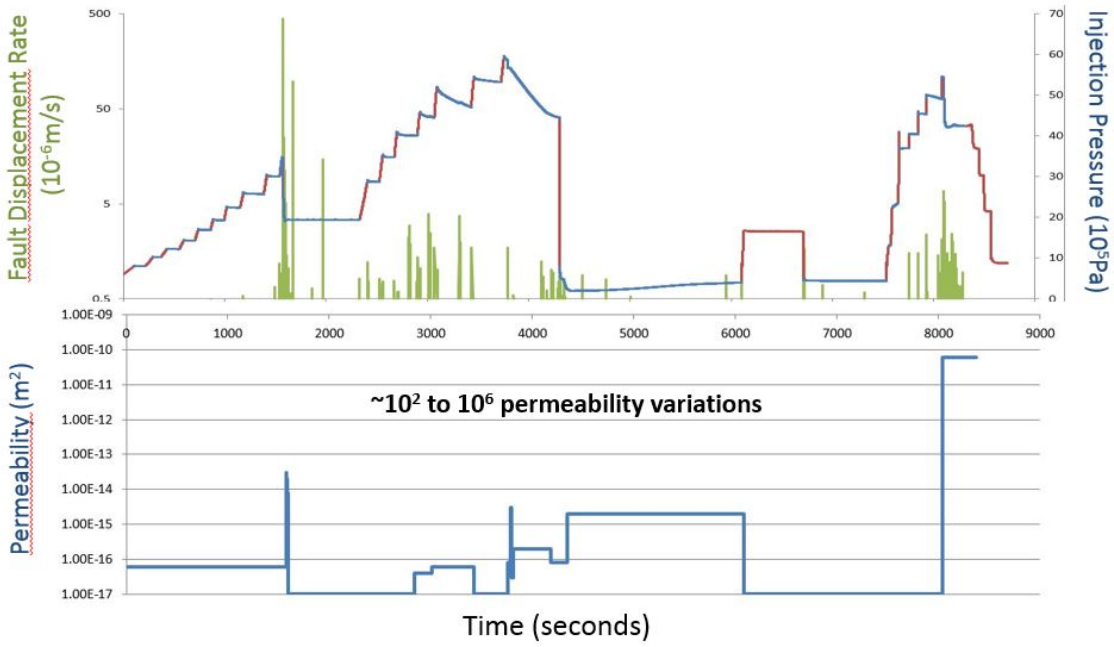

Figure 7-4. Upper graph – pressure (red and blue) and fault displacement rate (green) monitored during pressurization tests in the interval 40.2 m. Lower graph – interval permeability estimated from the fully coupled modeling of the pressure using the TOUGH-FLAC simulator.

Comparison of the upper and lower graphs shows that the large permeability variations correlate with periods of large slip rate events at 1500, 3800 and 8000 seconds, respectively. Interestingly, these permeability changes do not match well with the pressure imposed in the interval. Indeed, the 1500-second event is associated to a factor of 10 larger permeability change than the 3800-second one, although it occurs at a fault opening pressure about 2 MPa lower. This observation reveals that a relatively small pressurization associated with a high displacement rate might produce a larger permeability variation than a high pressurization associated to a small displacement rate. Thus, fault displacement rate might cause the effect of stress on fault reactivation and leakage. This observation also shows that the continuous fault displacement monitored by the SIMFIP sensor allows for tracking changes in faults displacement rates as potential precursors to “large” fault leaks (for simplicity we only show here the displacement rates, which are derived from the SIMFIP measured displacements).

7.4 Numerical analysis of key parameters conditioning fault activation induced by pore pressure increase

To investigate the coupling between fault permeability enhancement and slip or slip rate during fluid pressurization, we use the 3DEC code (Itasca Consulting Group, 2016), a distinct element method (Cundall, 1988) to simulate the interaction between fluid flow and fault slip evolution, including hydromechanical coupling, effective stress and friction. To describe the relationship between the fluid pressure diffusion and the permeability change with the fault normal displacement, the model uses the cubic law (Witherspoon et al., 1980). The method has been previously used to understand the hydromechanical behavior of fractured rock and fault zones during fluid pressurization (Cappa et al., 2006; Guglielmi et al., 2008), and to show that the evolution of the fault hydraulic diffusivity is a fully coupled problem depending on stress and fluid pressure (Guglielmi et al., 2015b).

Our 2D model (200 m × 50 m) considers a fluid injection into a horizontal flat fault in homogeneous elastic and impervious media (Figure 7-5a). The remote normal (σ_n) and shear stress (τ) resolved on the fault plane are constant. During injection, the fluid pressure is increased into the fault step-by-step of 0.5 MPa every 150 seconds at a point-source (Figure 7-5b). The total time of injection is 1050 seconds. For numerical accuracy, we used the fine mesh size (0.15 m) along the fault, which was gradually increased to 0.5 m in the direction normal to the fault toward model boundaries.

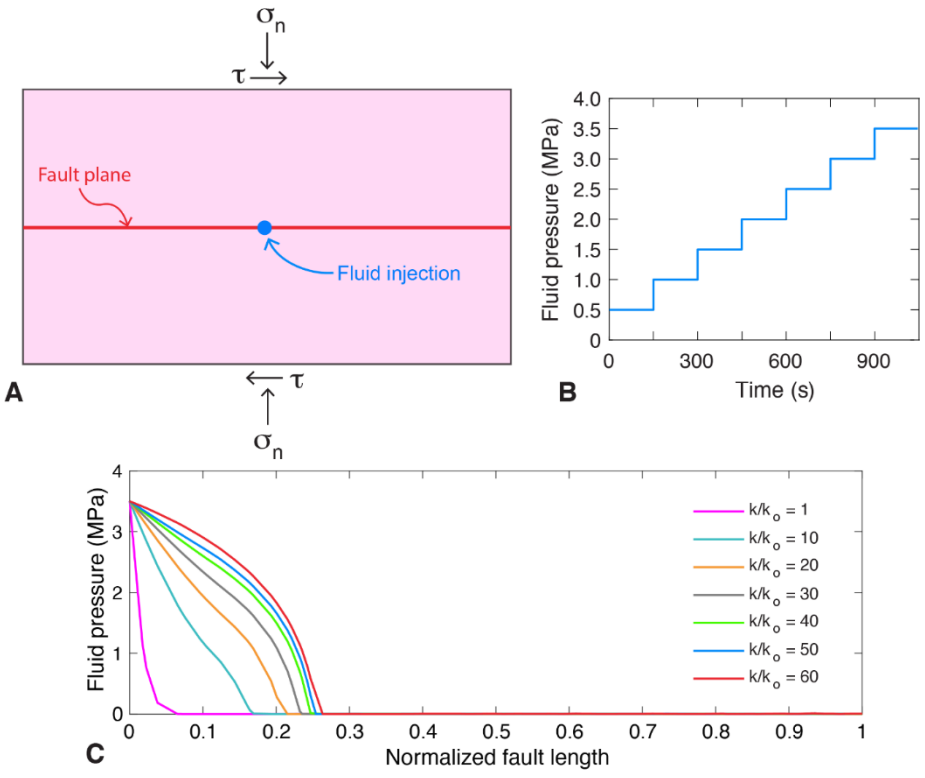

Figure 7-5. (a) Model geometry, and (b) graph of the simulated step-by-step pressure increase into the fault. The remote normal (σ_n) and shear stress (τ) resolved on the fault plane are constant, (c) half-profiles of fluid pressure calculated along the fault, assuming different permeability ratios (k/k_o). The injection point is located at $x = 0$ along the horizontal axis x representing the distance along fault. Half-profiles are plotted at the end of injection scenario (1050 seconds in Figure 7-4).

In these preliminary tests, we considered the following initial values of the normal stress and the fluid pressure into the fault: σ_{no} = 4.25 MPa and p_o = 0 MPa. We used two different values of shear stress τ_o = 1.65 and 2 MPa to evaluate the effects of different levels of fault criticality to failure, σ_{no}/τ_o = 0.388 and 0.47, respectively. We have tested the effects of different values of permeability changes with fault displacements k/k_o = 1, 10, 20, 30, 40, 50, and 60. The initial hydraulic aperture was assumed to be 9.15 microns (corresponding $k = 7 \times 10^{-12}$ m^2 calculated from the cubic law). Rock elastic properties are K = 20 GPa for the bulk modulus and G = 9 GPa for the shear modulus (more realistic argillite properties will be considered in furter numerical simulations).

Here, we have tested constant friction and rate-and-state friction (Marone, 1998). For a rate-and-state fault, we assumed the following frictional parameters: μ_o = 0.6, (a-b) = -0.002, and d_c = 10 microns. μ_o is the friction coefficient at a reference slip velocity. The parameter a quantifies the direct effect of a change in slip velocity. The parameter b describes the effect of the state variable (here, we use the "aging law" (Dieterich, 1979)). The characteristic slip distance, d_c, governs the evolution of the state variable. For the fault model with a constant friction, we assume a static value (μ_s) of 0.6. For simplicity, shear-induced dilatancy is neglected in the simulations.

The modeling results shown in Figure 7-5c revealed that the development of the fluid pressure along the fault varies as a function of different permeability enhancement. Modeling results indicate that both the magnitude and distribution of the steady-state overpressure, as well as the size of the pressurized area, depend on the permeability change. For constant permeability, the pressure perturbation is less pronounced, and the highest pressure and sharpest pressure gradients are situated near the pressurization point. For the modeling scenario with evolving permeability, the pressurization produces a reduction in effective normal stress by increasing the fluid pressure, which leads to opening the fault and increasing its permeability. The size of the pressurized zone is growing significantly with the fault permeability enhancement. Modeling results show that higher the permeability increase, the greater the pressurized area is (Figure 7-5c).

Then, we investigated the effects of the fluid pressure development on the size of the slip zone, and its dependency on the background stress and fault parameters (Figure 7-6). During the fluid pressurization along the fault, the reduction in frictional resistance to sliding, in the presence of a background fault-resolved shear stress, drives the growth of slip. Here, we modeled an aseismic slip (i.e., slow slip without dynamic effects). In Figure 7-6, we compared the slip length as a function of the length of the pressurized zone for a representative range of stress ratio (τ_o/σ_{no}), friction laws and permeability evolution (k/k_o). We found that the slip growth is controlled by a combination of the background stress, frictional weakening and permeability enhancement. For example, a fault with higher background stress and larger enhanced permeability can produce larger slip growth. The background stress affects both the timing of the onset of rupture and the subsequent size evolution of the slip area (Figure 7-6a). Reducing the shear stress delays the onset of rupture and decreases the maximal size of the slip area, whereas the increased shear stress leads to the earlier onset and a larger slipping zone. The effect of the fault friction is also illustrated in Figure 7-6a. Fault frictional weakening using the rate-and-state friction law influences the temporal evolution of the slipping area and may produce larger ruptures. This is expected because friction weakening leads to the reduced fault strength with sequences of accelerated and increased slip, while constant friction tends to stabilize the fault strength, resulting in a less pronounced slip.

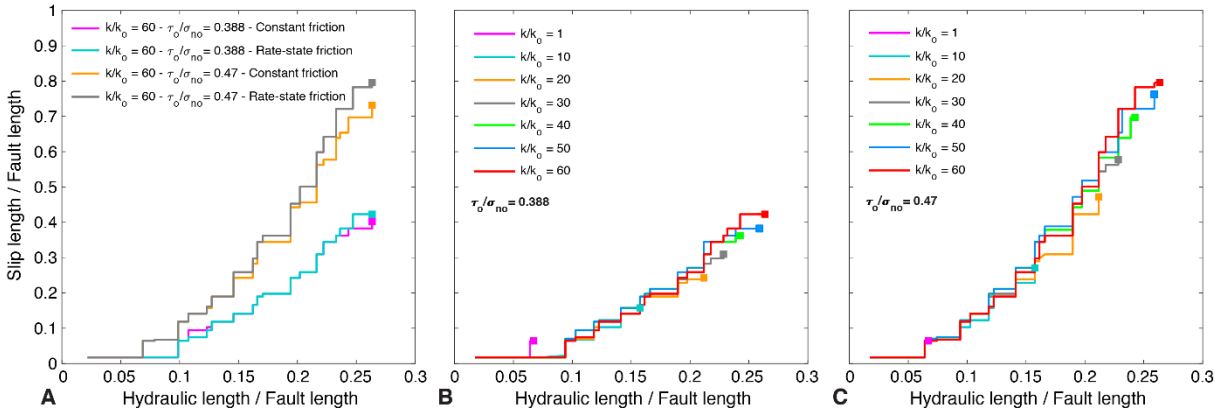

Figure 7-6. Influence of stress conditions and fault-related frictional and hydraulic parameters on the evolution of fault slip. Slip length as function of the hydraulic length for different (a) initial stress ratios and friction laws (i.e., constant friction, rate-and-state friction), and changes in fault permeability for two different stress regimes, (b) τ_o/σ_{no} = 0.388 and (c) τ_o/σ_{no} = 0.47, respectively.

Modeling results also indicate that the permeability evolution affects the spatial extent of the fluid overpressure on the fault, and the fault resistance to rupture; hence, it affects both the maximum diffusion length and the size of slip zone (Figures 7-6b and c). All simulation results, including permeability changes $k/k_o > 1$, show that the growth of the fault slip outpaces the growing fluid pressure front. Higher the increase in fault permeability, higher the growth of the slip front is. In addition, the most noticeable difference between the slip and pressure fronts occurs for the higher, more critical, initial stress ratio τ_o/σ_{no} = 0.47.

In summary, the initial stress on the fault and the change in fault permeability have an important impact on fault slip, which can occur over a zone much greater than the fluid-pressurized zone. For instance, the size of the slip zone is about 1.74 and 3.23 times greater than the size of the pressurized dilatant zone, respectively, for an initial stress ratio of 0.388 and 0.47, respectively (Figure 7-7). Thus, in addition to the fault frictional weakening, the size of the slip zone is controlled by the integral effect of the spatial extent of fluid pressure on the fault. The spatial extent of the largest slip increases with the spatial extent of the largest fluid pressure.

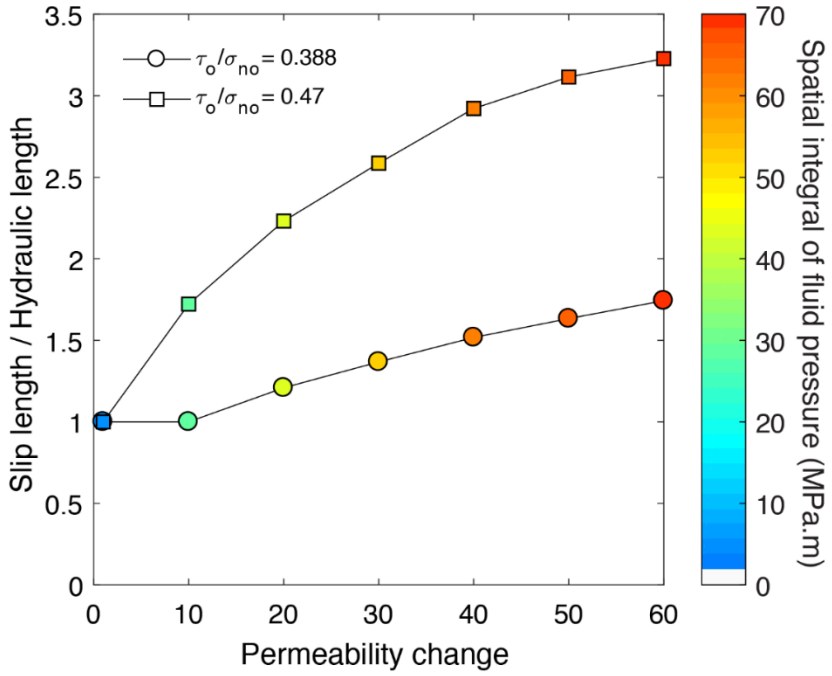

Figure 7-7. Graphs of the maximum slip length over maximum hydraulic length as a function of permeability enhancement. The color bar shows the spatial integral of fluid pressure computed at the end of injection.

7.5 Summary and future work on fault activation monitoring and SIMFIP tool

7.5.1 Upgrading the SIMFIP to detect nanoscale fault movements

In the next steps, we plan to increase the resolution of SIMFIP to nanometer accuracy over a broad band of frequencies [0 - 500Hz]. This will allow for capturing dynamic stress variations remotely from the borehole, ranging from below seismic detection to conventional seismic. Further engineering of the SIMFIP will focus on:

- Upgrading the SIMFIP resolution and accuracy to the nanostrain. This will be done by (i) engineering very high-resolution clamping systems to optimally bite the borehole wall, and (ii) testing different types of FBG sensors geometries from longer uniform FBG to more complex systems, such as Fabbry-Perot cavity based on FBG sensors, (iii) refining the SIMFIP cage design in order to make an ultra-compliant, and (iv) testing more advanced spectrometers based on the Stationary-Wave Integrated Fourier-Transform.
- Designing and testing different SIMFIP configurations including several SIMFIP cages in long intervals and configure a SIMFIP as a permanent long term monitoring sensor (instead of the current probe setting). We target testing >20 m long chains of SIMFIP that could simultaneously

probe the full stress tensor at relevant host rock scales, allowing monitoring three-dimensional displacements across a canister spacing or across a plurimeter thick fault or damage zone.

- Calibrating the SIMFIP to a broader band static to perform seismic stress monitoring. This is currently conducted by upgrading our existing calibration bench in the LBNL's laboratory that allows for applying to the SIMFIP probes both known forces and displacements in multiple directions. Current bench resolution is 0.05 mm and 100 Pa for displacements and stresses, respectively. We will (i) add more sensors to better characterize the coupling between SIMFIP and bench displacements, (ii) add accelerometers to characterize bench vibrations, and (iii) add hydraulic piston to produce computer controlled seismic waves in a [1, 10 Hz] frequency range.

7.5.2 Future *in situ* testing at Mt Terri (Switzerland) and Improvements in fault permeability constitutive laws in argillite

Our field observations and numerical results show that the initial stress on a fault, affecting the change in permeability and friction during a fluid pressurization directly into a fault, has an important effect on the fluid pressure diffusion and slip growth. Thus, our results indicate that a good knowledge of the initial state of stress, permeability and friction parameters are key requirements to explore the hydraulic and mechanical response of a fault to a fluid pressurization. In addition, we have shown that the fault deformation affects a volume largely greater than the volume pressurized by fluids. These results show that the new developments of friction with hydro-mechanical coupling made in the 3DEC code can be used for simulating the fault response to a fluid pressurization in argillite.

Next steps will include the initiation of a new fault activation experiment at Mont Terri. We plan to distribute sensors both close to the point of pressure variation and several meters apart from the pressure source in order to obtain a good spatial coverage of fluid pressure and deformation, and, hence, the estimation of the volume affected by the long-term permeability and stress changes. This experiment called FS-B should start in July 2018. In parallel, future numerical model improvements will include inelastic shear-induced dilatancy. We plan to use our improved numerical code to study a real dataset of fluid pressure and fault motion measurements, geology, rock properties, etc. collected during the FS-experiment at Mont Terri in order to improve our understanding of both the long-term permeability and stress changes in a fault zone in an argillite host rock.

This page intentionally left blank.

8. SUMMARY OF FY2018 PROGRESS AND FUTURE WORK

Here we summarize FY2018 progress and provide an outlook for the rest of FY2018 and future work planned for FY2019. First, in Section 8.1, we summarize in more detail the progress and plans of the ongoing argillite R&D and international activities. Thereafter, in Section 8.2, we present a summary of new activities for an expanded work scope and activities being launched as a result of new incremental FY2018 funding.

8.1 Progress and Plans of Ongoing FY2018 Activities

In FY2018 much work has been focused on modeling of the Mont Terri FE heater experiments in Opalinus clay and two *in situ* experiments at the Bure URL in COx claystone. Participating in these two international activities improved knowledge and provided data for model validation for two different clay types host rocks and for two different repository design concepts: the emplacement in horizontal tunnels (Swiss concept), and emplacement in micro-tunnels extended from the walls of larger tunnels (French concept). A comprehensive effort has also been dedicated to modeling of gas migration in bentonite, which is important to determine the fate of gas generated from metal corrosion of the waste package in a potential repository. In addition, new research has been launched on the evaluation of activation of faults and potential creation of flow paths through otherwise impermeable clay host rocks. Along with modeling these field and laboratory experiments, necessary model developments and improvements have been conducted.

1) Modeling of FE experiment at Mont Terri in Opalinus Clay

The Mont Terri experiment is unique because it is the only full-scale experiment in argillite, which involves natural resaturation of the bentonite buffer from the host rock (without artificial wetting). The experiment has been run with heating since the beginning of 2015 and the temperature at the heaters reached approaching 130°C. Modeling using TOUGH-FLAC of the first 3.5 years of heating has resulted in obtaining an excellent agreement between experimentally measured and simulated temperature and a good agreement between measured and simulated relative humidity (and saturation) in the buffer. The pattern of the buffer drying near the heaters was matched by assuming a reduced vapor diffusivity (the latter was calibrated by changing the tortuosity factor). In general, the buffer wetting caused by flow from the surrounding argillite rock is slow, and after 3.5 years, no substantial swelling stress has developed in the buffer. It will be very important to evaluate the mechanical behavior and a swelling stress in the buffer, as these are among the key functions of the buffer. In FY2019, we will continue modeling of the FE experiment along with new monitoring data, focusing more on the mechanical evolution of the buffer and host rock.

2) Modeling of heater experiments at Bure URL

Task E of the DECOVALEX-2019 project involves the evaluation of upscaling of THM properties and processes from laboratory-scale experiments, via *in situ* experiments, to a full repository scale. We have conducted coupled THM modeling following the task schedule of DECOVALEX-2019 along with other international modeling teams. The task also provides an opportunity to validate the software, TOUGH-FLAC, at a relevant field scale, in this case in COx clay stone. This year, we have made a good progress in modeling of two experiments with good agreement of addressing thermal pressurization. It is important to be able to accurately predict thermal pressurization and its impact on the stress field and potential for fracturing of the rock. A number of verification and validation steps have been completed and THM parameters of the COx claystone have been determined and validated. The next step to be conducted in FY2019 will be to model Step 4 of DECOVALEX-2019 Task E; that is, we will conduct model predictions at the repository scale of an area with several high level waste cells.

3) Modeling gas migration in bentonite

In FY2018, LBNL, as one of 11 international research teams, has continued to participate in DECOVALEX-2019 and conducted new simulations of gas flow through bentonite, and the results of simulations were compared with experimental data. Using two modeling approaches—continuum modeling (TOUGH-FLAC) and discrete fracture modeling (TOUGH-RBSN)—a good agreement was achieved with the results of the one-dimensional flow experiment, though not perfect regarding flow rate evolution. In FY2018, we also conducted a preliminary analysis of a spherical gas flow experiment using TOUGH-RBSN with a network for flow channels created from the injection point. Despite of a number of challenging problems involved in modeling of gas migration in bentonite, a good agreement between simulated and experimental data regarding the pressure and flow was achieved, although the internal micro-scale processes are not well known. In FY2019, we will continue modeling experiments related to the DECOVALEX-2019 tasks with comparison to experimental data and results of other modeling teams.

4) Fault activation monitoring using SIMFIP tool

We are leveraging on research and development at LBNL of a specialized borehole tool call SIMFIP. The SIMFIP tool allows for probing the physics of fault reactivation in low permeability host rock layers at the field scale. In parallel to the instrument development, LBNL is conducting *in situ* fault activation experiments at depths relevant to nuclear repository sites, using the SIMFIP to probe fault movements and to estimate fault permeability variations. Our results indicate that a good knowledge of the initial state of stress, permeability and friction parameters are key ingredients to explore the hydraulic and mechanical response of a fault to a fluid pressurization. The results also show that the fault displacement rate might play a larger role than fault displacements in fault permeability variations, highlighting the importance of developing a sensor, such as the SIMFIP sensor, to track minor fault displacements, but at an ultimate high slip rate and their repeated effects on fault leakage in low permeability argillite host rock. New international field tests are planned for investigating long-term effects of fault slip, including long term sealing and healing after initial creation of a fluid path, as well as fault reactivation caused by distant seismic events. In FY2019, we plan to upgrade the SIMFIP tool to be able to detect nanoscale fault movements and continue the development of constitutive models for fault and fracture hydromechanical evolution in argillite host rock, along with modeling of new field experiments.

8.2 Expanded FY2018 Argillite Research Activities

The expanded Argillite Disposal R&D and Argillite International at LBNL will be focused on the following activities: (1) Coupled processes model development with GDSA integration, (2) Deployment of monitoring thermal pressurization during a heater experiment at ANDRA's URL in Bure, (3) Model testing and development for large scale gas driven fracturing, (4) participation in DECOVLAEX-2019 fault slip study, (5) Coupled microbial-abiotic processes in EBS and host rocks. These activities will be carried out for the rest of FY2018 (June-September 2018) and will continue in FY2019. The relevance of these new activities, as an expansion of LBNL's existing work on coupled THM processes R&D in argillite, is illustrated in Figure 8-1. Issues related to gas generation and thermal pressurization are relevant for assessing the performance of the system, as to prevent new flow paths to form along the EDZ or across a low permeability clay host rock. Key questions include the faith of generated gas and the likelihood for creating such a flow path and the long-term evolution of such a flow path, including sealing and healing.

1) Model development and testing for GDSA Integration

This task involves a necessary model development and adaptation of TOUGH-FLAC for GDSA integration. We plan to upgrade to latest parallel version of FLAC3D and link it to TOUGH3, which is the newly released version of the TOUGH family codes. We will collaborate with Sandia National

Laboratories to evaluate how to integrate our work on near field coupled THM processes into their PFLORTRAN generic disposal simulations. This will involve practical applications of EDZ constitutive models with a need to develop EDZ models that can model long-term sealing and healing.

2) *In Situ* characterization of fracturing induced by thermal pressurization

The SIMFIP tool will be used for *in situ* characterization of a fracture induced by thermal pressurization at ANDRA's URL in Bure. This will be part of an *in situ* heating experiment in COx claystone aimed at studying potential fracturing induced by high fluid pressure during thermal pressurization. A borehole will be drill through the heated volume, and the SIMFIP tool will be used to characterize any effects of fracturing. Resulting changes in the complete strain tensors via the SIMFIP 6-component deformation cage coupled to changes in pore pressure will be inverted to characterize host rock within the heated zone. Characterizations will be conducted at different temperatures and analyzed using fully coupled THM models.

3) Model testing and development for large-scale gas driven fracturing

We will test and adapt 3D models for modeling large-scale (tens to hundreds of meters) fluid and gas driven discrete fracture propagation relevant to argillite disposal. We will evaluate existing discrete fracture modeling software, and/or other in-house options to decide the best approach to be adopted for high-performance computing (HPC) and visualization of 3D discrete fracture propagation in the field. We will model examples related to large-scale (hundreds of meters) 3D discrete gas driven fracture propagation from a repository tunnel located in argillite. This is again relevant to the potential impact of gas generation and its potential for creating a new flow path through initially impermeable host rock.

4) Participate in the DECOVALEX-2019, fault slip task

Scientists from LBNL are currently the technical leads of DECOVALEX-2019, Task B, related to modeling of fault activation experiments at Mont Terri, in Opalinus Clay, funded by the Swiss. As part of the expanded international collaboration, we will increase LBNL's involvement as a modeling team in this DECOVALEX-2019 task.

5) Coupled microbial-abiotic processes in EBS and host rocks

Preliminary laboratory and modeling investigations will be conducted to evaluate the role of coupled microbial-abiotic processes in host rock materials. Particular emphasis will be on processes driven by corrosion byproducts, including H_2 gas. The goal is to understand the role that these coupled microbial-abiotic processes have on controlling the fate of the corrosion byproducts and in inducing changes in the chemical and physical properties of the bentonite and host rock, which could alter future repository performance.

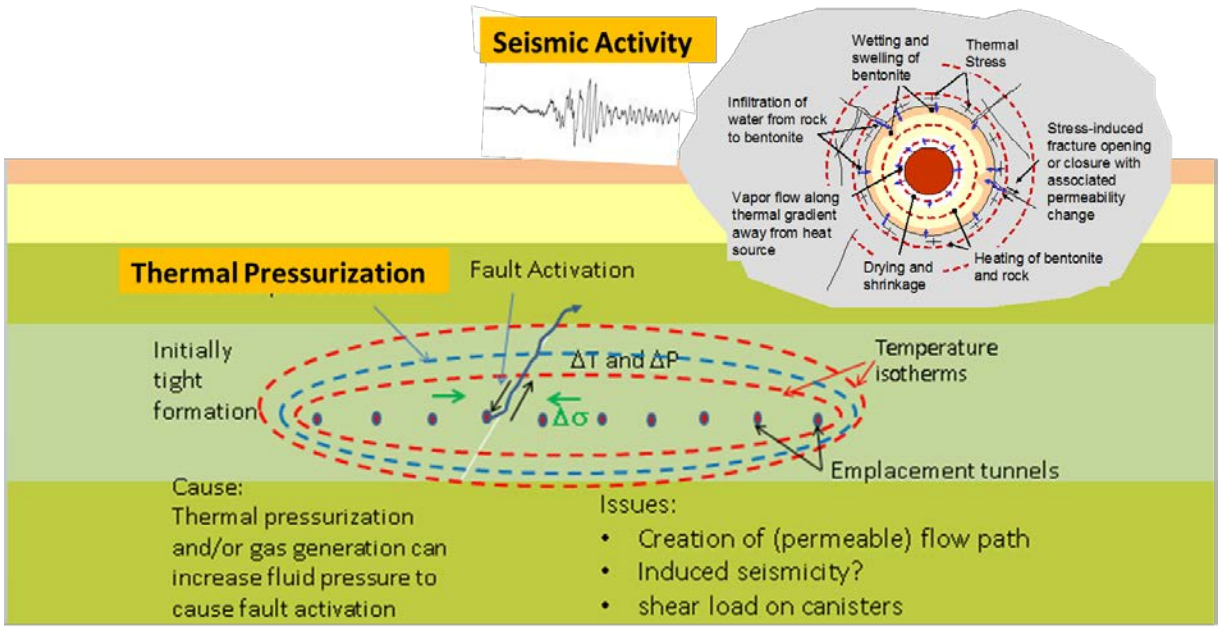

Figure 8-1. Schematic of coupled THM responses in a repository in the near field (upper right) and at the repository scale caused by heating, thermal pressurization and potential gas generation.

9. ACKNOWLEDGEMENTS

This work was supported by the Spent Fuel and Waste Science and Technology Campaign, Office of Nuclear Energy, of the U.S. Department of Energy under Contract Number DE-AC02-05CH11231 with Lawrence Berkeley National Laboratory.

This page intentionally left blank.

10. REFERENCES

Alonso, E.E., Gens, A., and Josa, A. (1990) A constitutive model for partially saturated soils. Geotechnique. 40: 405-430.

Asahina, D., and Bolander, J.E. (2011) Voronoi-based discretizations for fracture analysis of particulate materials, Powder Technology, 213, 92–99.

Asahina, D., Houseworth, J.E., Birkholzer, J.T., Rutqvist, J., and Bolander, J.E. (2014) Hydro-mechanical model for wetting/drying and fracture development in geomaterials, Computers & Geosciences, 65, 13–23.

Biot, M.A., and Willis, D.G. (1957) The elastic coefficients of the theory of consolidation, Journal of Applied Mechanics, 24, 594–601.

Bolander, J.E., and Saito, S. (1998) Fracture analyses using spring networks with random geometry, Eng. Fract. Mech., 61, 569–591.

Booker, J.R., and Savvidou, C. (1985) Consolidation around a point heat source. International Journal for Numerical and Analytical Methods in Geomechanics 9, 173–184.

Bossart, P., Meier, P.M, Moeri, A, Trick, T, and Mayor, J-C. (2002) Geological and hydraulic characterization of the excavation disturbed zone in the Opalinus Clay of the Mont Terri Rock Laboratory. Eng Geol 66, 19–38.

Bossart, P., Trick, T., Meier, P.M., and Mayor, J.-C. (2004) Structural and hydrogeological characterisation of the excavation-disturbed zone in the Opalinus Clay (Mont Terri Project, Switzerland), Applied Clay Science, 26, 429– 448.

Cappa, F., Guglielmi, Y., Rutqvist, J., Tsang, C-F., and Thoraval, A. (2006) Hydromechanical modeling of pulse tests that measure fluid pressure and fracture normal displacement at the Coaraze Laboratory site, France, Int. J. Rock Mech. Min. Sci., 43(7):1062-1082.

Chaboche, J.-L. (1992) Damage induced anisotropy: On the difficulties associated with the active/passive unilateral condition. International Journal of Damage Mechanics 1, 148–171.

Corkum, A.G., and Martin, CD. (2007) Modeling a mine-by test at the Mont Terri rock laboratory, Switzerland. International Journal of Rock Mechanics & Mining Sciences 44, 846–859.

Corey, A.T. (1954) The Interrelation Between Gas and Oil Relative Permeabilities, Producers Monthly, 38-41.

Cundall, P.A. (1988) Formulation of a three-dimensional distinct element model—Part I. A scheme to detect and represent contacts in a system composed of many polyhedral blocks. Int. J. Rock Mech. Min. Sci. Geomech. Abstr., 25:107-116.

Cuss, R.J., Harrington, J.F., Noy, D.J., Graham, C.C., and Sellin, P. (2014) Evidence of localised gas propagation pathways in a field-scale bentonite engineered barrier system; results from three gas injection tests in the Large scale gas injection test (Lasgit). Applied Clay Science, 102, pp.81-92, doi:10.1016/j.clay.2014.10.014Harrington J (2016) Specification for DECOVALEX-2019: Task A: modElliNg Gas INjection ExpERiments (ENGINEER). Ref: BGS-DX-v3.

Dieterich, J. H. (1979) Modeling of rock friction experimental results and constitutive equations, J. Geophys. Res., 84, 2161–2168, doi:10.1029/JB084iB05p02161.

Garitte, B., and Gens, A. (2012) TH and THM Scoping computations for the definition of an optimal instrumentation layout in the Full-scale Emplacement (FE) experiment NAGRA NIB 10-34, March 2012.

Garitte B., Shao H., Wang X.R., Nguyen T.S., Li Z., Rutqvist J., Birkholzer J., Wang W.Q., Kolditz O., Pan P.Z., Feng X.T., Lee C., Graupner B.J., Maekawa K., Manepally C., Dasgupta B., Stothoff S., Ofoegbu G., Fedors R., and Barnichon J.D. (2017) Evaluation of the predictive capability of coupled thermo-hydro-mechanical models for a heated bentonite/clay system (HE-E) in the Mont Terri Rock Laboratory. Environmental Earth Sciences, 76:64.

Gens, A., and Alonso, E. (1992) A framework for the behaviour of unsaturated expansive clays. Can. Geotech. J. 29, 1013–1032.

Gens, A., Sánchez, M., and Sheng, D. (2006) On constitutive modeling of unsaturated soils. Acta Geotechnica. 1, 137-147.

Gens, A., Sánchez, M., Guimaraes, L.D.N., Alonso, E.E., Lloret, A., Olivella, S., Villar, M.V., and Huertas, F. (2009) A full-scale *in situ* heating test for high-level nuclear waste disposal: observations, analysis and interpretation. Geotechnique 59, 377–399.

Guglielmi, Y., Cappa, F., Avouac, J.-P., Henry, P., and Elsworth, D. (2015a) Seismicity triggered by fluid injections induced aseismic slip, Science, 348(6240), 1224–1226, doi:10.1126/science.aab0476.

Guglielmi, Y., Elsworth, D., Cappa, F., Henry, P., Gout, C., Dick, P., and Durand, J. (2015b) In situ observations on the coupling between hydraulic diffusivity and displacements during fault reactivation in shales, J. Geophys. Res., 120, doi:10.1002/2015JB012158.

Harrington, J.F., and Horseman, S.T. (1999) Gas transport properties of clays and mudrocks. In: Muds And Mudstones: Physical And Fluid Flow Properties (eds A.C.Aplin, A.J. Fleet, and J.H.S. Macquaker). Geological Society of London, Special Publication No. 158, 107-124.

Harrington, J.F., Milodowski, A.E., Graham, C.C., Rushton, J.C., and Cuss, R.J. (2012) Evidence for gas-induced pathways in clay using a nanoparticle injection technique. Mineralogical Magazine. December 2012, Vol. 76(8), pp.3327-3336. DOI: 10.1180/minmag.2012.076.8.45.

Harrington, J. (2016) Specification for DECOVALEX-2019: Task A: modElliNg Gas INjection ExpERiments (ENGINEER). Ref: BGS-DX-v3.

Harrington, J.F., Graham, C.C., Cuss, R.J., and Norris, S. (2017) Gas network development in a precompacted bentonite experiment: Evidence of generation and evolution, Applied Clay Science, 147, 80–89.

Horseman, S.T., Harrington, J.F., and Sellin, P. (1999) Gas migration in clay barriers. Engineering Geology, Vol. 54, 139-149.

Horseman, S.T., Harrington, J.F., and Sellin, P. (2004) Water and gas flow in Mx80 bentonite buffer clay. In: Symposium on the Scientific Basis for Nuclear Waste Management XXVII (Kalmar), Materials Research Society, Vol. 807. 715-720.

Houseworth, J., Rutqvist, J., Asahina, D., Chen, F., Vilarrasa, V., Liu, H.H., and Birkholzer, J. (2013) Report on International Collaboration Involving the FE Heater and HG-A Tests at Mont Terri. Prepared for U.S. Department of Energy, Used Fuel Disposition Campaign, FCRD-UFD-2014-000002, Lawrence Berkeley National Laboratory.

International Formulation Committee (IFC) (1967) A Formulation of the Thermodynamic Properties of Ordinary Water Substance, IFC Secretariat, Düsseldorf, Germany.

Itasca, FLAC3D V5.0 (2011) Fast Lagrangian Analysis of Continua in 3 Dimensions, User's Guide. Itasca Consulting Group, Minneapolis, Minnesota.

Kawai, T. (1978) New discrete models and their application to seismic response analysis of structures, Nucl. Eng. Des., 48, 207–229.

Kim, K., and Lim, Y.M. (2011) Simulation of rate dependent fracture in concrete using an irregular lattice model, Cement & Concrete Composites, 33, 949–955.

Kim, K., Rutqvist, J., Nakagawa, S., and Birkholzer, J. (2017) TOUGH-RBSN simulator for hydraulic fracture propagation within fractured media: Model validations against laboratory experiments, Computers & Geosciences, 108, 72–85.

Kristensson, O., and Åkesson, M. (2008) Mechanical modeling of MX-80 – Quick tools for BBM parameter analysis. Phys Chem Earth, Parts A/B/C. 33, Supplement 1: S508-S515.

Liu, H.H., Houseworth, J., Rutqvist, J., Li, L., Asahina, D., Chen, F., and Birkholzer, J. (2012) Report on Modeling Coupled Processes in the Near Field of a Clay Repository. Prepared for U.S. Department of Energy, Used Fuel Disposition Campaign, FCRD-UFD-2012-000223, Lawrence Berkeley National Laboratory.

Marone, C. (1998) Laboratory-derived friction laws and their application to seismic faulting, Ann. Rev. Earth Planet. Sci., 26, 643–696.

Martin C.D., and Chandler N.A. (1994) The progressive fracture of Lac du Bonnet Granite. International Journal of Rock Mechanics and Mining Sciences & Geomechanics Abstract, 31, 643–59.

Martino, J.B., and Chandler, N.A. (2004) Excavation-induced studies at the Underground Research Laboratory. International Journal of Rock Mechanics and Mining Sciences, 41, 1413–26.

Nguyen, T.S., Börgesson, L., Chijimatsu, M., Hernelind, J., Jing, L., Kobayashi, A., and Rutqvist, J. (2009) A case study on the influence of THM coupling on the near field safety of a spent fuel repository in sparsely fractured granite. Environmental Geology, 57, 1239–1254.

Nutt, M. (2012) Used Fuel Disposition Campaign Disposal Research and Development Roadmap (FCRD-USED-2011-000065 REV1), U.S. DOE Used Fuel Disposition Campaign.

Okabe, A., Boots, B., Sugihara, K., and Chiu, S.N. (2000) Spatial Tessellations: Concepts and Applications of Voronoi Diagrams, 2nd ed., Wiley, NYC, 696 pages.

Pruess, K., Oldenburg, C.M., and Moridis, G. (2012) TOUGH2 User's Guide, Version 2.1, LBNL-43134(revised), Lawrence Berkeley National Laboratory, Berkeley, California.

Rutqvist, J., Noorishad, J., Tsang, C.-F., and Stephansson, O. (1998) Determination of fracture storativity in hard rocks using high-pressure injection testing, Water Resources Research, 34(10), 2551–2560.

Rutqvist, J., Tsang, C.-F., and Stephansson, O. (2000) Uncertainty in the maximum principal stress estimated from hydraulic fracturing measurements due to the presence of the induced fracture, International Journal of Rock Mechanics and Mining Sciences, 37, 107–120.

Rutqvist, J., Börgesson, L., Chijimatsu, M., Kobayashi, A., Nguyen, T. S., Jing, L., Noorishad, J., and Tsang, C.-F. (2001) Thermohydromechanics of partially saturated geological media – Governing equations and formulation of four finite element models. International Journal of Rock Mechanics and Mining Sciences, 38, 105-127. Rutqvist, J., Wu, Y.-S., Tsang, C.-F., and Bodvarsson, G. (2002). A modeling approach for analysis of coupled multiphase fluid flow, heat transfer and deformation in fractured porous rock. International Journal of Rock Mechanics & Mining Sciences, 39, 429-442.

Rutqvist, J., and Tsang, C.-F. (2002) A study of caprock hydromechanical changes associated with CO2-injection into a brine formation, Environmental Geology, 42, 296–305.

Rutqvist, J., Börgesson, L., Chijimatsu, M., Hernelind, J., Jing, L., Kobayashi, A., and Nguyen, S. (2009) Modeling of damage, permeability changes and pressure responses during excavation of the TSX tunnel in granitic rock at URL, Canada. Environmental Geology, 57, 1263–1274.Rutqvist, J. (2011) Status of the TOUGH-FLAC simulator and recent applications related to coupled fluid flow and crustal deformations. Computers & Geosciences, 37, 739–750.

Rutqvist, J., Ijiri, Y, and Yamamoto, H. (2011) Implementation of the Barcelona Basic Model into TOUGH-FLAC for simulations of the geomechanical behavior of unsaturated soils. Computers & Geosciences, 37, 751–762.Rutqvist, J., Ijiri, Y., and Yamamoto, H. (2011) Implementation of the Barcelona Basic Model into TOUGH-FLAC for simulations of the geomechanical behavior of unsaturated soils. Computers &Geosciences, 37, 751-762.

Rutqvist, J., Davis, J., Zheng, L., Vilarrasa, V., Houseworth, J., and Birkholzer, J. (2014a) Investigation of Coupled THMC Processes and Reactive Transport: FY14 Progress. Prepared for U.S. Department of Energy, Used Fuel Disposition, FCRD-UFD-2014-000497, Lawrence Berkeley National Laboratory, LBNL-6720E (2014a).

Rutqvist, J., Zheng, L., Chen, F., Liu, H.-H., and Birkholzer, J. (2014b) Modeling of Coupled Thermo-Hydro-Mechanical Processes with Links to Geochemistry Associated with Bentonite-Backfilled Repository Tunnels in Clay Formations. Rock Mechanics and Rock Engineering, 47, 167–186.

Rutqvist, J. (2015) Fractured rock stress-permeability relationships from *in situ* data and effects of temperature and chemical-mechanical couplings. Geofluids, 15, 48–66.

Rutqvist, J. (2017) An overview of TOUGH-based geomechanics models. Computers & Geosciences, 108, 56–63.

Sánchez, M., Gens, A., do Nascimento Guimarães, L., and Olivella, S. (2005) A double structure generalized plasticity model for expansive materials. Int. J. Numer. Anal. Meth. Geomech., 29, 751–787.

Senger, R., and Marschall, P. (2008) Task Force on EBS / Gas Transport in Buffer Material, Nagra Arbeitsbericht NAB 08-24.

Senger R., Romero, E., Ferrari, A., and Marschall, P. (2014) Characterization of gas flow through low-permeability claystone: laboratory experiments and two-phase flow analyses. Norris, S., Bruno, J., Cathelineau, M., Delage, P., Fairhurst, C., Gaucher, E. C., Ho¨hn, E. H., Kalinichev, A., Lalieux, P.

& Sellin, P. (eds) Clays in Natural and Engineered Barriers for Radioactive Wast Confinement. Geological Society, London, Special Publications, 400, http://dx.doi.org/10.1144/SP400.15

Shen, X., and Shen, G. (2002) A fracture-energy-based elasto-softening-plastic constitutive model for joints of geomaterials, Applied Mathematics and Mechanics, 23(9), 1097–1104.

Tamayo-Mas, E., Harrington, J.F., Shao, H., Dagher, E.E., Lee, J., Kim, K., Rutqvist, J., Lai, S.H., Chittenden, N., Wang, Y., Damians, I.P., and Olivella, S. (2018) Numerical modeling of gas flow in a compact clay barrier for DECOVALEX-2019, Proceedings of ARMA/DFNE 2018 (DFNE 18-623).

van Genuchten, M.T. (1980) A closed-form equation for predicting the hydraulic conductivity of unsaturated soils. Soil. Sci. Soc. Am. J., 44, 892-898.

Vilarrasa, V., Rutqvist, J., Blanco-Martin, L., and Birkholzer, J. (2016) Use of a dual structure constitutive model for predicting the long-term behavior of an expansive clay buffer in a nuclear waste repository. *ASCE's International Journal of Geomechanics*, 16, article number D4015005.

Wang, Y. (2011) Research & Development (R&D) Plan for Used Fuel Disposition Campaign (UFDC) Natural System Evaluation and Tool Development, U.S. DOE Used Fuel Disposition Campaign.

Witherspoon, P.A., Wang, J.S.Y., Iwai, K., and Gale, J.E. (1980) Validity of cubic law for fluid flow in a deformable rock fracture, Water Resources Research, 16, 1016–1024.

Yip, M., Mohle, J., and Bolander, J. (2005) Automated modeling of three-dimensional structural components using irregular lattices, Computer-Aided Civil and Infrastructure Engineering, 20, 393–407.

Zheng, L., Rutqvist, J., Steefel, C., Kim, K., Chen, F., Vilarrasa, V., Nakagawa, S., Houseworth, J., and Birkholzer J. (2014) Investigation of Coupled Processes and Impact of High Temperature Limits in Argillite Rock. Prepared for U.S. Department of Energy, Used Fuel Disposition, FCRD-UFD-2014-000493, Lawrence Berkeley National Laboratory, LBNL-6719E.

Zheng, L., Rutqvist, J., Kim, K., and Houseworth, J. (2015) Investigation of Coupled Processes and Impact of High Temperature Limits in Argillite Rock. Prepared for U.S. Department of Energy, Used Fuel Disposition, FCRD-UFD-2015-000362. LBNL-187644, Lawrence Berkeley National Laboratory.

Zheng, L., Kim, K., Xu, H., and Rutqvist, J. (2016) DR Argillite Disposal R&D at LBNL. FCRD-UFD-2016-000437, LBNL-1006013, Lawrence Berkeley National Laboratory.

Zheng L., Kim K., Xu H., Rutqvist J., Voltolini M., and Xiaoyuan C. (2017) Investigation of Coupled Processes and Impact of High Temperature Limits in Argillite Rock: FY17 Progress. Prepared for U.S. Department of Energy, Spent Fuel and Waste Disposition. SFWD-SFWST-2017-000040, LBNL-2001014, Lawrence Berkeley National Laboratory.